HIGH RESOLUTION MID-INFRARED IMAGING OF ACTIVE GALACTIC NUCLEI

By

JAMES THOMAS RADOMSKI

A DISSERTATION PRESENTED TO THE GRADUATE SCHOOL
OF THE UNIVERSITY OF FLORIDA IN PARTIAL FULFILLMENT
OF THE REQUIREMENTS FOR THE DEGREE OF
DOCTOR OF PHILOSOPHY

UNIVERSITY OF FLORIDA

2003

To Mom, Dad, and my family

contributions to pteradon paleontology. I am grateful to all my office mates over the years from 201, 301, 405, and 14 and I thank Beth for her counsel and friendship. I also would like to wish good luck to my friend Boon who has been with me since the beginning and thank him for all he has done for me. I also owe a great deal to Pimol whose love and support have been the glue that has kept me together this last difficult year.

Last but not least I would like to thank all those in the Department of Astronomy who have contributed to my success. It has been a great pleasure working with the Infrared Astrophysics Group. I credit Charles Telesco and my advisor Robert Piña with my training as an astronomer. All I know I learned from them. I thank them for all the knowledge and experiences. I would like to specially thank Chris Packham whose unwavering support gave me confidence to complete any task. I also thank Fred Hamann for his help in completing my dissertation. I am also grateful to the company of David Ciardi and Jeff Julian who made observing runs as well as intramural sporting events very entertaining. I thank Jaydeep and The Florida Space Grant Consortium for help in my research. Finally, all my degrees and accomplishments at U.F. have been the direct result of the hard work and support of the finest secretaries I have ever known. They have always been more than co-workers; they have been my family away from home. I want to thank Ann, Janice, Glenda, Debra, Audrey, and Tracey for all their help.

Abstract of Dissertation Presented to the Graduate School
of the University of Florida in Partial Fulfillment of the
Requirements for the Degree of Doctor of Philosophy

HIGH RESOLUTION MID-INFRARED IMAGING OF ACTIVE GALACTIC NUCLEI

By

James Thomas Radomski

May 2003

Chair: Fred Hamann
Department: Astronomy

Type 1 AGN are characterized by broad emission lines in addition to narrow permitted
and forbidden lines, whereas as Type 2 AGN reveal only narrow emission lines. The
"grand unified model" suggests these AGN represent the same phenomenon; a super
massive black hole (SMBH) surrounded by a dusty torus. In the case of Type 2 AGN the
line-of-sight intercepts the torus (edge-on) and obscures the broad emission lines. In Type
1 the torus is orientated such that the line of sight is perpendicular to the plane of the
torus (pole-on) allowing observations of the broad emission lines close to the SMBH.
However, the idea that AGN classification depends solely on the line of sight to the
central engine has been called into question by recent surveys of AGN. These surveys
reveal that the host galaxies of Type 2 AGN typically have an increased level of star
formation as compared to Type 1. Several authors suggest that this is due to an
evolutionary link between Type 1 and 2 AGN. In these models material associated with
circumnuclear starbursts in addition to the torus acts to obscure Type 2 AGN. As these

starbursts evolve over time and expel excess material through superwinds, the central AGN is more likely to be classified as a Type 1.

A key prediction of evolutionary models is a greater occurrence of circumnuclear starbursts with Type 2 AGN in comparison to Type 1 AGN. Previous observations suggest the size of such circumnuclear starburst may be on order of a few hundred parsecs. A high resolution mid-IR survey of AGN which can trace the peak emission of such circumnuclear starbursts on the scales necessary to test evolutionary predictions is needed. This dissertation outlines the process necessary to conduct such a mid-IR survey and presents three preliminary observations of AGN. These AGN (NGC 4151, Cygnus A, and Mrk 231) show no strong circumnuclear starburst activity but are too few to accurately test evolutionary predictions statistically. However these observations show the advantages of mid-IR imaging in studying the relationship between AGN and starburst activity in the central kiloparsec of active galaxies.

CHAPTER 1
INTRODUCTION

The nuclei of some galaxies produce an amount of energy thousands of times more powerful than our entire Milky Way galaxy on scales comparable to our solar system. These galaxies with powerful non-stellar central engines are referred to as "Active Galactic Nuclei" or AGN. This powerful central radiation ranges over the entire electromagnetic spectrum. The most likely source of this central power is the accretion of matter onto a supermassive ($> 10^6$ M$_\odot$) black hole (Rees 1984).

In addition to high luminosities from a small area due to non-stellar processes, AGN display many other characteristics. In contrast to normal galaxies, AGN commonly show bright highly ionized emission lines which at optical and UV wavelengths can contribute several percent to the total continuum flux and show an equivalent width of up to 10^4 km s^{-1}. AGN also show high degrees of variability in their nuclei usually at X-ray, ultraviolet (UV), and optical wavelengths. This variability can be as large as an order of magnitude or greater on scales ranging from seconds to decades. Active galactic nuclei also show high degrees of polarized emission as well as strong continuum emission over the entire electromagnetic spectrum from gamma rays to radio wavelengths.

AGN can generally be classified into two groups. Type 1 AGN display permitted lines with very broad velocity wings (typical FWHM in the range of 10^3-10^4 kms^{-1}) while observed forbidden lines show narrower profiles (FWHM $\leq$1000 kms^{-1}). In Type 2 AGN, both permitted and forbidden lines display similar narrow velocity widths (FWHM$\leq$1000 kms^{-1}). The line characteristics outlined above can best be explained in terms of a broad

emission line region (BLR) and a narrow emission line region (NLR), where a Type 1 AGN displays both the BLR and NLR whereas Type 2 only (directly) display the NLR.

AGN Emission

In order to better understand AGN emission a general review of emission processes is needed. These can be subdivided into two major categories; line emission and continuum emission.

Line Emission

Line emission processes are separated into two categories; broad emission lines and narrow emission lines.

Broad emission lines

As discussed earlier, Type 1 AGN display emission lines of hydrogen as well as He I, He II, and Fe II. The emission lines show very broad velocity widths (FWHM ~1000-10,000 km s^{-1}; Robson 1996) produced in what is commonly referred to as the broad emission line region (BLR). This emission is primarily due to photoionization of gas by the central engine (Yee 1980; Shuder 1981). The lack of forbidden emission lines in this region implies a minimum electron number density of 10^8 cm^{-3}. Photoionization models of MacAlpine (1986) also estimate a temperature of ~ 10^4 K and a mass of ionized gas of ~ 10^4 M$_\odot$. The size of the BLR can be estimated from observations of variable AGN. The time delay from the change in AGN continuum luminosity to that of the broad emission lines imply the size of the BLR to be ~0.01-1 pc (Netzer & Peterson 1997).

Narrow emission lines

Narrow emission lines are present in all varieties of AGN. They are the result of the photoionization of gas and in some cases collisionally ionized gas. Forbidden lines such as [O III], [N II], [Ne III], [S II], and [OII] are present with FWHM ≤ 1000 km s^{-1}.

Ratios of these forbidden lines show electron number densities of 10^3-10^6 cm^{-3} (Netzer 1990). Photoionization models also calculate a typical $T \sim 10^4$ K and a mass of $\sim 10^9$ $M_\odot$. The gas is further from the central engine than the BLR and thus displays lower ionization and lower velocities. The location of these emission lines lead to what is called the narrow emission line region (NLR). Observations of Seyferts by Dahari & DeRobertis (1988) found that the size of the NLR ranges from 0.1-1 kpc.

Continuum Emission

Continuum emission processes in AGN are discussed below. These include synchrotron, compton, and bremsstrahlung emission as well as blackbody radiation.

Synchrotron radiation

Synchrotron emission is caused by accelerated charged particles spiraling around a magnetic field at relativistic speeds (Figure 1-1). Although this may pertain to both protons and electrons, protons are typically less common because they are much harder to accelerate due to their greater mass. The frequency of the electromagnetic radiation emitted by the charged particle is proportional to its energy and the strength of the magnetic field. If the electrons are moving at relativistic velocities, the emission will be beamed in the form of a narrow cone in the electrons instantaneous direction of travel.

The shape of the synchrotron spectrum is determined by the energy distribution of the emitting particles. Observations of cosmic rays shows that the energy distribution of these charged particles follows a power law. Thus a synchrotron emission spectrum from such an ensemble of electrons also shows a power law dependence. The spectral index of this radiation is typically $\alpha \sim -0.7$ such that $F_\nu \propto \nu^\alpha$. Deviations from this spectral index however are evident at high and low frequencies. At high frequencies such as in the
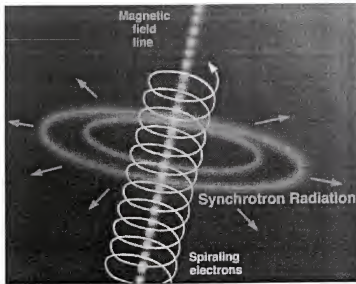
Figure 1-1. A schematic of synchrotron radiation (illustration by Jon Lomberg; Image Credit: Gemini Observatory)
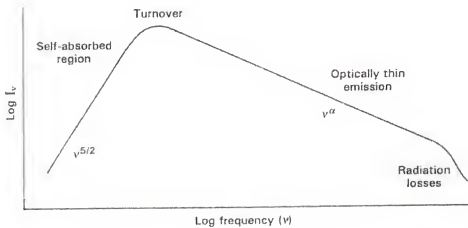
Figure 1-2. Synchrotron spectrum schematic. (Robson 1996)

optical and X-ray the spectrum is dominated by the finite radiative lifetimes of the electrons resulting in an increased spectral slope due to radiation losses. At low frequencies the photons emitted will become self-absorbed by the ensemble of electrons

which now become optically thick to their own emission. This results in a turnover in the spectral index such that $\alpha \sim 2.5$ (see Figure 1-2).

Compton emission processes

The Compton effect is caused when a high energy photon interacts with a low energy electron. This results in a loss in the photon's energy and the "boosting" of the electron's energy. This process is also referred to as Compton scattering as the photon is effectively scattered, losing energy and decreasing in frequency. This results in the heating of the electron field and the cooling of the photon field. In the low energy analog, the photon energy remains constant and the process is referred to as Thompson scattering. Compton emission is important in regions where electrons exist in an intense high energy photon field such as near the accretion disk of a black hole (Robson 1996).

Also important in the region of a black hole is inverse Compton emission which involves a high energy electron interacting and "boosting" the energy of a photon resulting in a higher frequency. This process acts as a cooling process for the electrons which in turn heats the surrounding photons. The inverse Compton effect is also related to synchrotron radiation. In the case of a self-absorbed synchrotron source such as a quasar, synchrotron photons, through the Compton effect, scatter electrons to higher energies. As the electrons interact with the magnetic field, more synchrotron photons are created and the process repeats, increasing the temperature of the electron field. A limit is reached however due to the inverse Compton effect. This occurs when the photon and electron energy densities are sufficiently large such that the high energy electrons scatter their own synchrotron photons. The boosted photons are no longer self-absorbed and escape. This results in a cooling of the electron field and an upper electron temperature limit of $\sim 10^{12}$ K .
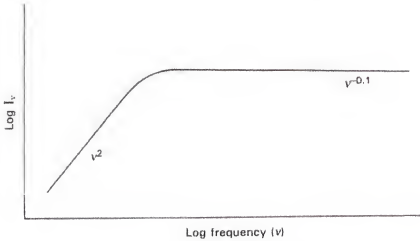
Figure 1-3. Schematic of bremsstrahlung emission (Robson 1996).

Bremsstrahlung (free-free) emission

Bremsstrahlung emission is caused by free electrons of an ionized gas interacting with each other or with positive ions. The word Bremsstrahlung is of German derivation and is loosely translated as "braking radiation" which refers to the de-acceleration of the free electron in the field of another charged particle. It is also referred to as "free-free[1]" emission as it involves the interactions of free particles. Bremsstrahlung emission is found in the atmospheres of stars, HII regions, and hot dense plasmas which may occur in the nuclei of an AGN. It has been suggested as the cause of the big blue bump at UV wavelengths in the spectra of AGN, although this feature could also be due to thermal radiation from an accretion disk. Bremsstrahlung radiation ranges from radio through X-ray wavelengths is unpolarized and has a smooth spectral profile. The spectral index

---

[1] Other interactions such as the collision of a photon resulting in the ejecting of an electron bound to an atom is referred to as a "bound-free" interaction or ionization, while the inverse is called "free-bound" or recombination.

follows a $v^{-0.1}$ slope when the emission is optically thin and drops to v^2 when the emission becomes self-absorbed or optically thick (see Figure 1-3).

Blackbody radiation

A blackbody has a surface emissivity of 1. Such a body will emit all of the thermal radiation it can (as described by theory), and will absorb 100% of the thermal radiation striking it. Most physical objects have surface emissivities less than 1 and hence do not have blackbody surface properties. Blackbody emission is isotropic and displays a smooth continuous spectrum that depends solely on the temperature of the object. Blackbody emission is important to understand as many astronomical sources such as stars closely approximate a blackbody continuum. The form of a blackbody follows the Planck function

$$B_v(T) = \frac{2 \cdot h \cdot v^3}{c^2 \cdot \left(e^{\frac{h \cdot v}{k \cdot T}} - 1 \right)} \qquad (1\text{-}1)$$

where $B_v(T)$ the emitted intensity of radiation per unit frequency v as a function of temperature T, h is Planck's constant, c is the velocity of light, and k is the Boltzmann's constant. This equation can also be written in terms of wavelength λ.

$$B_\lambda(T) = \frac{2 \cdot h \cdot c^2}{\lambda^5 \cdot \left(e^{\frac{h \cdot c}{\lambda \cdot k \cdot T}} - 1 \right)} \qquad (1\text{-}2)$$

Figure 1-4 shows the blackbody spectrum at several temperatures. Note that a higher temperature blackbody curve encloses and never crosses a lower temperature blackbody curve. The peak of a blackbody curve can be found in terms of λ by taking the derivative of equation (2) such that $d(B_\lambda(T))/d\lambda = 0$. This results in Wien's displacement law

$$\lambda_{max} = \frac{2898}{T} \qquad (1\text{-}3)$$
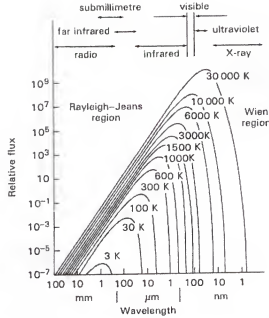
Figure 1-4. Blackbody spectra at several different temperatures. (Robson 1996)

where λ_{max} is the peak wavelength in μm and T is in K. Equations (2) can also be simplified mathematically for the two regions seen in figure 1-4. When $hc/\lambda kT \gg 1$ equation (2) can be simplified to

$$B_\lambda(T) = \frac{2 \cdot h \cdot c^2}{\lambda^5 \cdot e^{\frac{h \cdot c}{\lambda \cdot k \cdot T}}} \tag{1-4}$$

This is referred to as the Wien distribution or region and lies on the short wavelength side of the peak. Correspondingly when $hc/\lambda kT \ll 1$ equation (2) can be approximated as

$$B_\lambda(T) = \frac{2 \cdot c \cdot k \cdot T}{\lambda^4} \tag{1-5}$$

which is known as the Rayleigh-Jean distribution which lies at wavelengths longward of the emission peak.

AGN Emission Model

Figure 1-5 shows a schematic model of the spectrum of an AGN/starburst galaxy from the UV (0.1 μm) to the submillimeter (1000 μm). Several processes throughout the galaxy contribute to the overall continuum. Blue and yellow stars contribute strongly to the UV and optical emission. Photospheric radiation from red giants and supergiants typically dominate at near-IR (1-5 μm) wavelengths. Contribution from blue stars, ionized gas emission (bremsstrahlung), and very hot dust grains near sublimation (~1000-1500 K) also permeate the near-IR regime. In the mid-IR (5-30 μm) thermal re-radiation of dust becomes more important. Dust grains heated to a few hundred K by the central AGN and massive young stars typically dominate the mid-IR. The peak of the energy distribution of an AGN with a strong starburst component occurs in the far-IR (30-100 μm). This represents dust predominately heated by young massive stars to a T ~ 30-50 K. The far-IR and submillimeter also contains a small contribution from "cirrus" emission, which is more prevalent in "quiescent" galaxies with low activity. This emission is referred to as cirrus for its filamentary appearance and resemblance to cirrus clouds in the Earth's atmosphere. It represents cool dust emission (~ 10 K) from the interstellar radiation field characteristic of a very red and old stellar population.

Other wavelength regimes not shown in figure 1-5, such as X-ray and radio, also contribute to the spectrum of AGN. X-ray emission can represent a significant contribution to the bolometric luminosity of some AGN. Although AGN range in X-ray luminosity over several orders of magnitude the overall spectrum of X-ray emission is relatively uniform. X-ray emission typically follows a power law of index ~ 1 for radio quiet sources and ~ 0.5 for radio loud sources (Wilkes & Elvis 1987). Radio emission in AGN is most readily attributed to synchrotron radiation. In many cases this emission is
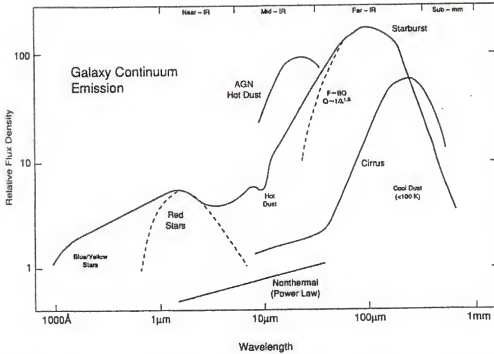
Figure 1-5. Schematic overview of spectral energy distribution of an AGN/ starburst galaxy (Telesco 1993).

seen as large jets in radio galaxies. However, even in radio-loud sources only ~ 1% of an AGN's total luminosity is emitted at radio wavelengths (Osterbrock 1991).

Classification of AGN

AGN can be classified into several subcategories, according to their luminosity, emission line properties, variability, and even circumstances involving initial discovery. These varieties of AGN frequently overlap and often have arbitrary dividing lines. One of the most frequently used partitions among AGN involves radio luminosity. This results in the separation of AGN into two major categories; radio loud and radio quiet. These categories also contain subclasses of various AGN whose properties and descriptions are discussed below.

Radio Quiet AGN

Radio quiet AGN have modest radio emission with radio luminosities at 1.5 GHz of $<$ 10^{25} W Hz^{-1} (Woltjer 1990). A second definition of radio loudness involves using the ratio of radio to optical emission. A ratio of radio emission at 5 GHz to optical B-band flux in the form of $F_{5\,GHz} / F_B < 10$ defines an AGN as radio quiet (Kellerman et al. 1989). Examples of AGN in this class are discussed below.

Seyfert galaxies

In 1943 Carl Seyfert completed a study of six galaxies selected from the plate archives of the redshift surveys of the Mt. Wilson Observatory. These galaxies showed bright nuclei with respect to their disk component. Also, compared to normal galaxies whose spectra were generally devoid of emission lines, these galaxies revealed broad emission lines at visible wavelengths (Figure 1-6). They became known as Scyfert galaxies and later became the basis for an entire class of active galaxies. As spectroscopic techniques improved, Khachikian & Weedman subdivided Seyferts into two categories in 1974. In one group of Seyferts, both permitted and forbidden emission lines had the same width, whereas in a second group there was a marked difference between the widths of the permitted and forbidden lines (Figure 1-7). In Seyfert 1 (Sy 1) galaxies the permitted lines, HI, He I, He II, and Fe II seen at optical wavelengths show very broad velocity widths with FWHM in the range from 1000-10,000 km s^{-1} (Robson 1996). However, the forbidden lines such as [O III], [N II], [Ne III], [S II], and [OII] lack the very broad wings and have FWHM $\leq$ 1000 km s^{-1}. In Seyfert 2 (Sy 2) galaxies, both permitted and forbidden lines have similar velocity widths $\leq$ 1000 km s^{-1}. This led to what is referred to as the broad emission line region (BLR) and the narrow emission line
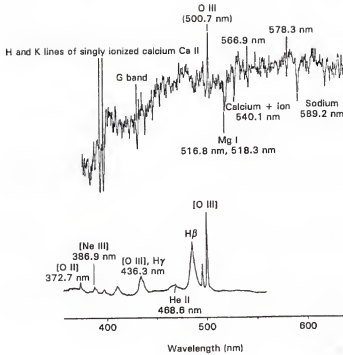
Figure 1-6. Optical spectrum of a spiral galaxy (top) showing absorption lines due to the stars of the galaxy and narrow emission line of the doubly ionized oxygen [O III] due to ionized hydrogen regions around star formation sites. Below is the Seyfert galaxy Mrk 509 whose spectrum is dominated by the very strong and broad emission lines of hydrogen. (Audouze & Israel 1985; Robson 1996)

region (NLR) discussed above. Therefore Seyferts were the first class of AGN to be

divided into Type 1 (showing broad and narrow line regions) and Type 2 (showing only

narrow line regions). Subsequent researchers have also sub-divided Seyferts into

intermediate classes such as Types 1.2, 1.5, 1.8, and 1.9 based on the increasing strength

of narrow lines with respect to the broad lines (Maiolino et al. 1995; Osterbrock 1989).
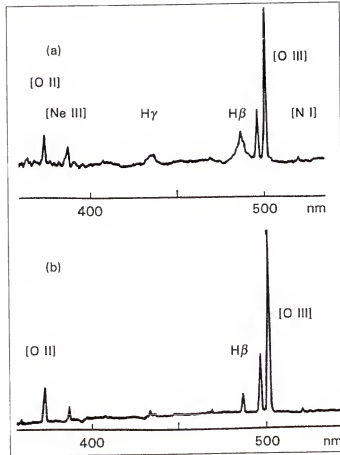
Figure 1-7. Optical spectra of (a) the Seyfert 1 galaxy NGC 3227 and (b) the Seyfert 2 galaxy Mrk 1157. Note how the permitted lines of Hα and Hβ differ in their FWHM. (Osterbrock 1989; Robson 1996)

Radio quiet quasars

Radio quiet quasars (also referred to as Quasi Stellar Objects or QSOs) are very similar to high luminosity Seyfert 1 galaxies. In fact the dividing line between these two types of galaxies is somewhat arbitrary with galaxies brighter than absolute V-band magnitude $M_V = -23$ classified as QSOs while those dimmer are classified as Seyfert 1. The division between QSOs and Seyfert 1 also shows some distance bias based on their initial discovery. Distant star-like objects that were later found to be extremely luminous and contain broad emission lines were classified as QSOs, while closer objects in which

the host galaxy was more obvious tended to be classified as Seyfert 1. Though QSOs are very similar to Seyfert 1, there seems to be a definite lack of Type 2 QSOs which contain no observable broad emission lines. Reasons for this deficit may be due to their concealment in a subset or warm ultraluminous infrared galaxies (Antonucci 1993) or the dynamics of their luminous central AGN (Ohsuga et al. 1999).

Low ionization nuclear emission line regions (LINERS)

LINERS represent the low luminosity counterparts to Seyferts and QSOs. They are mainly found in early spirals of type Sa and Sb, with some also found in Sc and irregular morphologies. These galaxies were first identified by Heckman (1980). LINERS differ from normal spiral galaxies by frequently having compact flat spectrum radio cores and occasionally an unresolved central X-ray source. In addition they typically show signatures of AGN activity containing strong emission in [OI], [SII], and [NII] (Osterbrock 1991). However they differ from Seyferts due to weak emission from highly ionized lines such as [OIII] and Ne V. LINERS are considered the low luminosity counterparts to active galaxies such as Seyferts. Evidence for this is strengthened by the observations of weak Hα emission in NGC 7213 by Filippenko and Halpern (1984) as well as other LINERS observed by Filippenko and Sargent (1985). Alternatively some LINERS may have a "non-active" explanation for the source of their emission lines. Strong circumnuclear starburst activity may result in the LINER classification of galaxies such as Arp 220 (Genzel et al. 1998), though such galaxies still may contain a weak AGN.

Radio Loud AGN

Radio loud AGN have radio luminosities at 1.5 GHz of $> 10^{25}$ W Hz^{-1} (Woltjer 1990). Their ratio of radio emission at 5 GHz to optical B-band flux is $F_{5\,GHz} / F_B \geq 10$

(Kellerman et al. 1989). These galaxies can be divided into two classes, Type 1 Broad Line Radio Galaxies (BLRG) and Type 2 Narrow Line Radio Galaxies (NLRG) based on their optical spectra. In a general sense these types are similar to those associated with Seyfert galaxies. One major difference from their radio quiet counterparts is that while Seyferts are most often associated with spiral galaxies these radio galaxies are most likely to be associated with ellipticals.

Other subcategories of radio loud AGN depend on their spectral slope where a distinction is made at the frequency of 1 GHz. Steep spectrum galaxies with $\alpha < -0.4$ ($F_\nu \propto \nu^\alpha$) are "lobe dominated" galaxies containing one or two extended lobes of diffuse radio emission fed by radio jets from the cores of these galaxies. Core dominated radio galaxies are characterized by strong radio emission from a compact core on the scale of an arcsecond (Robson 1996). Unlike their lobed counterparts, these class galaxies show weak or no line emission. In addition, they show a very flat radio spectrum in contrast to the steep spectrum of lobe dominated galaxies. They may also display prominent single-sided radio jets on scales of ~ kpc. Most of the population of BLRG are core dominated while NLRG are predominately lobe dominated (Lawrence 1987).

A further subdivision of radio galaxies was found by Fanaroff and Riley (1974). This divides sources into two luminosity classes with a transition luminosity of L_ν (178 MHz) $\approx 2 \times 10^{25}$ W Hz^{-1}sr^{-1}. These two classes were referred to as Fanaroff-Riley I and II or FR I and FR II for short. Class I (FR I) sources are the weaker of the two classes at radio wavelengths. They are brightest in the center with decreasing brightness towards the edges of their radio lobes. In contrast, the more luminous FR II galaxies are frequently edge-brightened showing bright knots of emission in their outer lobes. NLRG show

features of both FR I and FRII galaxies while BLRG typically only display FR II characteristics.

Quasars

Quasars are dominated generally by an unresolved blue nucleus of high luminosity ($M_V > -23$) with radio structures similar to those of core and lobe dominated radio galaxies. They are also very closely related to their radio quiet counterparts displaying similar spectral shapes and broad emission lines as QSOs. Quasars however are typically larger, more luminous, and bluer than QSOs. They are also 10 -20 times less numerous than their radio quiet counterparts (Peterson 1997). They represent the high end of the luminosity spectrum of AGN hosting the most powerful galaxies in the class.

BL Lacertae objects (BL Lacs)

BL Lac's display a featureless continuum spectra along with rapid variability (timescales of hours and longer) and strong polarization (≥ 5 %). The continuum emission rises steeply from x-ray to the infrared while the radio continuum resembles that of flat spectrum core dominated radio galaxies. The variability of BL Lacs is the most dramatic of all AGN changing in amplitude as much as four magnitudes on timescales of hours. These galaxies however are quite rare, numbering ~100s. They also are found at relatively low redshifts ($z < 0.2$) and are frequently associated with superluminal motion. This class of AGN also shares many properties with other rare and highly polarized galaxies such as optically violently variable objects (OVVs) and Highly Polarized Quasars (HPQs).

Unification

As discussed above, the different classifications of AGN have many overlapping qualities. While initial studies of AGN relied on separating individual classes, recent

efforts have focused on unifying the different types. The "grand unified model" suggests that the central engine of an AGN is powered by accretion of gas and dust onto a rotating supermassive black hole (SMBH) (Rees, 1984). The accretion process releases energy in the form of high-energy photons which photoionize material orbiting close to the SMBH (~0.1-1pc), producing the Doppler-broadened emission lines characteristic of the BLR. The NLR is located along the poles of the SMBH, at distances ranging from 100-1000 pc. The greater distance from the SMBH results in a lower rotational velocity leading to the narrow widths of the emission lines. Both the BLR and NLR are excited either by photoionization from the UV continuum of the central engine (Koski 1978; Ferland & Netzer 1983; Stasinska 1984), by shock excitation from jets (Sutherland, Bicknell, & Dopita 1993; Dopita & Sutherland 1995), or by a combination of the two. Surrounding the central engine in the accretion plane of the AGN a geometrically and optically thick torus of gas and dust (see Figure 1-8). The torus obscures the central engine from direct view at some lines of sight, dependant on the covering fraction of the torus. If the line of sight to an AGN is along the rotation axis of the system, both the BLR and NLR will be directly observed and hence it will be classed a Type 1 AGN. If the line of sight is perpendicular to the axis of the system, the torus will obscure the central engine and a Type 2 AGN will be observed. In the case of radio loud AGN, a synchrotron jet is also present. Observations along the jet axis will result in enhanced radio emission and strong variability resulting in a BL Lac or "blazar" classification.

Strong evidence for unifying Type 1 and 2 AGN came through spectropolarimetry of the Seyfert galaxy NGC1068 by Antonucci and Miller (1985). They detected broad emission lines in polarized flux in what was previously classed as a Type 2 Seyfert. Thus
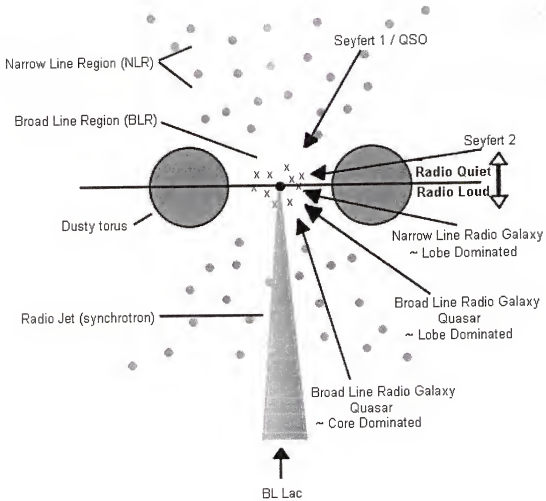
Figure 1-8. Schematic diagram of unified scheme for AGN.
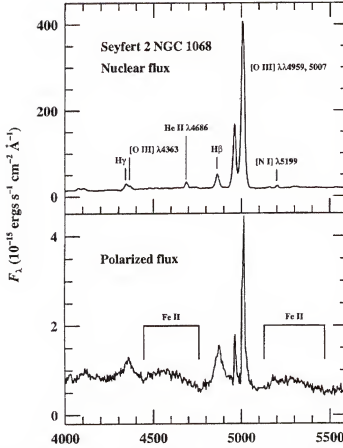
Figure 1-9. NGC 1068 spectra. Notice the broad Hβ emission which becomes apparent only in polarized light. (Miller, Goodrich, & Matthews 1991; Robson 1996)

they concluded that NGC1068 possessed a BLR, similar to those detected in Type 1 but

hidden from our direct view, revealed in polarized flux due to scattering from clouds of

dust/electrons that scatter broad emission lines into our line of sight (Figure 1-9).

Therefore, Antonucci and Miller (1985) suggested that Type 1 and Type 2 Seyferts both

contain a BLR and a NLR but the BLR is hidden in Type 2 by a dusty torus.

Unification is also applicable to radio loud galaxies. The unification scheme for

NLRG (Type 2) and BLRG (Type 1) is similar to that of Seyfert 1 and Seyfert 2 galaxies

discussed above. In the case of NLRG, the broad emission line region is obscured by a

line-of-sight intersecting the torus, while the line-of-sight to a BLRG is more closely

perpendicular to the plane of the torus avoiding the obscuration and revealing the BLR. Evidence for this has been observed in the NLRG 3C 234 (Antonucci & Barvainis 1990; Young et al. 1997). Like NGC 1068 this galaxy displayed only narrow emission lines until it was observed in polarized light which clearly showed broad Hα indicative of a BLR.

Unification Problems

In the grand "unified model" of AGN the appearance as Type 1 or 2 depends solely on the observed line of sight to the central engine. However, this may not hold true for Seyfert galaxies which represent the most studied class of AGN due to their relatively close proximity and abundance (outnumbering radio galaxies by a factor of ~100; Osterbrock 1989). Recent surveys have cast doubt on the suggestion that the line of sight to the central engine is the only defining characteristic of Seyfert classification. Edelson, Malkan, and Rieke (1987) showed the 10μm luminosity of Sy 2 host galaxies is less compact than in Sy 1 hosts. These results were later confirmed by 10μm observations of Rieke (1992) and Maiolino et al. (1995). They noted that Sy 2 host galaxies display enhanced infrared luminosity from their host disks by around one magnitude compared with Type 1 and "non-active" galaxies. In addition, Dahari and DeRobertis (1988) found Sy 2 hosts typically show increased far-IR emission as compared to Sy 1 hosts. This result was also confirmed by Heckman et al. (1989) who showed that Sy 2 hosts included in the RSA sample show an average far-IR luminosity 3-4 times larger than Sy 1 hosts or 'non-active' galaxies despite showing the same absolute magnitude and Hubble type. Pogge (1989) and Gonzales-Delgado and Perez (1995) showed Sy 2 hosts preferentially show greater extended emission in Hα and [NIII] as compared to Sy 1 hosts. The results

outlined above are most readily explained in terms of an elevated star formation rate in host galaxies with Sy 2 nuclei as compared to Sy 1.

In addition to enhanced star formation, it has been tentatively reported that the morphology of Sy 2 hosts differ from that of Sy 1. Maiolino et al. (1997) found that Sy 2 hosts are 20% more likely to have non-axisymmetric potentials (peculiar or irregular morphologies) than Sy 1 hosts. Hubble WFPC 2 observations by Malkan et al. (1998) also showed that Sy 2 AGN are typically hosted by later type galaxies than Sy 1 AGN. Malkan also showed that Sy 2 hosts have a greater overall nuclear dust mass distributed in irregular patches and lanes close to the nucleus. This result correlates well with earlier observations of Dahari and DeRobertis (1988) that found NLR (sizes 0.1-1 kpc) of Sy 2 are more heavily reddened suggesting an excess of dust and cold gas in those AGN.

A further problem associated with the grand unified model arises when the source of the blue featureless continuum (BFC) of Sy 2 galaxies is considered. The BFC is found on small scales (sub-kpc) and produces most of the near UV emission and typically 10% – 50% of the optical emission longward of 4000 Å (Heckman et al. 1997). The classical Seyfert unified model accounts for this feature as non-stellar emission scattered from the hidden Sy 1 nucleus into our line of sight. The emission is scattered into our line of sight along the polar axis of the SMBH from electrons or dust (Miller, Goodrich, & Mathews 1991; Antonucci 1993). This model readily accounts for the observed properties of NGC1068 (Antonucci & Miller 1985) but additional observations revealed this model cannot account for the origin of the BFC in other Seyfert AGN. First, the typical observed degrees of polarization of the central regions of Sy 2 are a few percent, far lower than the predicted values (Martin et al. 1983; Miller & Goodrich 1990; Tran, Miller

& Kay 1992; Kay 1994). Second, the CaII absorption triplet is not as diluted in the BFC

as would be expected if the source were non-stellar in origin (Terlevich, Diaz, &

Terlevich 1990). Finally broad emission lines, which should also be reflected into our

line-of-sight by the "mirror" are either absent or below the expected detection threshold.

Cid Fernandez and Terlevich (1995) suggest these problems can best be reconciled if the

primary source of the BFC is young stars located near the nucleus of the Sy 2 host rather

than reflection of emission from the central engine. Evidence for the stellar origin of the

BFC has been detected at UV wavelengths for eight galaxies by Heckman et al. (1997),

Colina et al. (1997), and Gonzalez-Delgado et al. (1998).

Amendment to the Grand Unified Theory: The Evolutionary Model

In order to account for the problems with the grand unified model as outlined above,

Heckman et al. (1989) outlined an alternative theory. This theory was similar to earlier

scenarios proposed by Weedman 1983 (also Terlevich & Melnick 1985; Heckman,

Armus, & Miley 1987; Sanders et al. 1988; Norman & Scoville 1988; Rieke, Lebofsky,

& Walker 1988) in which an evolutionary connection between galaxy types was made.

Others including Osterbrock (1993), Miguel Mas-Hesse et al. (1995), and Storchi-

Bergmann et al. (2001) have also suggested evolutionary scenarios for Seyfert galaxies.

The model proposed by Heckman et al. (1989) has remained largely unaltered and has

been supported by the recent observations discussed above. In this theory, Seyfert

galaxies are characterized by the covering fraction of the central engine defined as the

fraction of the sky observable by the central engine versus that of the obscuration. The

division between Type 1 and 2 is thus attributable to intrinsic differences such as star

formation, morphology, and environment combined with the standard line of sight effects

addressed by the unified model. Evidence for this can be seen in the Hubble Space

Telescope (HST) observations of 256 Seyferts by Malkan et al. (1998) which show a greater fraction of the sky as seen from a Sy 2 nucleus is blocked by obscuration as compared to Type 1. The nature of this obscuring material may be a dusty molecular torus similar to that required for the unified model (Krolik & Begelman 1988) or dust lanes as suggested by Malkan et al. (1998). A torus would have to be geometrically and optically thick and on scales large enough to obscure the BLR, but less than a few hundred parsecs. Dust lanes would also be optically thick on scales >100 pc but not necessarily symmetric like a torus.

The evolutionary sequence starts when an event such as a merger, a galactic bar, or gravitational perturbations of close companions acts to funnel a large mass (10^9-10^{10} M_{sun}) of molecular material into the circumnuclear ($\leq$kpc) region of a galaxy. If self-gravity is important in the circumnuclear molecular disk, dynamical instabilities will quickly lead to a burst of star formation (Norman & Scoville 1988; Larson 1988), efficiently fueling a SMBH if one is already present (Norman 1987). Initially both the AGN and starburst will be shrouded in the molecular material in which they originated; hence, the emission from the source will be dominated by reprocessed mid/far-infrared thermal radiation. This is the FIRG (far-infrared galaxy) or starburst galaxy stage, characterized by very strong far-IR and CO emission (e.g. Sanders et al. 1988).

The starburst region will impart a significant amount of thermal and mechanical energy in the form of supernova explosions, Wolf-Rayet winds, and radiation pressure on the molecular gas. Combined with the starburst, energy from the AGN will act as an outflow and begin to expel molecular material from the circumnuclear region. This will result in a large-scale mass outflow in the form of a "superwind." At this stage, the AGN

still remains obscured along most lines of sight and the optical emission line spectrum is characterized by unusually broad forbidden lines and line ratios that are rarely observed in Seyfert types. They are instead either LINER or intermediate between LINER and giant HII regions (Heckman, Armus, & Miley 1987; Armus, Heckman, & Miley 1989). The broad lines arise in the superwind, while the line ratios may reflect the competing processes of shock heating by the superwind and photoionization from the partially excavated starburst and AGN.

As the nuclear region gradually is revealed from the dust shroud, the galaxy enters the Sy 2 stage. As the starburst is still underway, this region remains a strong source of far-IR and CO emission. The star formation in this near nuclear region could be the source of the BFC, predominantly observed in Sy 2 AGN (Cid Fernandez & Terlevich 1995, Colina et al. 1997). During this phase, from some lines of sight, it is possible to gain a direct view of the central engine revealing the BLR and non-stellar optical/x-ray continuum source. NGC 7469, a Sy 1 with strong CO and far-IR emission and a circumnuclear starburst represents a good example of this stage of AGN. As the starburst evolves and fades in intensity the obscuring wall collapses, increasing the viewing angle for which the AGN is classified as a Sy 1.

Finally, as the central engine becomes the dominant energy source, the central reservoir of molecular material is blown away, obscuration is reduced and the nucleus is revealed. Depending on the power of the central engine, either a Sy 1 or QSO is revealed. The galaxy will no longer be a strong CO source, and any excess in far-IR emission will arise predominantly in the compact AGN by non-thermal processes. Evidence for this final stage is supported by results of Edelson, Malkan, and Rieke (1987)

which show much greater relative strength of non-thermal versus thermal IR emission in QSO and Sy 1 than Sy 2 galaxies. Additional support for this model is found from the CO measurements of Curran (2000) who showed that Sy 1 hosts tend to have less material within the central regions than Sy 2 hosts.

Advantages of a High Resolution Mid-IR Survey

The mid-infrared is an ideal wavelength regime for investigating AGN and exploring evolutionary scenarios discussed above. The mid-IR (10-25μm) suffers 25–75 times less extinction than optical wavelengths and 3-10 times less extinction than the near-IR. This is especially important when studying the embedded regions in Sy 2 galaxies where the extinction must be at least 10 magnitudes at optical wavelengths in order to hide the broad emission line region (Malkan et al. 1998). The peak emission of many AGN also occurs in the mid-IR due to thermal re-radiation of dust from the surrounding torus. The mid-IR also provides an excellent trace of the peak emission of circumnuclear starbursts (Telesco 1993). These starbursts peak in the far-IR at $\lambda \sim 80$ -100 μm. Far-IR observations however are not possible from the ground due to the opaqueness of the Earth's atmosphere at these wavelengths. Current technological limitations on the aperture size of space-based and high altitude far-IR telescopes also limit their resolution to orders of an arcminute or worse. The mid-IR has the enormous advantage that it can be done with sub-arcsecond angular resolution at large ground-based telescopes (Telesco 1993).

A major problem with previous mid-IR observations has been resolving mid-IR emission sources. Most mid-IR data on Seyfert galaxies depend on low-resolution images taken by either IRAS (Infrared Astronomical Satellite) or ISO (Infrared Space Observatory). The beam of IRAS is approximately 30" x 90" while the ISO beam is 23".

This corresponds to a resolution of ~ 14 x 43 kpc for IRAS and ~11 kpc for ISO at an average distance of 100 Mpc. Higher resolution mid-IR surveys of Seyfert galaxies from the CfA sample (Huchra & Burg 1992) such as those by Rieke (1992), Maiolino et al. (1995), and Giuricin et al. (1995) were also at insufficient resolution to study Seyferts at sub-kpc scales. These surveys had a typical resolution of 5"-10" which correspond to average scales sizes ~2 kpc. However, the NLR of Seyferts typically extend on scales of 0.1-1 kpc (Dahari & DeRobertis 1988). In addition circumnuclear starbursts as observed in the UV by Heckman et al. (1997), Colina et al. (1997), and Gonzalez-Delgado et al. (1998), typically occur on scales of a few hundred parsecs. A key prediction of evolutionary scenarios is that AGN will display an increasing amount of circumnuclear star formation (seen as extended mid-IR emission) as one goes from Type 1 to Type 2 galaxies. In order to test this theory higher resolution mid-IR data that can resolves starbursts and dusty NLR structures on scales of a few hundred parsecs are needed.

The detection of extended mid-IR emission in the nuclear region of an AGN however does not necessarily confirm the existence of starburst activity. Several phenomenon unrelated to star formation may also occur on scales of a few hundred parsecs and result in extended mid-IR emission. Two primary examples include a dusty torus and NLR as described by the grand unified model. This dissertation used two methods by which to discern the primary source of extended mid-IR emission. First, a dusty torus or NLR is a result of dust heated by the central engine while starburst activity is a result of in-situ dust heating. Analysis of the color temperature of the emission (see Chapter 3) can determine if the temperature observed at a given distance is consistent with central heating. Also the morphology of the temperature map is useful in discerning between different sources

of mid-IR emission. A centrally heated NLR or torus will display a smooth radial profile containing a relatively hot core with subsequently cooler regions as the distance from the core increases. Starburst regions however should show no correlation with distance from the core and result in a more clumpy temperature morphology consistent with in-situ heating.

The second method used to confirm extended mid-IR emission as starburst related involved the use of complementary multi-wavelength results from the literature. High-resolution mid-IR imaging on scales less than a few hundred parsecs can only be achieved by observing a survey of nearby AGN. As discussed earlier, previous mid-IR surveys had insufficient resolution at which to observe the nuclear regions of these AGN. However due to the proximity of these AGN, they have typically been observed at several other wavelengths. By comparing results obtained in the mid-IR with results at other wavelengths the case for starburst activity may become clearer. Examples of this method involve observations of [OIII] $\lambda 5007$ which delineate the ionization cone or NLR of the AGN. Extended mid-IR emission associated with the NLR should be closely aligned with the major axis of the emission, while torus emission should be very close to perpendicular. Mid-IR emission showing no morphological relationship to this [OIII] ionization cone may indicate the presence of a star forming region.

Another multi-wavelength test involves the relationship of polycyclic aromatic hydrocarbon (PAH) emission and starburst activity. This PAH emission is found to be weak or absent in AGN with weak star formation and strong in AGN with strong starburst activity (Roche et al. 1991; Genzel et al. 1998). Thus if extended mid-IR emission is seen in the nuclear region of an AGN which is also found to have strong PAH

emission, a strong starburst may be the source of the mid-IR emission. Other multi-wavelength tests to confirm starburst activity in the cases of AGN discussed in this dissertation on performed on a case by case basis depending on the individual data collected for each source (see Chapters 4 through 6). Although multi-wavelength analysis provides a further evaluation of the activity in the nuclear regions of AGN, high resolution mid-IR imaging which traces the peak energy distributions of both the AGN and starburst still provides one of the best methods by which to study these sources of emission.

The Goal of this Dissertation

The goal of this thesis was to carefully explore, at the highest available resolution, the mid-IR properties of the nuclear environments of a survey of AGN in order to test evolutionary predictions. These models suggest that Type 2 AGN evolve over time into Type 1 AGN. If this evolution does occur one would expect to observe a higher incidence of circumnuclear starburst activity in Type 2 AGN as compared to Type 1. The mid-IR which traces the peak emission of both starburst activity as well as AGN/torus emission represents the ideal wavelength in which to conduct this research. This dissertation outlines the process necessary to conduct such a mid-IR survey and presents preliminary observations of three AGN. These AGN (NGC 4151, Cygnus A, and Mrk 231) show no strong circumnuclear starburst activity but are too few to accurately test evolutionary predictions statistically. However these observations show the advantages of mid-IR imaging in studying the relationship between AGN and starburst activity in the central kiloparsec of active galaxies.

CHAPTER 2
OBSERVATIONS AND INSTRUMENTATION

This chapter discusses the observations used in this dissertation. It begins with a discussion of the criteria for selection of the sample of Seyferts for this thesis as well as the observing strategy. In addition, information regarding instrumentation and standard techniques used in mid-infrared astronomy are discussed.

Sample Selection

In order to study the characteristics of a class of galaxies such as Seyferts, ideally one would observe all members of that class. Of course this is impractical due to the vast number of known Seyferts and limitations in acquiring time on large telescopes. Thus studies of galaxies such as Seyferts rely on the analysis of a sample of sources that are chosen to representative the class as a whole. However, it is difficult to select a sample small enough to be reasonably observable over time and yet large enough to adequately represent the entire class. Also depending on the selection criteria for a sample, subtle biases may be introduced. No incomplete sample of Seyferts is completely free from bias. Understanding the shortcomings of these samples is imperative when trying to project their characteristics onto the entire class. The following sections outline the advantages and disadvantages of several AGN samples. Although the goal of this dissertation was to observe large relatively unbiased sample of AGN by which to test the evolutionary hypothesis, in reality, due to poor weather and observing conditions only three AGN were observed. These three sources represent a beginning to surveys outlined below.

V/V$_m$ Test

One way to test the completeness of a galaxy sample is with the "V/V$_m$ test". First used by Schmidt (1968), this method tests if a sample is uniformly distributed in space. Let us consider a sample of optically selected Seyferts. For every Seyfert in the sample there corresponds two volumes.

$$V = \frac{4 \cdot \pi}{3} \cdot r^3 \qquad V_m = \frac{4 \cdot \pi}{3} \cdot r$$

where "r" is the distance to the Seyfert and "r$_m$" is the distance at which the flux "F" from the Seyfert reduces to the limiting flux of the sample "F$_m$".

$$r_m = \left(\frac{F}{F_m} \right)^{\frac{1}{2}}$$

Thus V is a measure of the actual volume enclosed by the Seyfert while V$_m$ is the volume enclosed if the galaxy were at a distance such that it would be at the flux limit of the sample. A Seyfert from a sample uniformly distributed in space is equally likely to be anywhere in the accessible volume. Thus values of V/V$_m$ for such a uniform sample should vary between [0, 1], resulting a sample mean value of 0.5. Mean values of V/V$_m$ other than 0.5 indicate a gradient in the density of the sample as a function of distance. Mean values of V/V$_m$ < 0.5 indicate an increase in number density towards the nearest parts of the accessible volume. This typically means that a sample is incomplete, missing faint objects which would normally fill the farthest part of the accessible volume. Mean values of V/V$_m$ > 0.5 suggest the opposite, that there is an increased number of galaxies at the outer extent of the volume. This can be seen in the case of quasars which typically show values of V/V$_m$ > 0.5 (Schmidt 1968) showing an increase in density with distance.

This suggests that quasars were more common in an earlier epoch of the universe. However in the case of quasars, the simple Euclidean geometry used to define the volumes V and V_m do not apply. At these large distances, the effects of an expanding universe must be taken into account. For all surveys discussed in this thesis however, distances are small enough such that a Euclidean approximation is justified.

Selection Criteria

One of the earliest Seyfert samples were the Markarian lists (Markarian 1967, 1969a, b, Markarian & Lipovetsky 1971). These samples however were selected on the basis of UV excess, which is not an isotropic property. If the unified model is accurate the orientation of the torus blocks 99% of the nuclear UV featureless continuum in Seyfert 2's, while one observes ~ 100% of the continuum in Seyfert 1's. Thus this method favors the selection of Sy 1 galaxies and only the brightest of Sy 2's. These lists also are biased against reddened and dusty nuclei in favor of the "bluer" Sy 1 nuclei. Similarly, samples selected by hard X-rays such as those by Piccinotti et al. (1982) also heavily favor Sy 1 nuclei whose central regions are relatively unobscured. In contrast samples selected according to their far-IR properties favor dusty nuclei whose bolometric luminosity is mostly reradiated by dust grains. Other IR selected samples such as the 12 μm sample (Rush, Malkan, & Spinoglio 1993) also are likely to be biased towards galaxies with strong star formation and bright nuclei.

Two of the best Seyfert samples are the CfA sample (Huchra & Burg 1992) and the Seyfert sample from Maiolino and Rieke (1995) (hereafter the MR95 sample). Both are magnitude limited spectroscopically selected (based on their optical emission lines) samples and thus do not suffer from the "blue-bias" associated with the Markarian lists. In addition they avoid the bias towards dusty nuclei and galaxies with strong star

formation which may occur in many IR selected samples. However as mentioned earlier, no Seyfert sample is completely free from bias; their advantages and shortcomings are discussed in detail below.

The CfA Seyfert Sample

The CfA Seyfert Sample (Huchra & Burg 1992) is drawn from 2399 galaxies in the merged Zwicky-Nilson catalog (Zwicky et al. 1961-1966; Nilson 1973). The sample is magnitude limited covering all galaxies with Zwicky magnitudes $m_{Zw}^2 \leq 14.5$ in the region of the sky $\delta \geq 0°$, $b_{II} \geq 40°$ or $\delta \geq -2.5°$, $b_{II} \leq -30°$. The values δ and b_{II} refer to galactic coordinates of latitude and longitude measured from the plane of the Milky way and from the center of the galaxy. Thus the sample is primarily observable from the Northern Hemisphere only. In addition, the sample contains a total of 48 Seyferts (26 Seyfert 1, 22 Seyfert 2) chosen solely on the basis of strong emission lines in their optical spectra. These Seyferts appear to be uniformly distributed in space with a mean V/V_m value ~ 0.5 and are 1-2 magnitudes brighter than those in the Markarian Survey (Huchra & Sargent 1973).

CfA Biases

However, the CfA sample is not without biases. The distance distributions of Seyfert 1's and 2's are not identical. Seyfert 1's have a much larger range of optical luminosities and are found at correspondingly greater distances. In addition, the sample is complete to a "total" magnitude of $m_{Zw} = 14.5$ and reaches out to relative high redshifts (z >0.03). This introduces the two main biases in the CfA sample discussed below.

---

[2] A roughly defined magnitude system from the Catalogue of Groups and Clusters of Galaxies (Zwicky et al. 1961-1968) which corresponds to a blue magnitude m_b. See Bothun & Cornell (1990) for an in depth discussion of the Zwicky magnitude system.

Bias against faint nuclei

The unresolved optical nucleus of a Seyfert grows fainter with the square of its distance, whilst the surface brightness of its host galaxy remains constant over a constant aperture. The more distant an object, the more difficult it becomes to recognize the AGN emission lines above the galaxy continuum as more of the host galaxy is included in the measuring aperture. It is therefore harder to identify the more distant objects as being Seyferts – especially relatively faint nuclei such as the Seyfert 2's, which lack strong broad lines – even though their total integrated AGN and host galaxy magnitude is above the survey limit (Kukula et al. 1995).

Bias against edge-on galaxies

Most Seyfert samples tend to lack Seyferts located in edge-on galaxies (McLeod & Rieke 1995). In general very few Seyferts are found in galaxies with axial ratios[3] ≤ 0.7 (Maiolino & Rieke 1995). This is not unexpected in magnitude limited samples as the higher absorption along the line of sight makes the nuclei more difficult to identify and shifts them above the limiting magnitude. However the CfA sample shows a stronger bias against edge-on systems than would normally be expected due to the higher redshift coverage.

The MR95 Seyfert sample

The goal of the MR95 (Maiolino & Rieke 1995) Seyfert sample was to address the two major biases of the CfA sample – namely the deficiencies in faint nuclei as well as edge-on galaxies. Like the CfA the MR95 sample is a magnitude limited

---

[3] Ratio of minor to major axes of the two dimensional projection of the galaxy on the sky. A face on galaxy would have an axial ratio of 1 while an edge on galaxies would have an axial ration close to 0. An axial ratio of ≤ 0.7 represents a galaxy tilted $\gtrsim 45°$ with respect to the line-of-sight from Earth.

spectroscopically selected sample, drawn primarily from the Revised Shapley-Ames

(RSA) catalog (Sandage & Tammann 1987) and including three extensions to it. It

contains 91 galaxies covering the whole sky (Northern and Southern Hemispheres) with a

limiting magnitude of $B_T^4 < 13.4$. Seyferts were divided into class 1 and 2 as well as

several intermediate types (1.2-1.9) using the ration of emission lines as defined by

Veilleux and Osterbrock (1987) and Whittle (1992). The classification scheme is defined

in Table 2-2.

Table 2-1: MR95 Seyfert Classification

Class	Description
Sy 1	Objects showing broad Hβ emission line and with [O III]/Hβ < 0.3
Sy 1.2	Objects showing broad Hβ and with 0.3 < [O III]/Hβ < 1
Sy 1.5	Objects showing broad Hβ and with 1 < [O III]/Hβ < 4
Sy 1.8	Objects showing broad Hβ and with 4 < [O III]/Hβ
Sy 1.9	Objects not showing broad Hβ, but having broad Hα; in these cases we check also the diagnostic ratio's of the emission lines as specified in the Seyfert 2 definition below
Sy 2	Objects lying in the AGN region in the Veilleux and Osterbrock (1987) diagnostic diagram (defined by their solid lines) and having [O III]/Hβ > 3 to exclude LINER's.

The MR95 shows a significant decrease in the biases associated with CfA by selecting

nearby Seyferts. The average distances of Seyferts in the MR95 sample (D ~ 35 Mpc) are

approximately one third the distance of the CfA sample (D ~ 100 Mpc). Thus the nuclear

spectra are less diluted by light from the host galaxy allowing the detection of fainter

---

[4] Total (asymtotic) magnitude in the B-system. This is the standard blue magnitude used in major galaxy catalogs such as RC2 and RC3 (de Vaucouleurs et al. 1976;1991). B_T magnitudes are usually about 0.4 mag brighter than B(0)-Zwicky magnitudes.
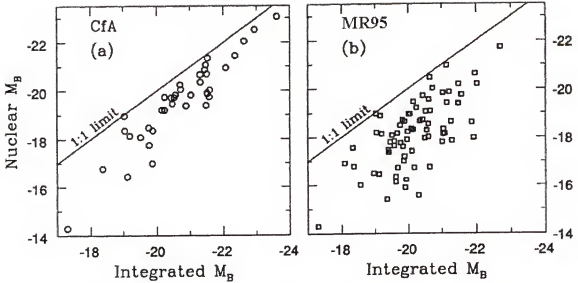
Figure 2-1. Plots of nuclear absolute magnitude (small-beam 16" aperture) vs. total integrated magnitude for (a) the CfA sample and (b) the MR95 sample. (From MR95). The 1:1 limit represents the unresolved limit where the total magnitude equals the nuclear magnitude.

nuclei. This is illustrated in Figure 2-7 (Figure 1 from Maiolino & Rieke 1995). This figure plots the nuclear absolute magnitude taken from small-beam photometry (typically 16") vs. the total integrated absolute magnitude. The CfA sample (Figure 2-1 (a)) shows a definite lack of nuclei which are weak in comparison to the integrated magnitude of the entire galaxy. In fact the distribution is closely related to the 1:1 limit or "resolution" limit where the nucleus cannot be distinguished from the host galaxy. As discussed earlier this bias has significant consequences for the detection of Type 2 Seyferts which are typically fainter than Type 1 and thus are under sampled in the CfA list. Figure 2-1 (b) shows the same analysis for the MR95 sample. This selection effect is greatly reduced as the sample regains many faint nuclei. However a 16" beam aperture may still contain substantial stellar contamination from the host galaxy. Thus Maiolino and Rieke also plotted the [OIII] λ5007 luminosity (a more direct indicator of nuclear activity) vs.
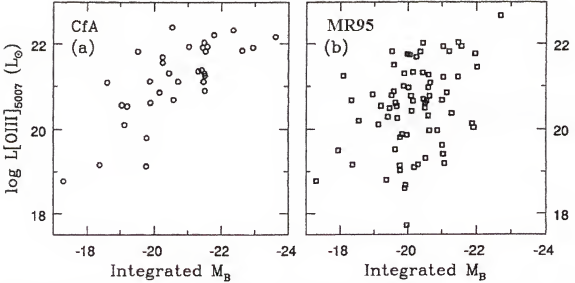
Figure 2-2. [OIII] luminosity vs. integrated absolute magnitude for (a) the CfA sample and (b) the MR95 sample. (From MR95)

integrated absolute magnitude for each galaxy. The results for both the CfA and MR95 samples can be seen in Figure 2-2 (Figure 2 from Maiolino & Rieke 1995). It is clear in the CfA sample that as the total galactic magnitude increases, a definite bias against faint, low activity nuclei is present, whereas this bias is greatly reduced in the MR95 sample.

In addition to recovering many low luminosity Seyfert nuclei, the MR95 sample also has a reduced bias against edge-on galaxies. In a magnitude limited sample, edge-on systems are expected to be less numerous due to the increased absorption of the intergalactic disk which acts to shift the nucleus beyond the limiting magnitude. Assuming galaxies are thin circular disks, this effect follows the distribution:

$$dN(r) \propto r^{3\beta/5} \, dr$$
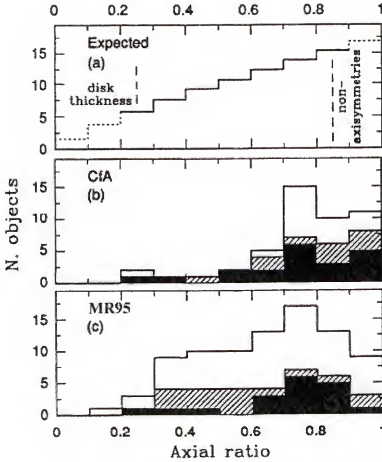
Figure 2-3. Axial ratio distributions for (a) expected for a magnitude limited sample of thin circular disks, (b) the CfA sample, and (c) the MR95 sample. Filled bars represent types 1, 1.2, and 1.5, shaded bars types 1.8 and 1.9, and empty bars type 2. Histograms are cumulative; in each bin the number of objects for each group is given by the difference in the height of the bars. (From MR95)

where r is the axial ratio, dN(r) is the number of galaxies with axial ratio's between r and

r + dr, and β =1.34 for spiral galaxies of type Sa-Sb (Sandage & Tammann 1987). This

simple relationship however does not account for nonaxisymmetric morphologies or the

thickness of the galactic disk and thus breaks down at high and low axial ratios

respectively. Figure 2-3 shows histograms of axial ratios taken from Maiolino and Rieke

(1995). Figure 2-3 (a) shows the expected distribution of axial ratios for a magnitude

limited sample as defined by the equation above (with an arbitrary normalization). Figure

2-3 (b) shows the distribution for the CfA sample. Notice the lack of Seyferts with axial ratios below 0.7. The CfA histogram also shows fewer low axial ratio systems than expected from a magnitude limited sample. Figure 2-3 (c) show the same analysis for the MR95 sample. It is clear that this sample is much more evenly distributed with a greatly reduced bias against edge-on Seyferts with low axial ratios. Deficiencies of Seyferts below r = 0.2-0.3 is expected due to disk thickness while those above r = 0.8 may be caused by non-circular disks (Binney & de Vaucouleurs 1981).

MR95 Biases

The MR95 sample greatly reduces two of the major biases associated with the CfA sample. However this sample also contains biases. The main reason that the MR95 accounts for more faint and edge-on Seyferts is due to its selection of nearby galaxies (mean D ~ 35 Mpc). Thus while the CfA sample is uniformly distributed in space with a mean V/Vm ~ 0.5, the MR95 sample is skewed towards nearby Seyferts represented by a mean V/Vm ~ 0.37 for the entire sample. Also although the MR95 sample recovers many faint and low luminosity nuclei missed by other samples, it still underestimates their number. The RSA catalog from which much of the MR95 Seyfert sample (B_T <13.4) was drawn from, is known to be incomplete above B_T >12.3 (Sandage et al. 1979). Completeness corrections applied over the whole RSA sample (Sandage et al. 1979) cannot be applied to the RSA Seyferts however due to the significantly different distributions (Maiolino & Rieke 1995). The RSA Seyferts show a much larger portion of bright galaxies probably due to the less complete identification of Seyfert nuclei in fainter and more distant members of the parent population. The heavier obscuration associated with Seyfert 2 AGN suggest that many of these missing faint galaxies will be in this class. Thus the MR95 still under samples faint low luminosity Seyferts and those located

at greater distances. However to date, the MR95 Seyfert sample represents one of the best surveys to include faint and edge-on galaxies.

Observing Strategy

All galaxies were observed in a consistent manner using both the N (~ 10 μm) and IHW18 (~ 18 μm) OSCIR filters (see Figure 2-8). These filters were chosen due to their wide passbands which offer the greatest sensitivity for these observations. In addition, for each galaxy observed there were additional observations of stellar sources. These stellar sources can be broken into two groups. The first is called a "standard star" and is used as a flux calibrator for the Seyfert observations (see Chapter 3). The second is used as a measure of the point spread function (PSF) of the telescope and instrument. This is used as a measure of the resolution and quality of observations throughout the night. In some cases observations of the standard stars were also used as a measure of the PSF.

Integration times for the MR95 sample based on observations using the Gemini 8 m telescopes were calculated as follows. Due to the "chop-nod" data acquisition (see later in Chapter 2) of the University of Florida mid-IR imager/spectrometer OSCIR, the average efficiency of observations is 25%. Thus a 15 minute exposure on-source (30 minutes chopped) would require 1 hr real-time. Integration times for the MR95 sample of Seyferts were based on previous 10 μm measurements (~ 5" - 15" aperture) from the literature for about 44 galaxies and IRAS (Infrared Astronomical Satellite) 12 and 25 μm measurements (~ 30" x 90" aperture) for the remaining 48. These were then scaled (by slope) to approximate flux densities expected from OSCIR N-band and IHW18 filters. Comparing 10 μm photometry taken at ~ 5" resolution to that from the large IRAS apertures showed that IRAS 12 μm measurements overestimated the nuclear fluxes by as

much as ~ 3 times in some cases. Thus, flux density estimates for Seyferts in the MR95 sample based on IRAS measurements were reduced by a factor of ~ 3 for all galaxies as a worst case scenario. Since many of these Seyferts may contain extended emission from star formation regions, it was assumed that the predicted flux was evenly distributed over a circular region with a radius ~ 100 pc. This represented a size typical of circumnuclear starbursts observed in these type AGN (Heckman et al. 1997; Colina et al. 1997; and Gonzalez-Delgado et al. 1998). Integration times of 4 minutes on-source (8 in chopped) yielded an average Signal to Noise ratio (S/N) of 10 per pixel at N, while 8 minutes (16 min chopped) yielded an average S/N of 12 per pixel at IHW18. For weaker sources, time of 10 minutes at N and 20 minutes at IHW18 were needed to reach a S/N in the range of 3-10 per pixel. Standard stars were typically observed for a total of 0.5 − 1 minute on-source while integration times for PSF stars ranged from 1-2 minutes on source. OSCIR can achieve a S/N of 3 on 0.16 mJy/pixel in 2 minutes on-source in N-band and a S/N of 3 on 0.9 mJy/pixel in 8 minutes on-source at IHW18 at Gemini. S/N values could be higher or lower depending on the accuracy of IRAS flux estimates as well as the extent and morphology of mid-IR emission.

AGN Sample

The objects observed in this dissertation represent a preliminary step in surveying a larger sample of Seyferts. Observations of these galaxies were performed in order to study their mid infrared properties as they relate to evolutionary predictions. These predictions suggest that observations should show an increase in extended mid-IR emission associated with circumnuclear starbursts as one progresses from Type 1 to Type 2 AGN. Due to extremely poor weather as well as telescope difficulties only three sources were obtained for this research. Two sources are Seyferts taken from the CfA and

MR95 sample. The third source though displaying many characteristics of a Type 2 Seyfert is more accurately identified as a powerful radio galaxy. This galaxy was chosen as a target of interest and as a preliminary step in analyzing the mid infrared properties of radio loud sources as they pertain to evolutionary models. Table 2-2 list the sources observed for this preliminary survey.

Table 2 - 2. Survey Galaxies

Name	AGN Type	Class	Telescope	Discussion
NGC 4151	1.5	Seyfert	Gemini N	Chapter 4
Cygnus A	2	FR II	Keck II	Chapter 5
MRK 231	1	Seyfert	Keck II	Chapter 6

Detecting Mid-Infrared Radiation

In order to detect mid-infrared (5μm - 25 μm) radiation from an astronomical source from ground based telescopes, it must first pass through the Earth's atmosphere. It is typically collected using a telescope which focuses the radiation onto an instrument commonly designed to detect such radiation.   A discussion of the path of mid-IR radiation through the Earth's atmosphere to the instrument is discussed below.

The Atmosphere

The Earth's atmosphere is not completely transparent to mid-IR radiation. As shown in Figure 2-4, the atmospheric transmission through the mid-IR regime has numerous strong absorption features caused by the Earth's atmosphere. Ozone (O_3) is responsible for many of these features including the strong absorption at 9.6 μm, while CO_2 causes the mid-IR transmission to drop to zero between 14 – 16 μm. Water vapor also absorbs

Atmospheric Transmission, Mauna Kea
(altitude=4200m, airmass=1.0, pwv=1.2mm, R=3000)
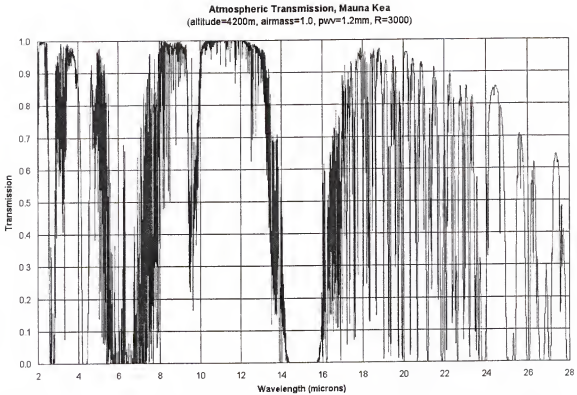
Figure 2-4. Atmospheric transmission. The 7-14 micron window can be seen clearly. Longer wavelength filters take advantage of the 16-30 micron window, which has numerous absorption features. (Image adapted from ATRAN model (Lord 1992))

in the mid-IR and results in many of the absorption features such as those seen in the wavelength regime between $16 - 30$ μm. At $\lambda > 40$ μm, the atmosphere is primarily opaque to radiation until the submillimeter regime. Astronomers typically observe at wavelengths where the atmospheric transmission is the highest, refereed to as atmospheric "windows". In the mid-IR there are two major windows. The first is located between 8 - 14 μm while the second is located between $16 - 30$ μm, often called the 10 and 20 μm windows respectively. Within these mid-infrared windows, there can be rapid variations in transmission due to changes in the water vapor column depth.

In addition to absorption, the atmosphere also emits strongly in the mid-IR peaking at ~ 10µm. Thus the atmosphere not only attenuates the mid-IR signal from an astronomical source, but also dilutes the signal with thermal emission of it's own. Separating the background sky emission from the source emission is one of the key elements in observational mid-IR astronomy.

Another affect the atmosphere has on observations is "seeing". This is a blurring affect caused by turbulence (density inhomogeneities in the atmosphere). This results in random fluctuations in refraction causing a star to vary in intensity and location on the sky (scintillate). This effect limits the angular resolution of all but the smallest optical telescopes. Ideally the image of a point-like source in the focal plane of a telescope should resemble a classical Airy disk (see Chapter 3). In practice however, time-averaged images resemble a two dimensional Gaussian distribution with a full width at half max rarely smaller than 1" at optical wavelengths. Seeing however is wavelength dependent with image size proportional to ~ $\lambda^{-0.2}$. Therefore longer wavelength mid-IR observations are much less affected by this phenomenon. This results in mid-IR images being primarily diffraction limited.

The Telescope

Both telescopes used in this dissertation (Gemini North and Keck II) are reflective systems following a Ritchey-Chrétien Cassegrain design. Figure 2-5 shows the general characteristics of this design which features a large "primary mirror" in the shape of a concave hyperboloid. The primary mirror bounces the light off a "secondary mirror" in the shape of a convex hyperboloid which then focuses the light through a hole in the primary mirror to the Cassegrain focus. These telescopes are typically classified by the size of their primary mirrors. The size of the primary is particularly important at mid-IR
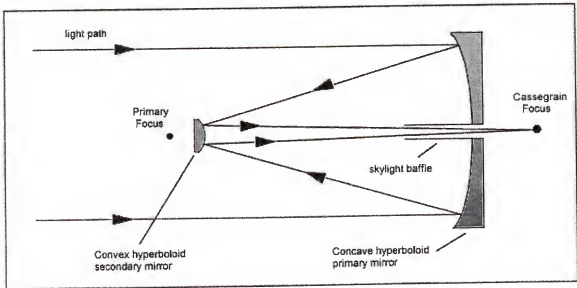
Figure 2-5. Ritchey Chrétien Telescope design.

Gemini
(8 meters)

Keck II
(10 meters)
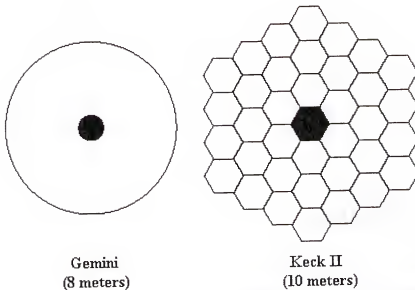
Figure 2-6. This image shows the relative sizes and configurations of the primary mirrors associated with the telescopes used in this project. Dark areas represent the central holes in each of these mirrors where light from the secondary is focused onto the instrument (see IFA University of Hawaii Information Bulletin 20, August 1995).

wavelengths. Since mid-IR observations in general are diffraction limited rather than seeing limited, the angular resolution of observations increases directly with the size of

the primary. Thus for a diffraction limited point source the sensitivity at mid-IR wavelengths is proportional to the diameter of the primary to the fourth power ($\sim D^4$) (Jones 1997). Thus, doubling the size of the primary increases its mid-IR sensitivity by a factor of sixteen.

The telescopes used in this project are listed in Table 2-3 along with the diameters of their primary mirrors. The 10 meter Keck II (along with it's twin the Keck I) is the largest optical/infrared telescope on Earth. This class is closely followed by the 8 meter Gemini telescopes which are also among the largest in the world. Figure 2-6 shows the relative sizes and forms of the primary mirrors used by both telescopes. Note how the Gemini telescopes use a primary formed from a single mirror while the Keck system uses a collection of thirty six small mirrors to act collectively as one large mirror. This was used as an alternative design method due to the technological difficulty in creating such a large single mirror.

Table 2 - 3. Telescope Characteristics

Telescope	Location	Elevation (ft)	Primary Diameter (m)
Keck II	Mauna Kea, Hawaii	13,647	10
Gemini North	Mauna Kea, Hawaii	13,824	8

In addition to the size of the primary mirror the location of the telescope is also important in the quality of the observations. Ideally a telescope should be located within a Hadley cell. Hadley cells are one of four cells created by convection on the Earth. These circulation patterns are characterized by strong up flows of air near the equator followed by a down flow at higher latitudes ($\pm 30°$). The up flowing air currents carry warm moist

air while the down flowing currents deposit cool dry air. Locations near the down flow of the Hadley cells thus benefit from dryer air resulting in greater atmospheric transmission at optical and infrared wavelengths. Observatories within a Hadley cell and devoid of surrounding mountain formations also take advantage of laminar air flow. This is a level flow of circulating air from inside a Hadley cell which greatly reduces atmospheric turbulence and seeing. Observatories should be at a sufficient altitude above the local inversion zone. This occurs when the ground cools faster than the sky forming a bend in the atmospheric temperature curve. Below the inversion zone the air is cooler than above trapping low level clouds and fog below. In addition, turbulence and convection are also reduced above a local inversion zone. Mauna Kea, Hawaii takes advantage of all these factors. This is considered one of the best locations for astronomy in the world and hosts observatories from eleven countries as well as both telescopes used for this dissertation.

OSCIR

Once the mid-infrared radiation from the astronomical source is collected by the telescope it passes through the entrance window into the instrument OSCIR (Figure 2-7). Except for the filters and the camera entrance window, OSCIR is an entirely reflective system. All of the mirrors in the optical path of OSCIR are gold-coated to take advantage of the high refelctivity gold has in the mid-infrared. Furthermore, except for the entrance window, the optics in OSCIR are cryogenically cooled with liquid nitrogen and helium. By cooling the optical components in this way, they do not contribute any thermal background. The detector is also cooled to cryogenic temperatures to suppress thermally generated dark current. Infrared cameras such as OSCIR have optics that reimage the telescope's focus onto the detector with a system of mirrors for two primary reasons. The
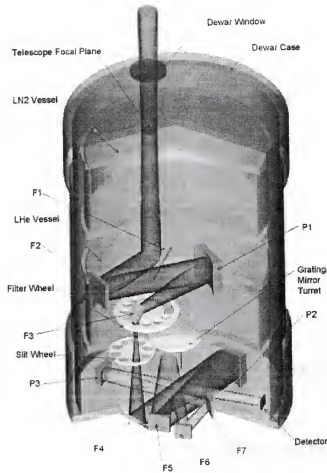
Figure 2-7. A cut-away view of OSCIR. This shows the path of light (dark gray cylinder) as it passes through the system optics. Both flat ('F') mirrors and parabolic ('P') mirrors are labeled and numbered in order. The 'LN2 vessel' is the canister that holds the liquid nitrogen, and the 'LHe vessel' is lower canister that is filled with liquid helium, and is responsible for cooling the detector to temperatures near 4 K. (Image provided by U.F. engineer Jeff Julian)

first is to achieve the desired plate scale at the detector at mid-IR wavelengths often

matched to the diffraction limit, and second is to create a pupil image within the cryostat.

There are two key reasons for wanting internal pupils:

- First, filters should be placed near a pupil and cryogenically cooled, to both reduce
  their thermal emission and ensure that the light collected is spread out over the entire

filter. Thus the light passing through the filters is less affected by small inhomogeneities.

- The second reason is that a "pupil stop" can be placed at the location of the pupil. This is done because a large background problem comes from stray light entering the camera system. In order to cut down this stray light, an aperture or "stop" is placed near the pupil image of the secondary mirror where it can reject stray light from outside the beam. This also reduces contamination from scattered light within the dewar. The stop is located internally where it can be cryogenically cooled (called a "cold" stop) so as too not contribute any thermal emission of its own.

Both the dewar entrance window and the filter complement are made of infrared transmitting materials. Since normal glasses become opaque in the near and mid-IR they are inappropriate for use in a mid-IR system like OSCIR. For the mid-IR a variety of crystalline substances are used instead. Natural crystals like Cesium Iodide (CsI) and Barium Fluoride (BaF2) are commonly used as well as man made substances like KRS5, each having different sets of advantages and disadvantages. The major disadvantage of natural crystals is that they tend to be very soft, and therefore are easy to scratch. The natural crystals, which are actually salts, are also hydroscopic. This makes them difficult to work with when one of the crystal surfaces would be exposed to water or high humidity. The main advantage of natural crystals like CsI and BaF2 is that they have a high transmission at mid-IR wavelengths. For example the transmission of CsI is well over 95% throughout the mid-IR regime. This is compared to a transmission of ~70% for a similar sized piece of KRS5. Man made materials like KRS5 and others also have the disadvantage of being toxic and therefore dangerous to work with. On the other hand, the man made materials are extremely strong and are mostly impervious to water. For most of OSCIR's scientific use the advantage of overall durability outweighed the gain in throughput and a KRS5 entrance window was used.
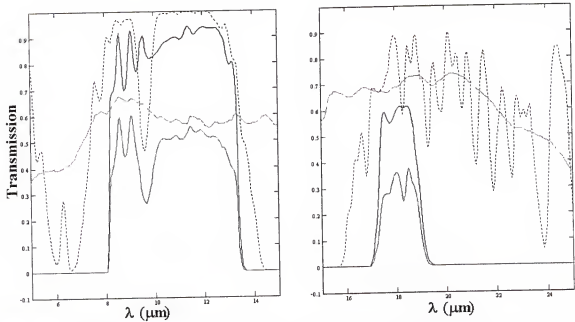
Figure 2-8. This figure shows the OSCIR N-band (left) and IHW18 (right) filters. Black lines represent the filter transmission, green represents the quantum efficiency (QE) of the OSCIR system, blue lines represent a smoothed estimate of the atmospheric transmission (ATRAN), and red represents the combination of all three resulting in the effective filter transmission (image created based on data provided by Robert Piña and the U.F. Infrared Astrophysics Group)

The custom entrance window assembly currently installed on OSCIR is comprised of two CsI lenses which have been anti-reflection (AR) coated and have a waterproof coating applied on top of the AR coating to protect the crystal surface. This assembly is also unusual in the sense that the lenses can be moved both independently of each other and in unison to achieve a precise focus of the telescope entrance beam. This is needed since the Gemini telescope produces a f/16 beam while OSCIR is designed to accept a f/35 beam. No special assembly was required to use OSCIR on the CTIO and Keck II since the focal ratios of those telescopes are f/30 and f/40 respectively. This however did result in minor vignetting by the cold stop in the dewar at CTIO, while the entrance beam at the Keck II was slightly undersized for optimal use with OSCIR.

The complement of filters in OSCIR is the only other place in the optical path where transmissive materials are used. All of the fourteen filters in OSCIR are multi-layer interference filters, and Table 2-4 lists their characteristics. These filters are designed to pass only a certain range of wavelengths. The filters are opaque to all other wavelengths by the interference properties of the filters themselves, and the transmission properties of the filter substrate material. The transmission of an interference filter within the passband is normally between 80% and 90%. Figure 2-8 shows the passbands of the OSCIR broadband N and IHW18 (International Halley Watch) filters. These are the OSCIR filters most used. This is due to a combination of their wide passbands providing high sensitivity as well as the high atmospheric transmission at the wavelengths of operation. These are also the filters used for all of the observations in this dissertation

Table 2-4: Characteristics of the OSCIR filter set.

Filter	Central Wavelength (μm)	Bandwidth (μm)
K (2.2)	2.20	0.42[a]
M (4.8)	4.80	0.60[a]
7.9	7.94	0.76
8.8	8.79	0.87
9.8	9.83	0.95
10.3	10.28	1.10
11.7	11.65	1.11
12.5	12.45	1.16
N (10.8)	10.38	5.23
IHW18 (18.2)	18.08	1.65
Qwide (17-24)	19.67	5.25[a]
Q3 (21)	20.75	1.65
LPF (20-29)	21.73	7.40[a]
H 25	24.13	3.60[a]

[a] Approximate bandwidths. Accurate to ± 0.2 μm.

The Detector

The detector in OSCIR is a Rockwell/Boeing 128x128 pixel, arsenic doped silicon (Si:As), blocked impurity band (BIB) array. It is an "extrinsic" semiconductor, as opposed to a CCD which is an "intrinsic" semiconductor. An intrinsic semiconductor is made from a pure semiconducting material that can interact with optical photons. The silicon in a CCD array interacts with an optical photon causing electrons in the semiconductor's valence band to be excited to the conduction band. The electrons in the conduction band are then free to conduct electricity, and thus charge can be read out.

However, silicon by itself does not effectively interact with photons of lower energy, such as mid-infrared photons. Instead extrinsic semiconducting materials are created such as silicon or germanium that has atoms in their crystalline structure deliberately replaced with other atoms, a process referred to as "doping". These "impurities", or "dopants", are atoms that can be excited by longer wavelength photons, hence providing electrons for the conduction band. The problem with doped photoconductors is that their quantum efficiency is dependent upon the concentration of dopant. However, too much dopant causes "tunneling" across the valence band, and this can lead to large dark currents. The only other choice is to make the photoconducting material lightly doped but very thick, which leads to many operational problems. A way of overcoming this is to use a "blocking band". By placing a layer of pure silicon between the doped material and the read-out contact, electrons cannot tunnel across the material. In this way, the infrared reactive material can be heavily doped to increase quantum efficiency, and the read out through the contact will be limited to electrons that were excited into the conduction band by interaction with a mid-infrared photon. The arsenic doped silicon BIB array employed in OSCIR is primarily sensitive to the wavelength regime from 5 to 25 μm.

Another fundamental difference between a BIB array and a CCD is the readout. CCD's employ a "charge-shift" readout, whereas the BIB arrays have discrete readout amplifiers for "each" pixel. This allows the BIB detector to be read out at an extremely fast rate as compared to CCD's.

Background Subtraction

As discussed earlier, the detector receives mid-IR radiation from more than just the astronomical source. This excess mid-IR emission is due to highly variable radiation from the sky (i.e. sky background), and the semi-constant background radiation from

telescope optics and the camera entrance window, commonly termed "radiative offset". In fact this combined background radiation dominates observations in the mid-infrared. For example, typical bright infrared standard stars used for flux calibration are frequently an order of magnitude fainter than the background emission. For scientifically interesting astronomical objects, which are typically much fainter than the standard stars, an observer may receive only 1 source photon for every 100,000 background photons.

One consequence of such high background levels is that the detector fills its wells very quickly. For example, using OSCIR at the IRTF it was found that the background emission within the N-band filter is typically $\sim 4 \times 10^{13}$ photons cm^{-2} s^{-1} (Fisher 2001). Given the high quantum efficiency of the detector, and a well depth of 22×10^6 electrons, the wells of the detector fill to $\sim 60\%$ in 20 ms. Obviously, these short frame integration times requires fast electronics to manage these high data rates. Additionally this extremely low ratio of source photon rate to background photon rate requires extremely accurate background flux subtraction to extract the signal of interest.

The Standard Chop-Nod Technique

The requirement of precise background subtraction dictates the method by which images are acquired at a telescope. Background subtraction is effected in real time using the standard infrared astronomical "chop/nod" technique. In this technique, the telescope is pointed at an object of interest (the "program object") and a set of images is acquired by the camera. An image consists of signal from the program object added onto the much larger signal from the background. The secondary mirror of the telescope is then moved slightly away from the nominal position so that program object moves out of the field of view of the camera and another set of images is acquired by the camera. This
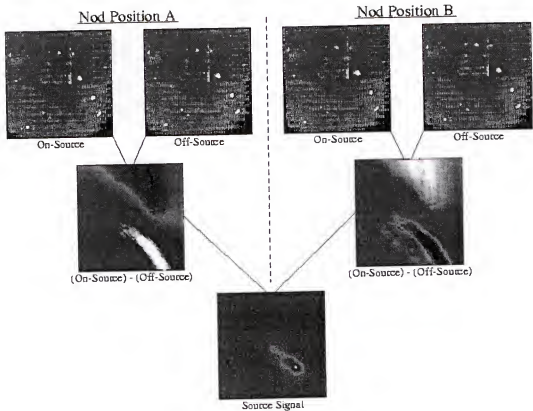
Figure 2-9. A schematic diagram of the chop/nod technique (courtesy Dr. Robert K. Piña).

procedure, called a "chop" cycle, is repeated many times at typically a 3-10 Hz rate moving back and forth between "on-source" and "off-source" positions. A "chop-differenced" signal is formed by taking the difference between the on-source and off-source images.

While this rapid movement of the secondary mirror allows subtraction of a spatially uniform background that is varying in time at frequencies below the chop frequency, it usually generates a spurious signal which may still be significantly larger than the source signal. This spurious signal, termed the "radiative offset," results from the fact that the emission pattern of the telescope, as seen by the camera, depends on the optical

configuration of the telescope. Movement of the secondary mirror changes this configuration, resulting in two different emission patterns. The difference in these emission patterns is found in the chop-differenced signal.

In order to remove the radiative offset, the entire telescope is moved after a short period of time so that the source now appears in what was previously the off-source position of the secondary mirror. This movement of the telescope is termed a "beam switch" or "nod" and typically occurs on timescales of tens of seconds. Timescales are much longer than that used in chopping due to slower changes in telescope emission relative to sky emission. Chop-differenced frames are then formed with this new on-source and off-source configuration. In this new configuration, the radiative offset will have changed sign and is effectively canceled when the new chop-differenced data is added to the old chop-differenced data (provided the telescope emission has not changed in the time between beam switching).

Figure 2-9 demonstrates the acquisition of data in the standard "chop/nod" mode. The images shown here were obtained with OSCIR at the IRTF. The top row of four images shows the raw data frames from the two secondary mirror positions at each of the two nod positions (called "Nod Position A" and "Nod Position B") of the telescope. These images are dominated by fixed-pattern offsets due to pixel-to-pixel variations and offsets between the 16 channels of the acquisition electronics. The background counts in these raw images correspond to 7.4×10^8 electrons s^{-1}. Each raw image consists of 5 minutes of total integration time (i.e. 15,000 frames coadded using a 20 ms frame integration time and the N-band filter) obtained in the chop/nod sequence as described above. The second row of two images shows the "chop-differenced" data derived from the subtraction of the

on-source and off-source data in the two nod positions of the telescope. Note that the dominant pattern (principally a gradient along the diagonal connecting the lower-left to upper-right corners of the images) changes sign between the two chop-differenced frames. However, since the subtraction is always done as "on-source minus off-source", the source signal remains positive in both chop-differenced frames. The signal levels in these differenced frames range $\pm 3.2\times10^6$ electrons s^{-1}, which is $\sim 0.4\%$ of the raw background signal. Finally, the bottom row shows the net signal obtained by adding together the two chop-differenced frames shown in the middle row (note that no other processing has been done to the data other than the additions and subtractions as described above). The detected source is the nuclear region of the starburst galaxy NGC 253. The net signal is the result of a total exposure of ~ 20 minutes in which half that time is actually spent imaging the off-source "reference" position. The signal level at the "tail" of this source near the middle of the frame is $\sim 6.4\times10^4$ electrons s^{-1}. This is about four orders of magnitude below the background level shown in the raw frame. In fact, the signal-to-noise ratio at this level in each pixel is about seven, so that the effective background subtraction is more nearly five orders of magnitude below the background.

CHAPTER 3
DATA REDUCTION AND ANALYSIS

This chapters discusses data reduction techniques as well as analysis used throughout this dissertation

Data Reduction

Data reduction is the process of converting observations taken at the telescope into a useable form for scientific analysis. This section will discuss the unique nature in which the data are saved using the instrument OSCIR (File Structure), followed by steps involved in the data reduction process. These include

- Removing Sub-Optimal Data Sets
- Cross Correlation
- Sky Subtraction
- Standard Star Calibration
- Airmass Calibration
- Flat Fielding
- Photometry
- Color Correction
- The PSF and Accounting for Pupil Rotation

File Structure

OSCIR data are saved in specialized six-dimensional FITS (Flexible Image Transport System) files. This file structure is a product of the chop/nod method used for mid-IR observations. These files were also created to save as much information as reasonably

possible from a single observation. The OSCIR detector is readout approximately every

$10 - 20$ ms during normal broad band observations. These $10 - 20$ ms images or data

frames are saved in an electronics rack connected to the back of the telescope near

OSCIR. Once every 2 seconds these frames are co-added in the electronics crate and sent

down a fiber optic cable to the OSCIR computer in the control room. The advantage of

this procedure is the observer has access to the entire data stream in two second quanta.

This does however result in large data files ranging from a 5-50 Mb or more depending

on the exposure time. Each file also contains a list of text called a "header" detailing all

the necessary information associated with the particular observation. The final format of

this header file may change slightly at different observatories since much of the

information gathered depends directly on the individual telescopes.

Removing Sub-Optimal Data Sets

A major advantage of the OSCIR data file structure is having access to the entire data

stream in two second quanta. This allows the removal of sub-optimal data sets which may

have occurred during the observation without affecting the other data sets. The primary

reason for removal of portions of a data stream is due to fluctuations in the background.

As discussed in Chapter 2, accurate background subtraction is imperative in mid-IR

observations. The quantity "%well" is a measure of the background seen by the OSCIR

detector. Figure 3-1 shows the "% well" as a function of frame number for an observation

of the Seyfert galaxy NGC 4051 during each of it's ~15 ms integrations. Experience has

shown that an acceptable background variation is < 0.5% change is "%well". Thus in the

case of NGC 4051, frames 150 - 260 were removed due to large changes in "%well"

during those readouts. This large change is most likely due to a faint band of

atmospheric cirrus moving though the field of view of OSCIR.
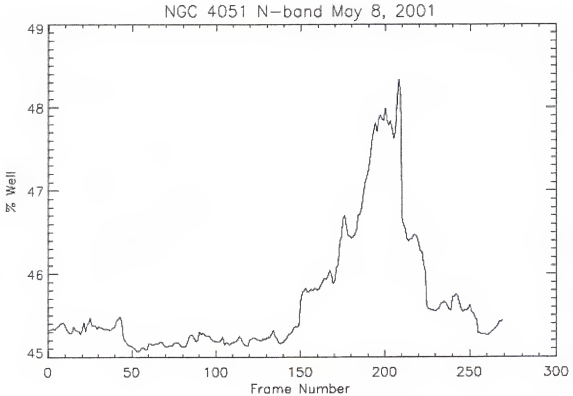
Figure 3–1. Background at N-band (10.8 µm) during an observation of NGC 4051 at Gemini North. This plot shows % well vs. frame number. During the reduction process frames 150-260 were removed due to large background change.

An additional source of data contamination may come from the OSCIR system itself. A small problem associated with the electronic readout of the detector array causes the occasional loss of one of the 16 independent readout channels. This results in rows of unresponsive pixels (see Figure 3-2). Fortunately this is a rare occurrence and is easily corrected. The horizontal row of bad pixels represents at most only 1/16th of the data. In most cases the science source does not cover the entire array, but rather only a small fraction further reducing the effects of these bad rows. A simple routine which replaces the bad channel with the median value of nearby pixels adequately accounts for this problem.
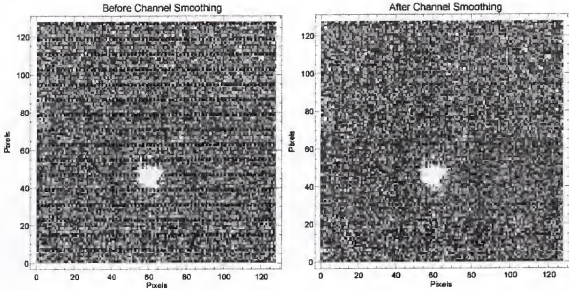
Figure 3-2. To the left is an image of Mrk 590 containing channel noise, right show the same image after the bad channel is smoothed using a median filter.

Cross Correlation

Once the sub-optimal data sets are removed, a series of signal "sig" frames remain. These "sig" frames are the final products of a complete chop-nod cycle, a single 128 x 128 image that has the background from the sky and telescope fully removed (see Figure 2-6). For most sources a "straight-stack" was performed. This is a direct sum of all the "sig" frames in an observation in which no processing was done. In some sources however there was a noticeable drift of the central source from frame to frame due to errors in tracking or differential refraction. In order to correct for this drift, the data was broken up into sets consisting of enough "sig" frames by which to achieve a sufficient S/N in order to centroid the source. The centroid of the source was measured in both x and y for each of these sets of data. This allowed a measurement of the drift rate which could then be accounted for by applying a shift-and-add to the entire data set.

Sky Subtraction

Another important data reduction step is sky subtraction. As mentioned in Chapter 2, accurate background subtraction is fundamental for mid-IR observations. The mean of the background or sky surrounding the science source in the final image should have zero counts. However even on a clear night and after removal of any contamination, the background of the final image often has a non-zero mean. In order to accurately calibrate the image this background level which the science source rests upon must be removed. To remove the sky background level the IDL routine "skyfit" designed by Drs. James De Buizer and Robert Piña was used. This routine allowed one to mask out the science source and fit the mean value of the remaining sky. This value was then subtracted resulting in a zero-mean count background. This program was also used when the sky background was non-uniform but showed structure that could not be removed by discarding sub-optimal data sets. In these cases after masking out the science source, rather than fitting a background level, a two dimensional polynomial surface was fitted and subtracted to achieve accurate sky subtraction.

Standard Star Calibration

On of the most important steps in data reduction is calibration of the science source. This involves converting from instrument units or Analog Digital Units (ADU sec^{-1} pixel^{-1}) which is measured with the instrument, to physical units such as millijanskys (mJy). This is done by observing what is called a "standard" star which has a well known spectral energy

Table 3-1: Standard Star Flux Densities

Standard Star	Flux Density (Jy)	
	10.8 μm (N-Band)	18.2 μm (IHW18)
α Lyr[†]	37.8	11.9
α CMa[†]	130.7	41.1
α CrB	5.0	1.8
α Boo[†]	682.7	219.1
α Hya[†]	125.2	41.5
α Tau[†]	600.6	200.1
β And[†]	245.9	83.9
β Gem[†]	115.5	37.0
β Gru	906.0	323.1
β Peg[†]	352.1	122.2
γ Aql[†]	77.2	25.6
γ Cru	833.9	286.7
γ Ret	72.6	28.7
λ Vel	194.6	69.4
μ UMa[†]	99.1	33.9

[†] Values are bandpass-averaged flux densities calculated by integrating Kurucz models of each star through the OSCIR filter bands also taking into account the detector QE, and atmospheric transmission. All other values come from the CTIO standard list (Fisher 2001).

distribution (SED). Using this SED the flux density (F_λ) in mJy is calculated for a standard star in a particular OSCIR filter taking into account standard atmospheric transmission and the measured quantum efficiency of the detector. This results in a measure of the brightness of the standard in ADU/sec from the telescope and an estimate

of the true flux density in mJy. The ratio of these two numbers results in a calibration value which converts each flux measurement into mJy. Table 3-1 shows a list of typical OSCIR standards used and their corresponding flux densities at N and IHW18 using SED models from Cohen et al. (1995).

Uncertainties associated with calibration are the dominant source of photometric error. The effects of atmospheric transmission typically dominate the photometric uncertainties in mid-IR. As discussed in Chapter 2, Figure 2-1, the mid-IR atmospheric windows at 10 and 20 μm have numerous atmospheric absorption features from water vapor, CO_2, and O_3. A variation in the column density of these species has a dramatic effect on the transparency and emission of the atmosphere in the mid-IR. Indeed, it is these variations of the sky background that requires the use of chopping in the mid-IR. Due to these limitations, uncertainties in absolute calibration of standard stars typically range from 5 - 10% for the 10 μm window, and upwards of 15% in the 20 μm window (van der Bliek et al. 1996). Observations in this dissertation show similar variations of 5-10% at N and 10-15% at IHW18 over the course of a single night.

Airmass Calibration

An additional factor in flux calibration involves the airmass. This is a measure of the distance from zenith and therefore is indicative of the volume of atmosphere one is looking through in which to observe a source. Airmass is defined by the equation (airmass = sec(z)), where z is the zenith angle. Ideally observations are done when the source is directly overhead when you are looking through the least amount of atmosphere (z=0°, airmass =1). In general, observations from this survey are at airmass < 2 (z<60°). The airmass corrections in the mid-IR for z < 60° are small. Under good sky conditions,

an approximate measure for the airmass correction in the N-band (10.8 μm) is ~ 0.02 mag/airmass. In this dissertation, airmass corrections were performed for all observations using measurements of the photometric calibrators over a range of airmass. At times this was impossible due to insufficient standard star observations, or obviously contaminated standard star data where there was no evident trend in the calibration values. In these cases photometric standards taken at the nearest time interval and closest in airmass to the science source were used. When there was sufficient data of good quality available, a linear regression of log(calibration value) vs. airmass was used to correct the science observations for airmass. These corrections rarely made a more than 5% change in the flux estimate for a calibrated source.

Flat Fielding

The pixel to pixel response of the OSCIR detector has a high degree of uniformity. Figure 3-3 shows an image of the OSCIR detector under uniform illumination in the N-band (10.8 μm) in chop mode only. Of the 16,384 pixels which make up the array, only 10 are unresponsive or "dead". A further 10 pixels are "hot" or show a significantly higher response than the others. There is also a small amount of vignetting within the instrument which can be seen as a dark area in the lower right corner of figure 3-3. The vertical line as well as the repeating horizontal structures are a "fixed pattern" that is removed during the chop-nod process. The overall flat-field of the array varies < 5%. Due to the uniform response of the array, in general no flat field corrections were applied to the data. In some cases during observations, background changes uniformly increased emission over the field of view. These frames are normally discarded (see Figure 3-1); however in post processing it is possible to recreate a flat field by comparing the high
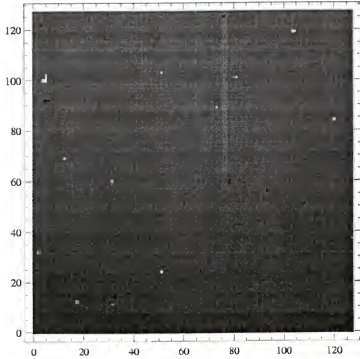
Figure 3-3. Image of OSCIR detector under uniform N-band illumination. The ~10 dead pixels are shown in black. The vignetting is in the lower right corner. The few white pixels are "hot" pixels that are active, but with signifigantly greater response than the others. The vertical line as well as the repeating horizontal structures are a "fixed pattern" that is removed during the chop-nod process.

background off-source frames to the low background off source frames. This was done in the case of two AGN; Cygnus A and NGC 4151. In both cases the flat field made negligible differences in the photometric measurements and no difference in source structure. Specifically, in the case of NGC 4151, flat fielding reduced the photometric measurements in the N-band by ~ 2% and by ~ 6% at IHW18. Similar results were found for Cygnus A. These measurements are within calibration error limits which dominate the uncertainty in the mid-IR. No such flat fielding was done in the case of Mrk 231.

Photometry

Photometry is typically used to accurately measure the flux density from the sources of interest. This is a rather simple step in which an aperture is placed over the source in

order to measure the total emission. This gives us the total flux density of the source in mJy. In stellar surveys where source confusion is not a problem it is common to use circular apertures of the same size for all data for consistency. Due to the varying morphology of AGN in this dissertation this method was not applicable. Aperture size and shape was determined in a case by case basis depending on the inherent morphology of the individual sources.

The size of the aperture used for photometry affects the uncertainty associated with the flux density measurement. This measurement error is directly proportional to the number of pixels included within the aperture (N_{pix}) and the mean standard deviation of the background (σ_{pix}) by the equation

$$error = \sigma_{pix} \sqrt{N_{pix}}$$

However even for the largest apertures used in this survey this error was small compared to the standard 5-15% photometric errors from standard star calibration.

Color Correction

In order to convert flux density measurements of science sources observed through wide bandpass infrared filters (such as N and IHW18) into monochromatic flux densities, a "color correction" needs to be applied. This step is necessary due to the different spectral energy distributions (SEDs) of the calibration star and the science object throughout the wide passbands. The photosphere of a calibration star typically ranges between 3000-10,000 K, resulting in an SED peak in the optical followed by a gradual fall off in emission through the mid-IR referred to as the Raleigh-Jeans tail of the Planck function. In the case of science targets, mid-IR emission is associated with heated dust at temperatures of a few hundred K. In this case the SED of the science target typically
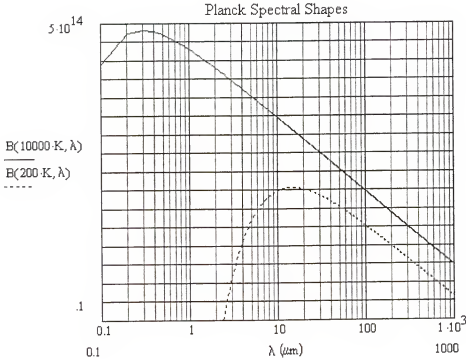
Figure 3-4. This graph shows the Planck function B(T, λ) vs. λ at two temperatures. The solid line represents a blackbody at 10,000 K typical of a calibration star while the dotted line is at 200 K typical of dust emission in the mid-IR. Note the contrast around 10 μm between the cresting of the sharp Wien side of the Planck function at 200 K vs. the declining Rayleigh-Jeans tail of the 10,000 K blackbody.

peaks in the mid to far-IR resulting in the sharp increasing Wien side of the Planck function passing through the mid-IR wavelength regime (see Figure 3-4). Since the calibration star and science objects have different SED's through the mid-IR, any monochromatic flux density given is dependent on the spectral shape of the source through the passband (see Figure 3-5).

The color correction factor assumes that the ratio of instrumental counts or for the calibration star (ADU^S) to that of the program object (ADU^P) is equal to the ratio of number of photons detected from the calibration star (N^P) to the program source (N^S).

$$\frac{ADU^P}{ADU^S} = \frac{N^P}{N^S} \tag{3-1}$$
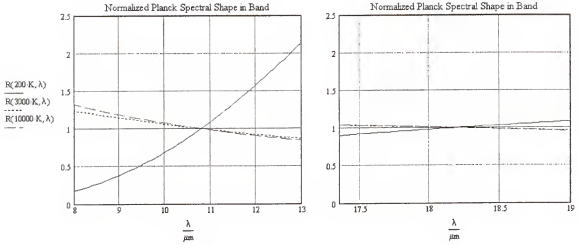
Figure 3-5. The left panel shows an enlarged view of the N-band which ranges from 8-13 μm. The right shows the IHW18 band. Here the blackbodies have been normalized so as to fit on the same y-axis. Both images clearly show the differing slopes of the hot stellar SED's (3000 -10,000 K) and the cooler science object SED (200 K). Note the greater effect at N than IHW18. (From MATHCAD program written by R.K. Piña)

The number of photons a source will generate through a bandpass is

$$N = \int Q_{sys} \frac{F_\nu}{h\nu} d\nu \qquad (3-2)$$

where F_ν is the flux density of the source at frequency ν and is defined as

$$F_\nu = \Omega \cdot \left(1 - e^{-\tau_\nu}\right) \cdot B_\nu(T) \cdot e^{-\tau_{\nu.ism}} \qquad (3-3)$$

where Ω is the solid angle subtended, τ_ν is the emission optical depth, $B_\nu(T)$ is the Planck function evaluated at temperature T, and $\tau_{\nu.ism}$ is the optical depth associated with the intervening interstellar medium (typically $\tau_{\nu.ism} \ll 1$ at mid-IR wavelengths). The "quantum efficiency" of the system, Q_{sys} is defined as

$$Q_{sys} = T_{atm}(\nu) \cdot T_{filter}(\nu) \cdot QE(\nu) \qquad (3-4)$$

where T_{atm} is the atmospheric transmission, T_{filter} is the transmission of the OSCIR filter, and QE is the quantum efficiency of the OSCIR detector all evaluated at frequency ν.

Substituting equation (3-3) into (3-2) results in

$$N = \Omega \cdot \int Q_{sys} \frac{\left(1 - e^{-\tau_\nu}\right) \cdot B_\nu(T)}{h\nu} d\nu \tag{3-5}$$

The factor Ω can be solved for in terms of a monochromatic flux density of a source, $F_{\nu o}$ at a temperature T.

$$\Omega = \frac{F_{\nu o}}{\left(1 - e^{-\tau_{\nu o}}\right) \cdot B_{\nu o}(T)} \tag{3-6}$$

Substituting equation (3-5) into (3-4) results in the number of photons produced by a source with flux density $F_{\nu o}$ through the passband of a filter as

$$N = \frac{F_{\nu o}}{\left(1 - e^{-\tau_{\nu o}}\right) \cdot B_{\nu o}(T)} \cdot \int Q_{sys} \frac{\left(1 - e^{-\tau_\nu}\right) \cdot B_\nu(T)}{h\nu} d\nu \tag{3-7}$$

Given from equation (3-1)

$$N^p = \frac{ADU^p}{ADU^s} \cdot N^s$$

and substituting equation (3-7) results in the equation below

$$\frac{F_{\nu o}^p}{\left(1 - e^{-\tau_{\nu o}}\right) \cdot B_{\nu o}(T^p)} \cdot \left[\int Q_{sys} \frac{\left(1 - e^{-\tau_\nu}\right) \cdot B_\nu(T^p)}{h\nu} d\nu \right] = \frac{ADU^p}{ADU^s} \cdot \frac{F_{\nu o}^s}{B_{\nu o}(T^s)} \cdot \left[\int Q_{sys} \frac{B_\nu(T^s)}{h\nu} d\nu \right]$$

Expressing this equation in terms of the flux density of the program source at a frequency ν_o yields

$$F_{vo}^{p} = ADU^{p} \cdot \left(\frac{F_{vo}^{s}}{ADU^{s}}\right) \cdot \left[\frac{\displaystyle\int Q_{sys} \frac{B_{v}\left(T^{s}\right)}{B_{vo}\left(T^{s}\right)} \cdot \frac{1}{hv} dv}{\displaystyle\int Q_{sys} \frac{\left(1-e^{-\tau\,v}\right) \cdot B_{v}\left(T^{p}\right)}{\left(1-e^{-\tau\,vo}\right) \cdot B_{vo}\left(T^{p}\right)} \cdot \frac{1}{hv} dv}\right]$$ (3-8)

Thus the monochromatic flux density of the program source F_{vo}^{p} is equal to its instrument

counts (ADU^{p}) multiplied by a calibration factor (F_{vo}^{s}/ADU^{s}) which is simply the flux

density of the standard star divided by its instrument counts. This in then multiplied by a

third term in brackets which is the color correction factor.

All flux densities in this dissertation were color corrected in this method with the

help of a MATHCAD routine written by Dr. Robert Piña. Given observations at two

filters (N and IHW18) and an estimate of the stellar temperature of the standard star, the

program iterates a solution to τ and T for the program source as well as the color

correction factor. The color correction factor typically increased the N-band flux density

evaluated at 10.8 μm ~ 15 % for the AGN in this sample. In the case of IHW18 the flux

density at 18.2 μm increased < 2% due to the much narrower passband ($\Delta\lambda = 1.6$ μm at

IHW18 compared to $\Delta\lambda = 5.2$ μm at N).

The PSF and Accounting for Pupil Rotation

The final data reduction step addresses the PSF. The primary function of a PSF

star is for comparison to the science object observed. It allows you to access whether the

source is resolved and the reliability of observed extended structure. Thus it is important

for the PSF to be taken as close to the science source in time and distance in the sky. If

observed too distant in time, atmospheric distortions may have changed between the two
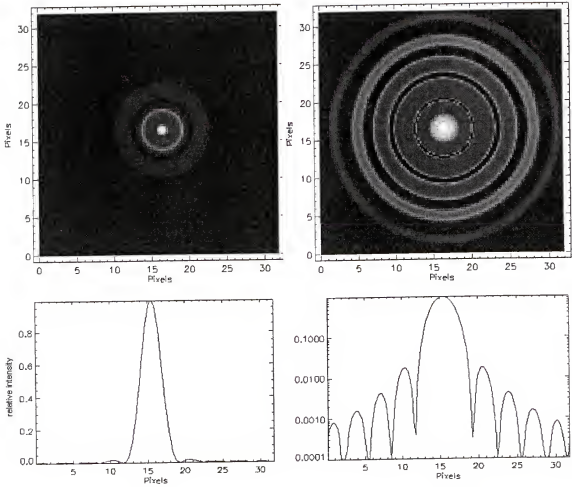
Figure 3-6. The top left side of this figure shows a model of the Airy PSF function at a λ = 10.8 μm on the 8 m Gemini North telescope followed below by a line cut through the image. The top right shows the same figure on a logarithmic scale to enhance the low level oscillatory features followed below by its associated profile. These images were created using an IDL routine written by Dr. Robert Piña.

observations. If observed too distant in the sky separation, differences in airmass and

flexure from the telescope may alter the PSF in comparison to the science source. The

PSF produced by a perfect optical system with a circular aperture is called the Airy

function. This function is oscillatory and displays a ring like shape. An example of the

Airy function associated with a telescope such as Gemini North can be seen in Figure 3-

6. Under perfect conditions the highest resolution achievable in the mid-IR is referred to
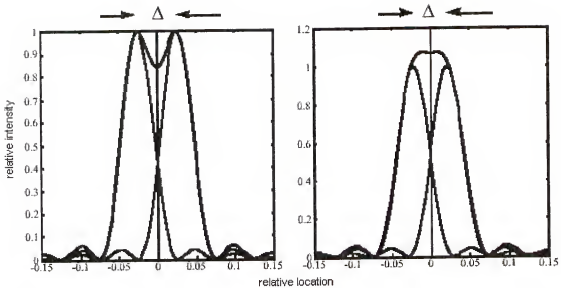
Figure 3-7. This image shows profiles of two PSFs along with their combined intensity profiles as defined by two resolution criteria. The left displays the Rayleigh criteria while the right image shows a schematic of the Sparrow criteria.

as the Sparrow criteria. Schematically this is defined as the point when two PSFs are separated such that the top of their intensity profile is flat (see Figure 3-7). Mathematically this is given as $\sim \lambda/D$ where λ is the wavelength of observation and D is the diameter of the telescope aperture. Also used as a measure of resolution is the Rayleigh criteria which is defined as the point where two PSFs are separated such that the peak of one point source falls on the first trough of the second point source and vice-versa (see Figure 3-7).

In the case of OSCIR on alt-az telescopes, such as the Keck II, Gemini North, and Gemini South, an additional factor concerning the PSF must be considered. This involves the rotation of the pupil from observations at different positions in the sky. An example can be seen with OSCIR mounted on the Keck II telescope. Figure 3-8 shows the PSF star Alpha Bootes taken with OSCIR at N-band at two different positions on the sky. The images are on a logarithmic scale to enhance low level emission in the
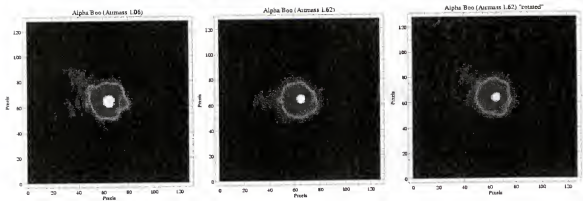
Figure 3–8. The leftmost image is the PSF star Alpha Boo taken at UT time 11:14 at an airmass of 1.06. The middle shows the same star taken at UT 13:31 at an airmass of 1.62. In both images North is up and East is left, but due to the different positions in the sky the pupil has rotated 40°. This is readily seen by the position angle of the extended distortion on the left side of images. The rightmost image shows the PSF after pupil rotation has been removed in order to match the first image.

diffraction pattern. The overall OSCIR-telescope optics are misaligned such that some optical distortion is present. This distortion can be seen as a prominent extension in the diffraction pattern on the left side of each image. The rotation of this distortion is due to the rotation of the Keck II telescope "pupil" as projected on the OSCIR detector array. In these images North is up and East is left at all times during the observation, only the pupil rotates. Thus in order to accurately compare the PSF and the science source, the pupil orientation of both images must also be aligned. This is done by using the image header information provided from each observation. The header file records the exact beginning and ending mirror positions for each observation. The difference between these positions from one observation to the next provides the degree of pupil rotation. As you can see from Figure 3-8 this is an important step in data reduction in order to compare the PSF and the science object to confirm that extended emission surrounding the science source is real and not due to distortion from the telescope optics.

An additional minor PSF reduction step involves the rotation of the pupil over different integration times. In general the PSF is very stable throughout the night allowing one to compare a PSF taken with a short integration (~ 1 min) to that of a science object taken with a longer integration (~ several minutes). However the pupil rotates slightly more during a longer integration than a shorter one as the telescope tracks across the sky. In order to account for this PSF images were rotationally 'smeared' to account for this slight rotation of the pupil. This smearing effect was accomplished by adding a series of PSF images rotated at increments of 0.1° up to the total degree of pupil rotation and normalizing. In all cases the difference in pupil rotation from long to short integrations was small (< 4°).

Analysis

After the data has been properly reduced, analysis of the observations follows. Below discusses the steps that were used to analyze all sources in this dissertation. These are

- Measuring the Unresolved Component
- Color Temperature/ Optical Depth Calculations
- Determining the Luminosity
- Properties of Dust Grains

Measuring the Unresolved Component

The first analysis performed on the science data involved determining whether a source was resolved or not, and if yes, the contribution from the unresolved component. This was accomplished by comparing the reduced science data with the PSF. The PSF was centered on the source peak, scaled to the same peak and subtracted. In the case of Mrk 231 there were no significant residuals and the source was considered unresolved.

This was confirmed by measuring the FWHM of both the source and the PSF, though at 10 μm this method showed that Mrk 231 may be marginally resolved (see Chapter 6). In the cases of NGC 4151 and Cygnus A, the residuals were significant, representing > 25% of the total flux density of the individual sources. These structures were often reminiscent of morphology observed at several other wavelengths. These objects were considered resolved. In the case of these resolved galaxies the contribution to the total flux density from the unresolved component was estimated. This was achieved by measuring the flux density of the PSF scaled to the same peak as the source. This typically represented an upper limit to the emission from the black hole driven central engine and/or torus which could not be resolved (see Chapter 5 for more detail).

Color Temperature / Optical Depth Calculations

Assuming uniform temperature and optical depth, one can estimate the 'color' temperature and emission optical depth using the ratio of observations taken at two wavelengths. This can be calculated by solving the standard solution of the radiative transfer equation at two frequencies.

$$F_{\nu 1} = \Omega \cdot \left(1 - e^{-\tau_{\nu 1}}\right) \cdot B_{\nu 1}(T) \cdot e^{-\tau_{\nu 1.ism}} \tag{3-9}$$

$$F_{\nu 2} = \Omega \cdot \left(1 - e^{-\tau_{\nu 2}}\right) \cdot B_{\nu 2}(T) \cdot e^{-\tau_{\nu 2.ism}} \tag{3-10}$$

Here, F_ν is the observed flux density at frequency ν, Ω is the solid angle, τ is the emission optical depth, $B_\nu(T)$ is the Planck function evaluated at frequency ν and temperature T, and $\tau_{\nu.ism}$ is the extinction from the intervening interstellar medium (ISM). As mentioned in Chapter 1, assuming a Mathis (1990) interstellar extinction curve, mid-IR emission

suffers 25-75 times less extinction than optical wavelengths. Thus extinction from the ISM was considered negligible and the term $e^{-\tau v.ism}$ is assumed to be ~1. Further assuming that the mid-IR emission from the science object is optically thin, the term $(1-e^{-\tau v})$ is approximated by τ_v. The emission optical depth is then

$$\tau = \pi \cdot a^2 \cdot Q_{abs}(a, v) \cdot N \cdot L \qquad (3\text{-}11)$$

Where 'a' is the dust grain radius, $Q_{abs}(a, v)$ is the mid-IR absorption efficiency, N is the grain number density, and L is the path length. Kirchoff's law tells us that $Q_{abs}=Q_{em}$. The frequency dependence of dust grain emission efficiency in the mid-IR can be approximated as $Q_{em}(a, v) \propto v^1$, thus $\tau \propto v^1$. Therefore using the above assumptions and assuming optically thin emission equations (3-9) and (3-10) reduce to

$$F_{v1} = \Omega \cdot \tau_{v1} \cdot B_{v1}(T) \qquad (3\text{-}12)$$

$$F_{v2} = \Omega \cdot \left(\tau_{v1} \frac{v1}{v2} \right) \cdot B_{v2}(T) \qquad (3\text{-}13)$$

Since F_{v1} and F_{v2} is measured from the data, two unknowns τ_v and T remain. An IDL program written by Drs. Elisha Polomski, James De Buizer, and I was developed to simultaneously solve for T and τ, using an initial estimate of the temperature and emission optical depth. The program uses equations (3-12) and (3-13) above to iterate a solution. Given that the observed flux density depends both on the source size and emission optical depth, τ cannot be determined for unresolved sources, only the product $\Omega\tau$ can be solved for. In these cases however an upper limit to the source size can be

given by the FWHM of the PSF. A lower limit to the source size can also be determined assuming the source is an optically thick blackbody; $F_\nu = \Omega B_\nu(T)$, and simultaneously solving for Ω and T.

In the case of resolved sources flux density maps were created by convolving calibrated images at N with the IHW18 PSF and vice-versa to attain the same resolution at both wavelengths. Color temperature and emission optical depth maps were calculated based on the ratio of these images. Since no astrometric calibration was performed due to the limited field of view of OSCIR, the peak flux of the convolved N-band image was aligned to coincide with peak flux of the convolved IHW18 image. The structures of temperature maps were highly dependent on the alignment of the two convolved images. In order to determine the errors due to alignment, a Monte Carlo simulation was performed by shifting the two convolved images with respect to each other up to two pixels (~ 0.15") in all directions. In general, temperature values were most stable in the core varying ~ 5-10 K, with variations of 15-20 K at the edges of emission regions due to lower S/N. As mentioned earlier the frequency dependence of dust grain emission efficiency in the mid-IR is usually approximated as $Q_{em}(a, \nu) \propto \nu^1$. A steeper power law dependence such as $Q_{em}(a, \nu) \propto \nu^2$ would only decrease the calculated temperatures ~ 15% and would correspondingly increase the emission optical depth by a factor of ~ 3.4.

Determining the Luminosity

The true luminosity of the sources in this dissertation is very difficult to determine. First, the entire SED which is needed in order determine a bolometric luminosity, is not always complete for all the survey galaxies. Second, in general many of these measurements were taken with much lower resolution than this survey. As a consequence

they typically represent a total galactic luminosity including many regions outside our field of view. Third, extinction is difficult to determine and can be very variable with wavelength, thus hiding the true luminosity. And finally, many AGN may emit anisotropically, thus the luminosity measured in the direction of the Earth may be a few to a few hundred times less than that of other lines-of-sight. Thus bolometric luminosities from the literature for galaxies in this survey were analyzed in a case by case basis.

A luminosity based on mid-IR measurements can also be calculated. The mid-IR provides and excellent trace of the bolometric luminosity in AGN (Alonso-Herrero et al. 2002). Evidence for this can be seen in the work of Spinoglio and Malkan (1989) which found that the 12 μm flux is approximately a constant fraction of the bolometric flux in Seyferts. In addition this provides us with a consistent method by which to determine the luminosity of sources in this sample. Mid-infrared luminosities were computed by integrating the Planck function from 1 to 600 μm at the derived dust color temperature and optical depth for each source, again using the emissivity function $1-e^{-\tau}$, assuming emission into 4π steradians, and using the estimated distance, D, to the source

$$L=4\cdot\pi\cdot D^2\left[\pi\cdot\left(\frac{a}{2}\right)^2\right]\cdot\int_{1\,\mu m}^{600\,\mu m}\left(1-e^{-\tau_\nu}\right)\cdot B_\nu(T)\,d\nu$$

This equation is for resolved sources, and is different for the blackbody and optically thin limits, since it is a function of source size, a. For the blackbody (optically thick) limit, the extinction term drops out, and the source size used is a_{bb}. For the optically thin limit this equation becomes

$$L_{thin}=4\cdot\pi\cdot D^2\cdot(\Omega\tau)\cdot\left(\int_{1\,\mu m}^{600\,\mu m}B_\nu(T_{thin})\,d\nu\right)$$

where $\Omega\tau$ is the product found above.

Properties of Dust Grains

A prominent source of mid-IR radiation is emission from dust grains. The Color

Temperature/Optical Depth section discussed how using mid-IR observations at two

wavelengths provides a temperature estimate of these grains. Temperature calculations

assist in exploring the characteristics of dust grains around the science object as well as

the mechanisms by which the grains are heated.

In studying the effects of radiation on dust grains the grain extinction efficiency Q_{ext} is

defined as

$$Q_{ext} = Q_{abs} + Q_{sca}$$

where Q_{abs} is the absorption efficiency and Q_{sca} is the scattering efficiency. The emission

efficiency of dust grains is given by Kirchoff's law which tells us that $Q_{abs} = Q_{em}$ at any

given wavelength. The quantity Q_{abs} is calculated by solving Maxwell's equations for the

incident absorbed radiation with appropriate boundary conditions at the grains surface.

Values of Q_{abs} are dependent on the size, shape, and composition of the dust grains. For

simplicity, dust grains in general are approximated as spherical. Dust grains composed of

silicate and graphite (and occasionally carbon) are most often used due to their good

approximation of extinction laws measured within the ISM such as Mathis et al. (1990).

Extensive calculations of Q_{abs} have been performed by Draine and Lee (1984), Laor and

Draine (1993), and Weingartner and Draine (2001). Figure 3-9 shows values of Q_{abs} vs. λ

for grains of varying sizes composed of "smoothed astronomical silicate" and graphite.

Dust grains in the interstellar medium typically fall within the range of 0.003-1μm
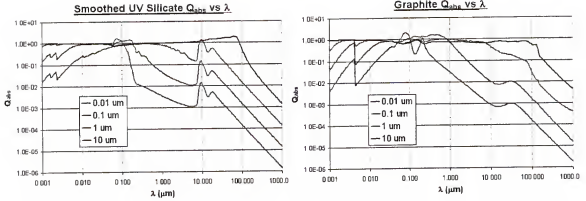
Figure 3-9: Values of Qabs vs. λ for several grain sizes ranging from 0.01 μm – 10μm for dust grains composed of "smoothed astronomical" silicate (right) and graphite (left)

(Draine & Lee 1984). Due to the long wavelengths in the mid-IR (5-25μm) scattering off these small grains is negligible. Figure 3-10 compares Q_{abs} and Q_{sca} vs. λ. Notice how Q_{sca} drop significantly as the wavelength approaches 10 μm.

The rate of energy absorbed by a dust grain is given as

$$\left(\frac{dE}{dt}\right)_{abs} = \int_0^\infty \pi \cdot B_\nu\left(T_s\right) \cdot \pi \cdot a^2 \cdot Q_{abs}(a,\nu) d\nu \tag{3-14}$$

where $\pi B_\nu(T_s)$ is the flux from the illuminating source at frequency ν and temperature Ts measured at the location of the dust particle. The equation can be rearranged by multiplying by a value of 1 defined as

$$\frac{\int_0^\infty \pi \cdot B_\nu\left(T_s\right) d\nu}{\int_0^\infty \pi \cdot B_\nu\left(T_s\right) d\nu}$$

This allows us to define the Q_{abs} in terms of a Planck averaged absorption efficiency
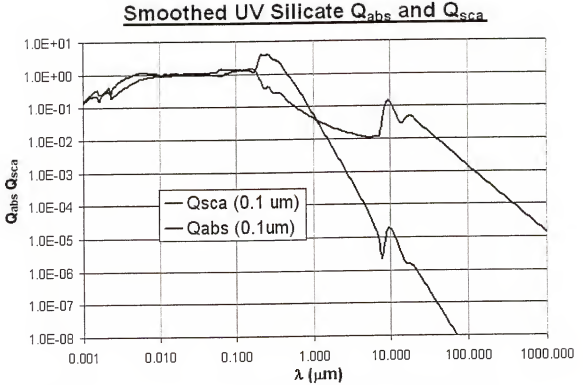
Figure 3-10. Comparison between Qabs and Qsca for 'Smoothed UV silicate'.

$$\overline{Q_{abs}(a, T_s)} = \frac{\displaystyle\int_0^\infty \pi \cdot B_v(T_s) \cdot Q_{abs}(a, v) \, dv}{\displaystyle\int_0^\infty \pi \cdot B_v(T_s) \, dv} \tag{3-15}$$

By taking into account the Planck function this averaged absorption efficiency is

dependent on temperature rather than frequency. The flux emitted by the source can also

be thought of in terms of the source luminosity by

$$\int_0^\infty \pi \cdot B_v(T_s) \, dv = \frac{L_v}{4 \cdot \pi \cdot r^2} \tag{3-16}$$

Where L_ν is the luminosity at frequency ν and 'r' is the radius from the central source at which the dust grains are located. Substituting equation (3-15) and (3-16) into equation (3-14) give us

$$\left(\frac{dE}{dt}\right)_{abs} = \frac{L_\nu}{4 \cdot \pi \cdot r^2} \cdot \pi \cdot a^2 \cdot \overline{Q_{abs}\left(a, T_s\right)} \tag{3-17}$$

The above equation defines the rate of energy absorbed by a dust grain. The rate of energy emitted is defined as

$$\left(\frac{dE}{dt}\right)_{emit} = \int_0^\infty \pi \cdot B_\nu\left(T_d\right) \cdot 4 \cdot \pi \cdot a^2 \cdot Q_{em}(a, \nu)\, d\nu \tag{3-18}$$

Applying a similar rearranging of variables as above this equation can also be expressed in terms of a Planck averaged emission efficiency

$$\left(\frac{dE}{dt}\right)_{emit} = 4 \cdot \pi \cdot a^2 \cdot \overline{Q_{em}\left(a, T_d\right)} \cdot \int_0^\infty \pi \cdot B_\nu\left(T_d\right) d\nu \tag{3-19}$$

Given Stefan Boltzman's law which states,

$$\int_0^\infty \pi \cdot B_\nu\left(T_d\right) d\nu = \sigma \cdot T_d^{\,4} \tag{3-20}$$

equation (3-19) can be simplified to

$$\left(\frac{dE}{dt}\right)_{emit} = 4 \cdot \pi \cdot a^2 \cdot \overline{Q_{em}\left(a, T_d\right)} \cdot \sigma \cdot T_d^{\,4} \tag{3-21}$$

Assuming radiative equilibrium, the rate of energy absorption is equal to the rate of energy emission

$$\left(\frac{dE}{dt}\right)_{abs} = \left(\frac{dE}{dt}\right)_{emit}$$

or

$$\frac{L_v}{4 \cdot \pi \cdot r^2} \cdot \pi \cdot a^2 \cdot \overline{Q_{abs}(a, T_s)} = 4 \cdot \pi \cdot a^2 \cdot \overline{Q_{em}(a, T_d)} \cdot \sigma \cdot T_d^4 \qquad (3\text{-}22)$$

If the dust grains are perfect blackbodies then they emit and absorb equally at all

wavelengths and $Q_{abs}/Q_{em} = 1$ and these terms drop out. However, as discussed earlier,

dust grains primarily absorb ultraviolet (UV) wavelengths and re-emit this energy in the

infrared (IR). Thus the right side of the equation (3-22) is dominated by UV frequencies

while the left is dominated by IR frequencies. Therefore it can be written as

$$\frac{L_{UV}}{4 \cdot \pi \cdot r^2} \cdot \pi \cdot a^2 \cdot Q_{UV} = 4 \cdot \pi \cdot a^2 \cdot Q_{IR} \cdot \sigma \cdot T_d^4 \qquad (3\text{-}23)$$

where L_{UV} is the source luminosity at UV wavelengths and Q_{UV} and Q_{IR} are the Planck

averaged emissivity efficiencies at UV and IR wavelengths respectively. This equation

can also be expressed in terms of the radius of the dust from the luminosity source by

$$r = \left(\frac{L_v}{16 \cdot \pi \cdot \sigma \cdot T_d^4} \cdot \frac{Q_{UV}}{Q_{IR}} \right)^{\frac{1}{2}} \qquad (3\text{-}24)$$

Note the effects of the dust grains attenuating the source radiation are neglected as is

scattering and grains heating each other by IR radiation. These assumptions however are

justified when the optical depth of the dust is <<1 at optical/UV and IR wavelengths. For

a more accurate analysis of grain heating a radiative transfer calculation needs to be

performed. However equation (3-24) can provide a first order approximation of the

distance at which dust exists from a source of luminosity

CHAPTER 4
CASE STUDY: NGC 4151

NGC 4151 is one of the nearest (13.2 Mpc, $H_0 = 75$ km s^{-1} Mpc^{-1}) and best studied

active galactic nuclei (AGN). The nucleus hosts a highly variable continuum and line

emission source. Continuum variability, first reported by Fitch et al. (1967), has been

observed at several wavelengths including X-ray (Papadakis et al. 1995), UV (Clavel et

al. 1990), and optical (Lyutyi 1972). Classified as a Seyfert 1.5 by Osterbrock and Koski

(1976), NGC 4151 displayed characteristics of a Seyfert 2 (Penston & P'erez 1984)

during a low luminosity state in 1984, and at a later date characteristics of a Seyfert 1

(Ayani & Maehara 1991). The mid-infrared emission from NGC 4151 has been

suggested to arise from either thermal emission from dust grains or synchrotron emission.

Discussions of the thermal vs. nonthermal origin of the infrared emission in NGC 4151

can be found in Rieke and Lebofsky (1981), Edelson and Malkan (1986), Carelton et al.

(1987), Edelson et al. (1987), and de Kool and Begelman (1989). A direct method to

investigate the origin of the mid-IR emission mechanism, as proposed by Neugebauer et

al. (1990) (hereafter N90), is a measurement of the size of the emitting region. They

suggest that a nonthermal self-absorbed synchrotron source would be < 1 mas, and hence

unresolvable. However, if the mid-IR emission is due to heated dust grains, the size of the

region would be > 0.1" . Observations show that the mid-IR emission in NGC 4151 is

compact. Comparison between 60" resolution IRAS 12 µm flux density measurements

and 6" resolution ground-based 10.6 µm measurements agree to within ~ 6% (Edelson et

al. 1987). Mid-IR observations by Rieke and Low (1972), Rieke and Lebofsky (1981),

and Ward et al. (1987) also did not detect any extended emission with resolutions ~ 6". Observations by ISO (Infrared Space Observatory; Rodriquez-Espinosa et al. 1996 - hereafter RE96) show a strong warm dust component in NGC 4151 and suggest a thermal origin from a geometrically and optically thick dusty torus and/or a dusty narrow line region (NLR). These observations however were at a resolution of 180". Using a technique of near-simultaneous north-south scans at 2.2 μm and 11.2 μm, N90 was able to resolve the 11.2 μm emitting region to be 0.16"±0.04". However this technique measured the size in only one spatial direction and was insufficient to explore the mid-IR morphology of the circumnuclear region. In addition, these north-south scans could not investigate the NLR of NGC 4151 which is primarily orientated in an east-west direction. This chapter presents high resolution mid-IR imaging which, to the best of our knowledge, resolves the inner NLR of NGC 4151 for the first time at 10 μm and 18 μm.

Observations and Data Reduction

Observations and Data Reduction Observations of NGC 4151 were made on 7 May 2001 using the University of Florida mid-infrared camera/spectrometer OSCIR on the Gemini North 8-m telescope. OSCIR uses a Rockwell 128 x 128 Si:As Blocked Impurity Band (BIB) detector. On Gemini North, OSCIR has a plate scale of 0.089" pixel^{-1}, corresponding to a field of view of 11.4" x 11.4" Images were obtained in the N ($\lambda_0 = 10.8$ μm, $\Delta\lambda = 5.2$ μm) and IHW18 ($\lambda_0 = 18.2$ μm, $\Delta\lambda = 1.7$ μm) filters using a standard chop/nod technique to remove sky background and thermal emission from the telescope. The chopper throw was 15" in declination at a frequency of 3 Hz and the telescope was nodded every 30 seconds. NGC 4151 was observed for a total chopped integration time of 360 seconds at 10.8 μm and 480 seconds at 18.2 μm. Observations of β Gem were taken for flux calibration and as a measure of the telescope point spread function (PSF).

Measurements of other calibration stars throughout the night showed flux calibration variations of less than 5% at 10.8 μm and less than 10% at 18.2 μm. Absolute calibration of β Gem was achieved using a spectral irradiance model by Cohen (1995) adjusted for filter and atmospheric transmission. The calibration value and FWHM were also color corrected to account for the different spectral slope of β Gem versus NGC 4151 as observed within our N and IHW18 filters. The measured color corrected FWHM of β Gem was 0.53" at 10.8 μm and 0.58" at 18.2 μm based on a 60 second chopped integration. Short integrations of β Gem were sufficient for comparison to NGC 4151 due to the stability of the OSCIR/Gemini PSF. Observations of several standard stars including β Gem, μ Uma, and γ Aql showed variations in the FWHM of < 6% throughout the night. Finally, observations of NGC 4151 showed no change in structure when divided into increments of time equal to that of the PSF (60s). OSCIR was mounted on the telescope with the Gemini instrument rotator oriented such that north was up and east was left on the detector array. In post-processing, images of the PSF star β Gem were ``unrotated'' -17.4° and -22.9° at 10.8 μm and 18.2 μm respectively to match the position angle of the Gemini North telescope pupil as projected on the detector array when NGC 4151 was observed. This is necessary to correctly account for the rotation of the telescope pupil with respect to OSCIR (during an observation or when changing pointing) due to the alt-az mount of the Gemini North telescope. In addition, PSF images were rotationally "smeared" to account for the slight rotation of the pupil (≤ 4°) during the exposure times of NGC 4151. Flux density maps were created by convolving images at 10.8 μm with the 18.2 μm PSF and vice-versa to attain the same resolution at both wavelengths. Color temperature and emission optical depth maps were calculated based

on the ratio of these images. Since no astrometric calibration was performed due to the limited field of view of OSCIR, the peak flux of the convolved 10.8 μm image was aligned to coincide with peak flux of the convolved 18.2 μm image. Temperature and emission optical depth were then calculated using the optically thin approximation $F_v = \Omega \tau B_v(T)$, where F_v is the observed flux density at frequency v, Ω is the solid angle of each pixel, τ is the emission optical depth, and $B_v(T)$ is the Planck function evaluated at frequency v and temperature T. The structure of the temperature map was highly dependent on the alignment of the two convolved images. In order to determine the errors due to alignment, a Monte Carlo simulation was done by shifting the two convolved images with respect to each other up to 0.1" in all directions. Temperature values were most stable in the core varying ±5 K, with variations of ±15 K further out. The frequency dependence of dust grain emission efficiency in the mid-IR was approximated as $Q(v) \sim v^1$. A steeper power law dependence such as $Q(v) \sim v^2$ would decrease the calculated temperatures ~ 15% and correspondingly increases the emission optical depth by a factor of ~ 3.4.

Results

NGC 4151 shows extended emission ~ 3.5" across oriented in an approximately east-west direction. Perpendicular to the extended emission (roughly north-south) the galaxy remains unresolved based our limiting resolution of ~ 0.53" - 0.58" at 10.8 μm and 18.2 μm respectively. Figure 4-1 shows our N-band image of the central ~ 400 pc (~ 6") of NGC 4151. Subtraction of the unresolved (PSF) component scaled to 100% of the peak results in a hole at the center of the residual emission. Since this may represent an over-subtraction of the unresolved component, residuals are shown after subtraction of the PSF scaled to 90%, 80%, and 70% of the peak of NGC 4151. Figure 4-2 shows a
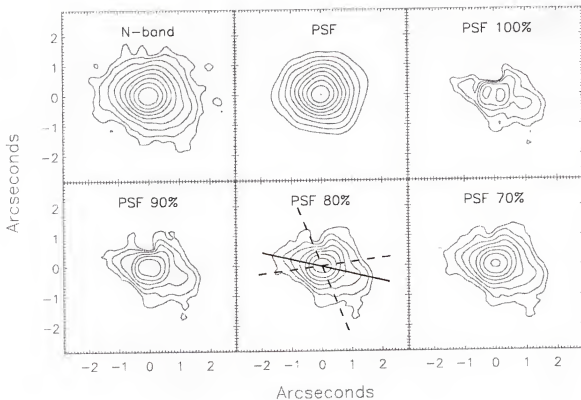
Figure 4-1. N-band images of the central ~ 6" of NGC 4151. All images are smoothed with a ~ 0.25" gaussian filter to enhance low level emission and scaled logarithmically. The lowest contour represents the 3 σ level of the smoothed data (0.086 mJy). The next image shows the PSF star β Gem scaled to the same level as NGC 4151 for comparison. The next four images show the residuals of NGC 4151 after subtraction of the PSF (unresolved component) scaled to 100%, 90%, 80%, and 70% of the peak height. In the 80% image dashed lines delineate the edges of the ionization region as observed by Evans et. al. (1993) while the solid line represents the radio jet axis. With the peak scaled to the same height as NGC 4151 (100%), the unresolved component represents ~ 73% of the total emission detected at 10 μm.

similar comparison at 18.2 μm. Both figures clearly show extended mid-IR emission on a

much larger scale than previously measured. The extent and position angle (~ 60°) of the

extended emission is coincident with the NLR as observed by Evans et al. (1993) and

Kaiser et al. (2000) using HST. This NLR was resolved at [OIII] λ5007 into a number of

emission line clouds distributed in a biconical structure oriented along a PA = 60° ± 5,

with an opening angle of 75° ± 10 (Evans et al. 1993). NGC 4151 also contains a radio jet
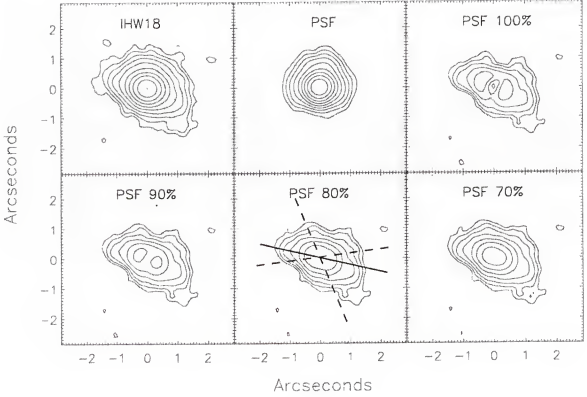
Figure 4 - 2. IHW18 images of the central ~ 6" of NGC 4151 in the same format as Figure 1. The lowest contour represents the 3 σ level of the smoothed data (0.46 mJy). With the peak scaled to the same height as NGC 4151 (100%), the unresolved component represents ~ 73% of the total emission detected at 18 μm.

(Johnston et al. 1982; Pedlar et al. 1993; and Mundell et al. 1995) which extends along a

slightly different PA (~ 77°) than the [OIII] emission. Figure 4-3 shows our mid-IR

images overlaid on the [OIII] and radio maps in the central ~ 6". The extended mid-IR

emission strongly coincides with the [OIII] emission out to a distance of ~100 pc from

the nucleus on either side. As previously mentioned, north-south scans by N90 measure

the 11.2 μm emitting region to be 0.16"±0.04" or ~ 10 pc. No extended emission is seen

in this direction resulting in an upper limit to the mid-IR size of ≲ 35pc based on our

resolution limit of ~ 0.53" - 0.58". Scaling the PSF to 100% of the peak of NGC 4151

results in an upper limit of the unresolved component of ≲ 73% of the total emission at

10.8 µm and 18.2 µm and a lower limit to the extended component of $\gtrsim 27\%$. Table 4-1

shows our mid-IR flux density measurements.

Table 4-1. NGC 4151 Flux Density Measurements

Description	Filter	Aperture (arcsec)	Flux Density (mJy)
Total	N band	4.5	1874 ± 52[a]
Unresolved (≤ 73 %)	"	[b]	$\leq 1368 \pm 38$
Extended (≥ 23 %)	"	[b]	$\geq 506 \pm 14$
	Long Wavelength		
Total	IHW18	4.5	4386 ± 241[a]
Unresolved (≤ 73 %)	"	[b]	$\leq 3202 \pm 176$
Extended (≥ 23 %)	"	[b]	$\geq 1184 \pm 65$

[a] All flux densities are color-corrected and in units of millijanksy.
Errors in .flux density are dominated by uncertainty in calibration (2.5%
at the N band and 5% at IHW18)but also include a small statistical error
based on the aperture size.
[b] Flux density measurements were performed by scaling the PSF star
Gem to 100%of the peak of NGC 4151 and subtracting off to find the con-
tribution from the resolved and unresolved component.
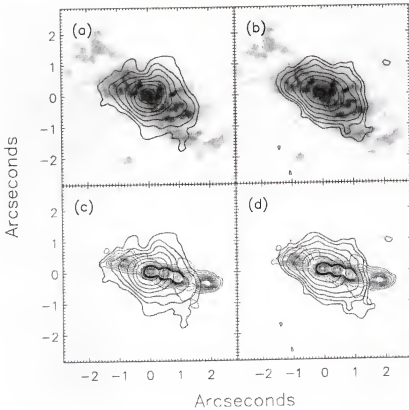
Figure 4-3. Contours represent the extended emission at N and IHW18 after PSF subtraction (with PSF scaled to 80% of the peak). Images (a) and (b) show the extended N and IHW18 emission respectively overlaid on the HST [OIII] ionization region as observed by Kaiser et al. (2000). Image (c) and (d) show the same N and IHW18 emission overlaid on the radio jet as observed at 18 cm by Pedlar et al. (1998). In all images the peak emission in the radio and [OIII] are aligned to correspond with the peak in the mid-IR.

Analysis and Discussion

Based on the conclusion from N90 that a nonthermal self-absorbed synchrotron source would be < 1mas, and hence unresolvable, our results are consistent with a thermal origin of the extended mid-IR emission. The re-radiation by dust grains heated by either stars or an AGN may result in this extended thermal mid-IR emission. However, processes such as fine structure emission lines may also produce extended mid-IR emission. Several mid-IR fine structure lines were observed by Sturm et al. (1999) using ISO. Four of these emission lines fall within our broadband N and IHW18 filters and may contribute to this

mid-IR emission. These emission lines are the 8.99 μm [ArIII], 10.51 μm [SIV], 12.81 μm [NeII], and 18.71 μm [SIII]. However based on flux measurements from Sturm et al. (1999), these emission lines contribute < 10% of the extended emission observed at 10.8 μm and 18.2 μm. Several mechanisms can contribute to thermal dust emission in the mid-IR. These in- clude shock heating, in-situ star formation, dust in the NLR heated by the central engine, and a dusty torus. Each is considered below in the context of the mid-IR emission detected in NGC 4151.

Dust Heated in Shocks

Shock heating of dust grains caused by the radio jet may contribute to mid-IR emission in NGC 4151. Mid-IR emission from shocks may be produced by either direct collisions between the plasma and dust particles (Draine 1981) or absorption of UV radiation produced by the postshock cooling plasma (Dopita & Sutherland 1996). However, radial velocity measurements of Kaiser et al. (2000) show no correspondence between velocity or velocity dispersion and the positions of the radio knots of NGC 4151. Models by Crenshaw et al. (2000) also do not require strong shocks to explain the kinematics of the NLR. Shocks may still contribute to the NLR as suggested by Contini et al. (2002), but are not considered to be a major source of ionization. Recent [Fe II] observations by Turner et. al. (2002) also support this concept. Thus shocks heating, though not ruled out, is not considered as a major source of the mid-IR emission observed.

Star Formation

Mid-IR emission has been observed to arise from star formation in the central regions of many galaxies (e.g. Telesco 1988). The mid-IR provides an excellent trace of HII star forming regions whose emission peaks at far-IR wavelengths (50-200 μm). Observations

by Engargiola et al. (1988) at 155 µm show extended emission (> 48") primarily in an east-west direction. ISO far-IR observations by RE96 measure this emission as a cold dust component (36K) consistent with dust heated in HII regions (Telesco et al. 1980). However, observations by Pérez-Fournon and Wilson (1990) in Hα show these HII regions exist in an elliptical galactic bar at a radius of ~ 50" (~ 3 kpc) from the nucleus. Thus these star forming regions cannot contribute to the mid-IR emission observed within our ~ 11" field of view. Star formation in the circumnuclear region of NGC 4151 has been characterized using the strength of polycyclic aromatic hydrocarbon (PAH) emission. Galaxies with strong nuclear star formation also feature strong PAH emission. This PAH emission however is found to be weak or absent in AGN with weak star formation (Roche et al. 1991; Genzel et al. 1998). In the case of NGC 4151, Roche and Aitken (1985) and Imanishi et al. (1998) failed to detect PAH emission at 11.4 µm and 3.3 µm respectively with their ~ 4" apertures. Further observation by Sturm et al. (1999) also failed to detect any PAH emission at 11.2 µm, 8.7 µm, 7.7 µm, or 6.2 µm. Thus the mid-IR emission observed on a scale of ~ 3.5" is unlikely to be associated with significant star formation.

Dusty Narrow Line Region

The most likely explanation for the ``extended'' mid-IR morphology in NGC 4151 is emission from a dusty NLR (Rieke et al. 1981; RE96). Dust in this region has a direct view of the central engine and hence can be heated resulting in extended mid-IR emission. The emission observed follows the NLR as delineated by the [OIII] observations of Kaiser et al. (2000), lending support to this concept. Mid-IR emission coincident with [OIII] NLR emission has also been observed in other galaxies such as NGC 1068 (Braatz et al. 1993, Cameron et al. 1993) and Cyg A (Radomski et al. 2001,
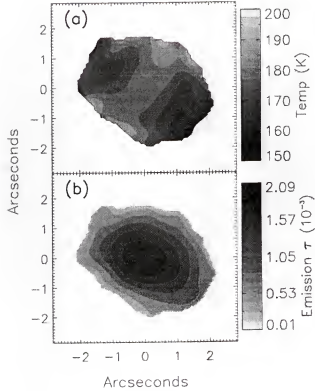
Figure 4-4. Temperature (a) and emission optical depth map (b) of the central ~ 6" of NGC 4151. Temperature peaks along the very outer edges are erroneous and most likely due to low signal-to-noise.

2002). In both galaxies dust heated by the central engine most likely contributes to this emission. In order to explore the possibility of central heating color temperatures based on the ratio of our 10.8 μm and 18.2 μm images were calculated. Temperature and emission optical depth maps from simple radiative transfer analysis provide a good first-order estimate of the sources of grain heating as well as the relative density of warm grains (Tresch-Fienberg et al. 1987). Figure 4-4 shows our temperature and emission optical depth maps. Color temperatures calculations range from ~ 185±5 K in the core to ~ 165±15 K within the NLR (r ~ 100 pc), consistent with the warm dust component (170 K) as measured by ISO (RE96). The emission optical depth shows the density of these

dust grains is enhanced along the direction of the NLR. Assuming a simple uniform dust distribution, a first-order determination of the size of the region that could be heated by a central source can be made. Given that dust grains primarily absorb UV-optical radiation and re-emit in the infrared, the equilibrium temperature of dust in a strong UV field is given by (Sellgren et al. 1983)

$$r = \left(\frac{L_v}{16 \cdot \pi \cdot \sigma \cdot T_d^4} \frac{Q_{UV}}{Q_{IR}} \right)^{\frac{1}{2}}$$

In the above equation, T is the dust temperature, L_{UV} is the UV luminosity of the central source, r is the radius from the source in parsecs, σ is the Stefan-Boltzman constant, and Q_{UV}/Q_{IR} is the ratio of the Planck averaged UV absorption coefficient to the infrared emission coefficient. Values of Q_{UV}/Q_{IR} are dependent on the dust grain size and composition and are given by Draine and Lee (1984), Laor and Draine (1993), and Weingartner and Draine (2001) for graphite and "smoothed astronomical" (SA) silicate. The observed UV-optical luminosity of NGC 4151 is ~ 10^{10} $L_\odot$ (Penston et al. 1990). Given this luminosity, in order to heat dust to the observed temperature of ~ 165 ± 15 K at a distance of ~ 100 pc, the inner NLR should be composed of 0.004 μm graphite grains or 0.001 μm SA silicate grains. These grain sizes fall near or below the limit of classical interstellar dust grains which range from 0.003 μm - 1 μm (Draine & Lee 1984). They also are much smaller than the estimated grains sizes used for the centrally heated NLR models of NGC 1068 (~ 0.05 μm; Cameron et. al. 1993) and Cyg A (~ 0.1 μm; Radomski et. al. 2002). However Penston et al. (1990) proposed that the continuum emission in NGC 4151 is inherently anisotropic and that the ionizing luminosity as seen within the extended NLR (1-2 kpc) may be on order of 13 times greater than that observed from

Earth. Subsequent models by Schulz and Komossa (1993), Yoshida and Ohtani (1993), and Robinson et al. (1994) also derive values for the anisotropy as high as 3-10. Thus a better estimate of the luminosity in the NLR may be $\sim 10^{11}$ L$_\odot$. This higher luminosity would increase the calculated grain sizes by an order of magnitude (0.04 μm graphite or 0.01 μm SA silicate), resulting in sizes more consistent with classical interstellar dust and grain size estimates in the NLRs of NGC 1068 and Cyg A. Thus to first order, assuming that the luminosity in NGC 4151 is anisotropic, the extended mid-IR emission is consistent with heating of dust in the NLR from a central engine.

Dusty Torus

Another source of mid-IR emission in NGC 4151 may be from a dusty torus (RE96). Emission from a dusty torus may dominate the unresolved mid-IR component in NGC 4151. It is considered that this disk/torus is viewed through a line-of-sight passing near the boundary edge (Cassidy & Raine 1996). Assuming the torus lies perpendicular to the NLR, it's major axis would be oriented in an approximately north-south direction. No extended emission is seen in this direction resulting in an upper limit to the mid-IR size of the torus of $\lesssim 35$ pc based on our resolution limit of $\sim 0.53"$ - $0.58"$. This is consistent with the polarimetry observations and subsequent modeling of Ruiz et al. (2002) which suggest that the torus size in NGC 4151 is ≈ 30 pc. A direct measurement of the torus may have been made by N90. As previously mentioned, north-south scans by N90 measure the 11.2 μm emitting region to be 0.16"$\pm$0.04" or $\sim$10 pc. Based on our "unresolved" (PSF) component an upper limit can be placed on the mid-IR contribution of a dusty torus of $\gtrsim 73\%$ of the total emission at 10.8 μm and 18.2 μm. This represents the maximum contribution from a dusty torus and does not rule out contribution to the

Arcsecond   Onion-Skin Model
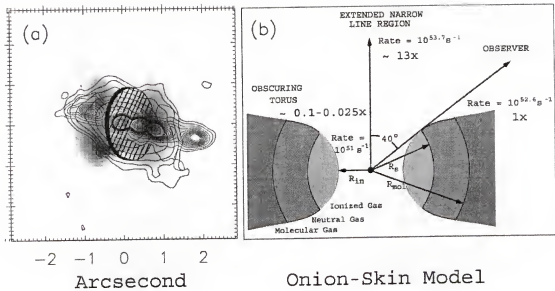
Figure 4-5. Image (a) shows four sets of data. First is the proposed HI disk from Mundell et al. (1995) (cross-hatched disk). Second, is the molecular H 2 1-0 S(1) ring as observed by Fernandez et al. (1999) (grey-scale). Both these images are overlaid on the 18 cm radio image from Pedlar et al. (1998) (narrow contours). Finally, the larger contours represent our 18.2 μm image from Figure 4-2 with the subtracted PSF scaled to 80%. Image (b) shows the ``onion-skin'' model of the gaseous torus from Pedlar et al. (1998)(their Figure 6). The rate values are the ionizing photons per second as calculated from Penston et al. (1990) (NLR and Observer) and Pedlar et al. (1998) (torus). The rate of 10^{51} s^{-1} is based on the lower limit from Pedlar et al. (1998). The upper limit is ~ 3 times greater, resulting in a range of ionizing flux 0.1-0.025 times as great as observed from Earth.

"unresolved" mid-IR emission from a self-absorbed synchrotron source. Observations of

neutral HI and molecular H 2 by Mundell et al. (1995) and Fernandez et al. (1999)

respectively, show evidence of a gaseous disk up to 2.5" (160 pc) across which may be

associated with the torus. This disk is located in approximately a north-south direction

and may consist of an "onion-skin" morphology as discussed by Pedlar et al. (1998). In

this model the gaseous torus contains several layers (see Figure 4-5). The innermost ring

consists of ionized gas followed by a ring of neutral HI gas surrounded by a ring of

molecular H_2. In Pedlar's "onion-skin" model the authors further expand on the subject of

anisotropy in NGC 4151 as discussed by Penston et al. (1990). Using observations of free-free absorption detected at 73 cm and 18 cm in conjunction with observations of HI by Mundell et al. (1995) they estimate the ionizing flux incident on the torus. Assuming a simple Strömgren model they calculate that the ionizing flux in the plane of the torus is between ~10 - 40 times less than seen from Earth or ~ 100 - 500 times less than seen in the NLR as modeled by Penston et al. (1990). To test the validity of this model the dust equilibrium equation from the Dusty Narrow Line Region section can be used. Given values for temperature and dust grain size discussed above the size of the mid-IR torus as a function of ionizing luminosity, L_{UV} can be calculated. Color temperature measurements of the core of NGC 4151 show T ~185±5 K. If the dusty torus intercepts the ionizing luminosity as seen from Earth ~ 10^{10} $L_\odot$ and consists of dust grains similar to those estimated for the NLR (0.04 μm graphite or 0.01 μm SA silicate), the size of the torus in the mid-IR would be ~ 0.65" (~ 42 pc). This is slightly larger than the size of the torus based on our resolution limit of ~ 0.53" - 0.58" (≲ 35 pc) and that of the Ruiz polarimetry model (≈ 30 pc). It is also 4 times larger than the north-south scans by N90 which measured the 11.2 μm emitting region to be 0.16"±0.04" or ~ 10 pc. Assuming the N90 mid-IR emission delineates the torus, dust grains in the torus would need to be ~10 times larger than that found in the NLR. Alternatively, if the luminosity in the plane of the torus is ~ 10 - 40 times less than seen from Earth as modeled by Pedlar et al. (1998), the size of the torus in the mid-IR would range between ~ 0.1" - 0.2" (~ 7 - 14 pc). Although slightly smaller than the Ruiz model, this size torus would be consistent with our upper limit as well as closely match the size measured by N90. Thus the "onion-skin" model of Pedlar et al. (1998) which suggests that the luminosity in NGC 4151 may be

very weak in the plane of the torus is roughly consistent with size estimates of the torus

in the mid-IR. However, it should be noted that the results discussed above derive from

simple equations involving Strömgren radii and dust grains at equilibrium temperatures.

Due to the increased density of material associated with the torus as opposed to the NLR,

a more robust radiative transfer analysis may be needed to truly understand the

anisotropy in NGC 4151.

Conclusions

In conclusion, extended mid-IR emission at 10.8 µm and 18.2 µm is detected in the

circumnuclear region of NGC 4151. This emission extends approximately ~ 200 pc (~

3.5") at a P.A. ~ 60° correlating with the NLR region as seen in [OIII] λ5007 by Evans et

al. (1993) and Kaiser et al. (2000) using HST. With the PSF scaled to 100% of the peak

of NGC 4151, limits to the unresolved and resolved components are measured as $\lesssim 73\%$

and $\gtrsim 27\%$ respectively. Mid-IR line emission contributes < 10% of the extended

emission at 10.8 µm and 18.2 µm. The lack of any detectable PAH emission also shows

that star formation is weak in the circumnuclear region. Assuming that the luminosity in

NGC 4151 is anisotropic (~ 13 times), the extended mid-IR emission in NGC 4151 is

consistent with thermal re-radiation from dust grains in the NLR heated by a central

engine. An upper limit on the size of the torus in the mid-IR of $\lesssim 35$pc is measured,

consistent with the measurements of N90, and Ruiz et. al. (2002). This results in an upper

limit to the mid-IR contribution from a dusty torus in NGC 4151 of $\gtrsim 73\%$ of the total

emission at 10.8 µm and 18.2 µm based on our unresolved (PSF) component. Mid-IR

measurements of the proposed torus by N90 as well as upper limits derived from this

paper are roughly consistent with the "onion-skin" model of Pedlar et al. (1998).

CHAPTER 5
CASE STUDY: CYGNUS A

Cygnus A is the most powerful extragalactic radio source in the local universe (located at a distance of 224 Mpc, $H_0 = 75$ km s^{-1} Mpc^{-1}) and was among the first extra-galactic radio sources to be optically identified (Baade & Minkowski 1954). However, the true nature of the central engine has remained controversial since that time. Cygnus A is the prototypical FR II radio galaxy containing a powerful radio jet extending approximately 80 kpc on either side of the nucleus. In addition, the nuclear region of Cygnus A may contain a heavily extinguished quasar, hidden from direct view by up to A V =170±30 magnitudes of extinction as determined by x-ray observations of Ueno et al. (1994).

Key evidence for the embedded quasar model of Cygnus A was provided through the detection of broad emission lines by Antonucci, Hurt, and Kinney (1994) and Ogle et al. (1997). Additionally, x-ray spectra taken by Ueno et al. (1994) suggest the presence of an obscured power-law source, entirely consistent with that expected of a quasar. Further evidence for a central AGN is provided by the detection of a bi-conical ionization structure in the inner 3", observed at optical and near-IR wavelengths by Jackson, Tadhunter, and Sparks (1998) and Tadhunter et al. (1999) respectively using the HST. The cone axis is aligned to within 15° of the radio axis and, in the near-IR, resembles an edge-brightened bipolar structure typically observed around young stellar objects (see Velusamy & Langer 1998).

The detection of an ionization cone and broad emission lines near the nucleus of Cygnus A provides general support for the so-called "unification theories of AGN" (i.e.

Antonucci & Miller, 1985). These models account for the dichotomy in active galaxies in which broad and narrow emission lines are observed in Type 1 AGN whilst Type 2 AGN display only narrow emission lines. Unified theories presume that an optically and geometrically thick dusty torus surrounds the central engine, obscuring the broad emission line region (BLR) from some lines of sight. The narrow emission line region (NLR) typically extends over a large volume and hence is less affected by the line of sight to the central engine. When the torus is viewed face on, the BLR and NLR from the central engine can be observed. When the torus is viewed edge on, the BLR is obscured and only narrow emission lines are detected. By observing Type 2 sources at emission line wavelengths (such as [OIII], Hα and [NII]), ionization structures have been detected in several sources (i.e. Schmitt & Kinney, 1996; Falcke et al., 1998). In many cases the structures are conical or bi-conical, consistent with ionization by a central source collimated by a surrounding torus. The detection of an ionization cone at optical wavelengths along with detection of broad emission lines lend support to the idea that the active core of Cygnus A is obscured from direct view by a torus.

This chapter presents subarcsecond resolution 10 and 18 μm images of the central ~ 8 kpc of Cygnus A. These images show evidence of the bi-conical structures seen in near-IR observations with HST (Tadhunter et al. 1999). This chapter discusses observations and results as well as the origin of the mid-infrared emission on nuclear (sub-kpc) and large (1.5-2 kpc) scales.

Observations

Observations of Cygnus A were made on May 9, 1998 using the University of Florida mid-infrared camera/spectrometer OSCIR on the Keck II 10-m telescope. OSCIR uses a 128 x 128 Si:As Blocked Impurity Band detector developed by Boeing. On the Keck II

10-m telescope OSCIR has a plate scale of 0.062" pixel^{-1} with the f/40 chopping secondary, corresponding to a field of view of 7.9" x 7.9". Images were obtained in the N (λ_0 = 10.8 µm, $\Delta\lambda$ = 5.2 µm) and IHW18 (λ_0 = 18.2 µm, $\Delta\lambda$ = 1.7 µm) filters using a standard chop/nod technique to remove sky background and thermal emission from the telescope. The chopper throw was 8" in declination at a frequency of 4 Hz and the telescope was beam switched every 30 seconds. All observations were guided using the off-axis guider. OSCIR was mounted at one of the Keck-II "bent cassegrain" ports. Due to the alt-az mount of the Keck-II telescope, any instrument directly attached to it will see a fixed pupil and a field orientation which rotates as the telescope tracks. In order to fix the field as seen by the detector array, OSCIR was mounted on an instrument counter-rotator. However, this does produce a rotation of the pupil as the telescope tracks, and correspondingly a rotation of the Keck hexagonal diffraction pattern on the detector array.

Cygnus A was observed for a total on-source integration time of 240 seconds (480 chopped) at N and 180 seconds (360 chopped) at IHW18. Observations of γ Aql were taken directly before Cygnus A for flux calibration. Absolute calibration of γ Aql was achieved using a stellar model based on spectral irradiance models of similar K3II stars by Cohen (1995) adjusted for filter and atmospheric transmission. Measurements of other calibration stars throughout the night showed flux calibration variations of less than 5% at N and less than 15% at IHW18. Observations of ν Cyg and γ Aql were used to measure the telescope's point spread function (PSF). The measured FWHM of ν Cyg at N was 0.30" based on a 15 second exposure (30 seconds chopped). Images of ν Cyg were not obtained at IHW18 so the flux calibration star γ Aql was used as a measure of the IHW18

PSF. This yielded a FWHM of 0.4" based on a 30 second exposure (60 seconds chopped). Both measurements lie close to the theoretical diffraction limit (0.27" at N and 0.38" at IHW18). Short integrations on ν Cyg and γ Aql were sufficient for comparison to Cygnus A due to the stability of the OSCIR/KECK II PSF on May 9, 1998. Observations of the standard star β Leo taken in 15 second increments showed that the FWHM varied by < 7% over a total integration time of 180 seconds (360 chopped).

Cygnus A images were rotated to place North up and East left in post-processing. Images of the PSF stars ν Cyg and γ Aql were also rotated -14.1° and 37.8° respectively to match the position angle of the Keck hexagonal diffraction pattern as projected on the detector array when Cygnus A was observed. In addition, PSF images were rotationally "smeared" to account for the slight rotation of the pupil ($\lesssim 3°$) during the exposure times of Cygnus A.

Results

Figure 5-1 shows our N band image of the central 2 kpc (~ 2") of Cygnus A. Figure 5-2 shows the same analysis of Cygnus A at IHW18. Both figures clearly show extended emission detected primarily to the east of the nucleus. This extended emission can be separated into two distinct regions located northeast and southeast of the central source. These regions are closely aligned with the bi-conical structure (opening angle ~116°) observed at optical wavelengths by Jackson, Tadhunter, and Sparks (1998) and at near-IR wavelengths by Tadhunter et al. (1999). In addition, the data shows that most of the 10 μm emission arises from the SE-NW limb of the bi-cone. This is similar to the results of Tadhunter et al. (2000) in which the SE-NW limb also dominates in near-IR polarization images.
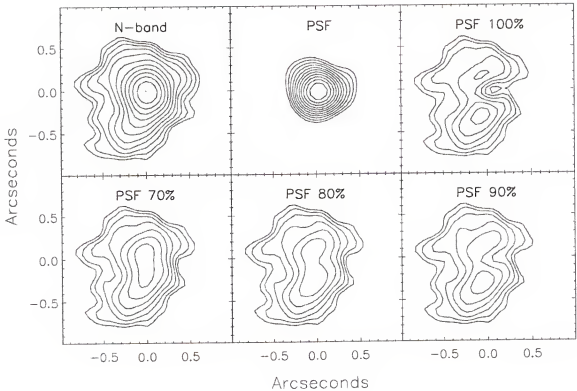
Figure 5-1. N-band images of the central 2" of Cygnus A showed with North up and East left. All images are smoothed with a 0.18" gaussian filter to enhance low level emission and scaled logarithmically. The lowest contour represent the 4 σ level of the smoothed data (0.067 mJy). The next image shows the PSF star v Cyg scaled to the same level as Cygnus A for comparison. The next four images shows the residuals of Cygnus A after subtraction of the PSF (unresolved component) scaled to 100, 70, 80, and 90% of the peak height. With the peak scaled to the same height as Cygnus A (100%), the unresolved component represents 40% of the total emission detected at 10 μm.

Table 5-1 shows our flux measurements of Cygnus A in comparison with other observation from the literature. These values are also plotted in Figure 3. Comparing our results with that of IRAS shows that while ~ 100% of the predicted 10 μm flux is observed, only 60% of the predicted 18μm flux is seen (based on a simple linear fit). This implies that most of the warm dust (< 12 μm) lies within the central 2" region of the galaxy while the cooler dust (> 18 μm) extends farther out. These results are roughly consistent with the 20 μm ISO data of Haas et al. (1998) which measured 816 mJy using
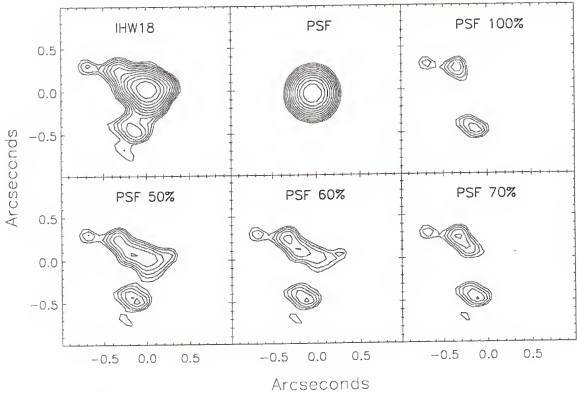
Figure 5-2. IHW18 (18 μm) images of the central 2" of Cygnus A showed with North up and East left. All images are smoothed with a 0.18" gaussian filter to enhance low level emission and are scaled logarithmically. The lowest contour represents the 3 σ level of the smoothed data (0.51 mJy). The next image shows the PSF star γ Aql scaled to the same level as Cygnus A for comparison. The next four images show the residuals of Cygnus A after subtraction of the PSF (unresolved component) scaled to 100, 50, 60, and 70% of the peak height. With the peak scaled to the same height as Cygnus A (100%), the unresolved component represents 60% of the total emission detected at 18 μm.

a 23" aperture but does not explain their 12.8 μm measurement of 485 mJy. It is unclear

why the 12.8 μm ISO data differs so greatly from the IRAS data taken in a larger aperture

as well as other 10 μm measurements from the literature.

In addition to the sub-kpc structure of Cygnus A, large scale mid-IR emission > 1.5

kpc from the nucleus is detected within the ionization cone. Flux is detected within both

cones at N, while low level emission at IHW18 is detected only in the southeastern cone.

This large-scale emission can be seen at a 2-3 sigma level in 0.5" gaussian smoothed 10

Table 5-1. Cygnus A Flux Density Measurements

Filter	Aperture (arcsec)	Flux Density (mJy)	Reference
N band	2	104 ± 3[a]	1
N band	2 x 4[b]	126 ± 4[a]	1
N band	5.8	180 ± 30	2
10 µm	6	180 ± 30	3
11.7 µm	1.92	122	4
12 µm (IRAS)	30 x 90	168 ± 18	5
12 µm (ISO)	23	485	6
Long Wavelength			
IHW18 (18 µm)	2	319 ± 27[a]	1
IHW18 (18 µm)	2 x 4[b]	409 ± 38[a]	1
25 µm (IRAS)	30 x 90	912 ± 16	5
25 µm (ISO)	23	816	6

[a] Error bars include statistical as well as calibration error (~ 5% at N band and ~ 15% at IHW18.
[b] Measured using a rectangular beam with major-axis position angle ~ 60° to incorporate large-scale emission.
REFERENCES. (1) This paper, also Radomski et al. 2001; (2) Heckman et al. 1983; (3) Rieke and Low 1972; (4) Whysong and Antonucci 2001; (5) Knapp, Bies, and van Gorkom 1990; (6) Haas et al. 1998.

µm and 18 µm images in Figure 5-4. Figure 5-5 shows the large-scale N-band emission to be approximately coincident with [OIII] emission located within the ionization cone of Cygnus A. Measurements of this emission were taken with 2" x 4" rectangular beam (see Table 1). Subtracting off the 2" flux measurement of the core leaves us with ~ 22 ± 2 mJy at N and ~ 90 ± 10 mJy at IHW18 over a ~ 5 arcsec^2 region.
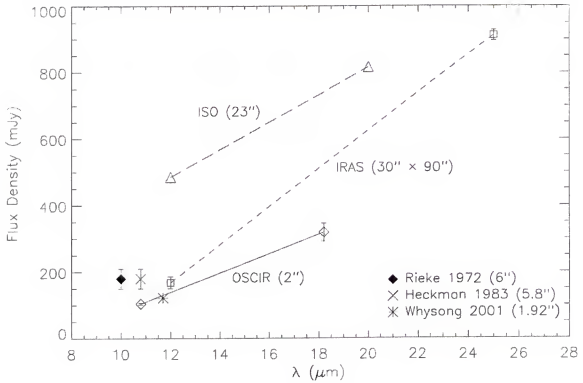
Figure 5-3. Flux measurements as seen in Table 5-1 labeled with the corresponding instrument (or reference) followed by the aperture used in parenthesis.
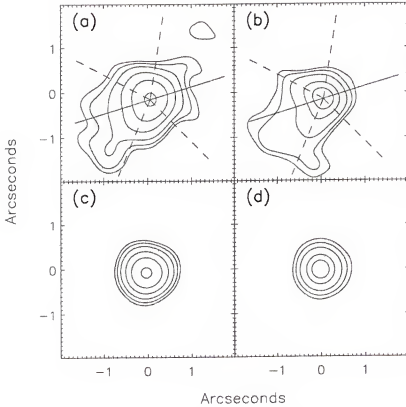
Figure 5-4. Contours of the large-scale emission marginally detected at 10 and 18 μm respectively, smoothed by a gaussian filter of width ~ 0.5" to enhance low level emission. Image (a) shows the 10 μm emission with the lowest contours representing the 2 σ level. Subsequent contours are at 3, 5, 10, 20, and 40 σ. Image (b) shows the 18 μm emission with the lowest contours also representing the 2 σ level. Subsequent contours are at 3, 5, 10, and 15 σ. The radio axis (solid line) and linear ionization cone structure (dashed lines) is overlaid for reference. Image (c) shows the 10 μm PSF star ν Cyg scaled the same as (a) for comparison. Likewise image (d) shows the 18 μm PSF star γ Aql scaled the same as (b) for comparison.
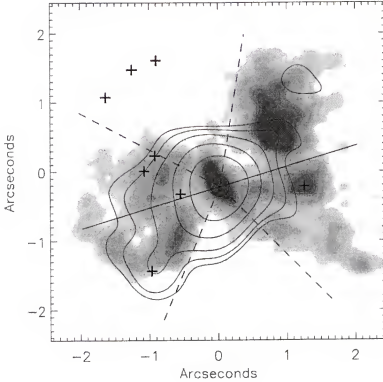
Figure 5-5. Contours of the large-scale emission marginally detected at 10 μm overlaid on the grayscale [OIII] map of Jackson et al. (1998). The 10 μm image is heavily smoothed by a gaussian of width ~ 0.5" to enhance low level emission and centered on the radio core. The lowest contour represents the 2 σ level, with subsequent contours at 3, 5, 10, 20, and 40 σ. Crosses indicate the position of blue compact condensations from Jackson et al. (1998) which possibly represent areas of star formation.

Temperature and Optical Depth

Temperature and emission optical depth maps from simple radiative transfer analysis

provide a good first-order estimate of the sources of grain heating as well as the relative

density of warm grains (Tresch-Fienberg et al. 1987). Flux maps of the nuclear region of

Cygnus A were created by convolving images at N with the IHW18 PSF and vice-versa

to attain the same resolution. Temperature and emission optical depth estimates were

obtained pixel by pixel by solving the equation of radiative transfer ($F_v = \Omega \tau B_v(T)$) at

two wavelengths assuming the optically thin approximation ($\tau \ll 1$), where F_v is the
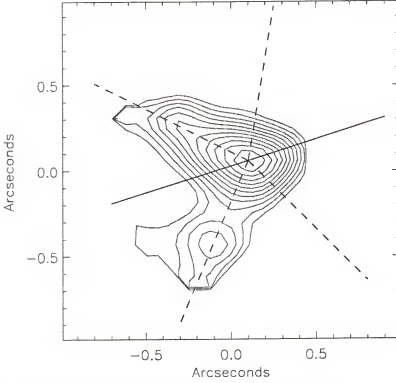
Figure 5-6. Emission optical depth map created from the ratio of 10/18 μm emission. Contours are scaled linearly with the lowest contour at 1.0 x 10^4 and the maximum at 5.9 x 10^4 . The radio axis (solid line) and linear ionization cone structure (dashed lines) derived from the 2.0 μm emission is overlaid for reference.

observed flux density at frequency v, Ω is the solid angle of each pixel, $B_v(T)$ is the

Planck function evaluated at frequency v and temperature T, and τ is the emission optical

depth. The frequency dependence of dust grain emission efficiency in the mid-IR is

approximated as $Q(v) \sim v^1$. Since no astrometric calibration was performed due to the

limited field of view of OSCIR, the peak flux of the convolved N-band image was

aligned to coincide with peak flux of the convolved IHW18 image. In order to determine

the errors due to alignment, a Monte Carlo simulation was done by shifting the two

convolved images with respect to each other up to ~ 0.1" in all directions. The structure

of the temperature map was highly dependent on the alignment of the two convolved

images. Temperature values were most stable within the SE cone, varying ±5 K.

Temperatures in the core showed a dispersion of approximately ±10 K, while that in the

NE cone varied up to ±30 K due to low S/N of any extended emission at 18 μm in this

area. The emission optical depth map (Figure 5-6) was much less dependent on alignment

and consistently showed higher optical depths along the limbs of the SE ionization cone.

This is consistent with the scenario proposed by Tadhunter et al. (1999) that dust has

been destroyed or swept out of the cones by outflows from the central quasar. Lateral

expansion of these outflows may have also caused density enhancements of dust along

the walls of the bi-cone.

Analysis and Discussion

There are several possible mechanisms that can account for extended mid-IR

emission: in-situ star formation, material heated by shocks, dust heated by the central

engine, polycyclic aromatic hydrocarbon emission (PAH), and emission lines. Each is

considered below and how they relate to the mid-infrared emission detected on small

(sub-kpc) and large scales (1.5-2 kpc).

Origin of Sub Kiloparsec Emission

The next two sections discusses two possible sources of the mid-IR emission in

Cygnus A detected on sub-kpc scales. These are star formation and heating from the

central engine.

Star formation

Extended mid-IR emission has been observed to arise from young star formation in the

central regions of galaxies (Telesco 1988). In Cygnus A however, estimates of the 2-10

keV hard x-ray luminosity relative to the 40-500 μm far-IR luminosity is ≥ 0.1, typical

for a galaxy predominantly powered by AGN activity (Imanishi et al. 2000). Additionally

the 11.3 μm PAH emission is less than would be expected if the region contains strong

star formation. PAH measurements of Imanishi and Ueno (2000) place a lower limit of the ratio of 11.3 µm luminosity to far-IR luminosity more than an order of magnitude smaller than that found for galaxies dominated by star formation (Smith, Aitken, & Roche 1989). Finally, optical spectroscopy of Cygnus A by Thornton, Stockton, and Ridgway (1999) (using a 1.1" slit oriented along the ionization cone axis) show the equivalent width of the Ca II triplet $\lambda 8498$, $\lambda 8542$, $\lambda 8662$ to be much less than would be expected if star formation dominated the nucleus (Terlevich, Diaz, & Terlevich 1990). Thus it is unlikely that the majority of the mid-IR emission detected arises from star formation.

Heating from central engine

Optical spectroscopy by Thornton, Stockton, and Ridgway (1999) also detected [Ar XI] $\lambda 6917$ and [Fe XI] $\lambda 7889$ in the southeastern component of Cygnus A. High-ionization lines such as these indicate either photoionization by a continuum source extending to the far-UV or transient heating by high speed shocks to $\sim 2 \times 10^6$ K (e.g. Osterbrock & Fulbright 1996). Thornton used the line flux ratios of H_2 (F[v = 1-0 S(3)]/F[v = 1-0 S(1)], Kawara, Nishida & Gregory 1990) as well as the ratio of H_2 and [O I] emitting regions (Mouri et al. 1989) to rule out shock heating and propose that the most likely cause for the high-ionization lines was due to x-ray heating from a central quasar. The central quasar may also be responsible for the extended mid-IR emission. Based on color temperature maps of the nuclear region (see section 3.1), dust is estimated to reach a T ~ 150±10 K up to 500 pc from the central source. Assuming a uniform dust distribution, a first-order determination of the size of the region that could be heated by a central source can be made. A rough estimate of the temperature of dust in a strong UV field (Dopita et al. 1998) is given by

$$T = 900 \cdot L_{10}{}^{0.22} \cdot r_{pc}{}^{-0.44} \cdot a^{-0.22}$$

where L_{10} is the luminosity of the central source is units of 10^{10} $L_\odot$, r_{pc} is the radius from the source in parsecs, and a is the average grain radius in units of 0.1 μm. Estimating the true luminosity of an embedded source such as Cygnus A is difficult due to the high levels of dust obscuration towards the central source. Haas et al. (1998) estimated a luminosity $L_{1-1000\mu m} = 4.7 \times 10^{11}$ $L_\odot$ for Cyg A from ISO measurements. Ward et al. (1991) however, estimated the total luminosity of Cyg A to be as high as $\sim 1.6 \times 10^{12}$ $L_\odot$. Using Balmer line fluxes in a 5" aperture, Stockton, Ridgway, and Lilly (1994) calculated a bolometric luminosity of Cyg A of $L_{Bol} = 3.3 \times 10^{11}$ $L_\odot$. However, they also noted that this calculation assumed that the gas in the central region had a covering factor of unity and hence represents a lower limit that could easily be an underestimate of the true luminosity by a factor of 10 or more. Therefore the true luminosity of Cygnus A could be as high as 3.3×10^{12} $L_\odot$. Using equation (1) and assuming a central luminosity of $\sim 1 \times 10^{12}$ $L_\odot$, dust could be heated to a temperature of 150 K from the central engine up to a distance of ~ 500 pc for grain sizes ~ 0.1 μm. Classical interstellar dust is generally considered to be a mixture of silicate and graphite particles with grain sizes in the range (0.003 - 1 μm) (Draine & Lee 1984). Thus the sub-kpc extended mid-IR emission in Cyg A is consistent with heating of dust from a central engine.

Origin of Large Scale Emission

Although dust heated from the central engine may account for the mid-IR emission on sub-kpc scales, it may not entirely account for the low level large-scale emission marginally detected at 10 and 18 μm (see Figure 5-4). This large scale emission extends 1.5 - 2 kpc from the nucleus and covers a total area of ~ 5 arcsec^2. Based on the average

surface brightness of this emission in the SE cone a dust T~150±5 K is estimated (similar to that found in the nuclear regions). Referring back to equation (1), in order for dust grains at ~1.5 kpc to reach these temperatures from central heating they would need to be ~ 0.02 µm. In the NE cone where only 10 µm emission is detected, a lower temperature limit of approximately 220±30 K is estimated which would require dust grains ~ 0.003 µm. Though these are only approximations of course, they do imply that central heating may not be able to entirely explain mid-IR emission on these large scales. This raises the possibility that small grains such as PAH's could contribute to the large scale emission. Previous spectrometry by Imanishi and Ueno (2000) reveals that the 11.3 µm PAH feature is weak in Cygnus A. This measurement was made with a 0.5" slit centered on the nucleus of the galaxy. However, the orientation of the slit with respect to this large scale extended emission is unclear. If the slit was oriented perpendicular to this emission it may have only shown that PAH emission is weak in the core of Cygnus A and may not necessarily rule out PAH emission farther out in the ionization cone. In-situ heating from ongoing star formation may also contribute to the large-scale emission. Though mid-IR emission from star formation is probably weak in the central few kpc of Cygnus A, it may explain the low level emission marginally detected in the SE cone at N and IHW18. Jackson, Tadhunter, and Sparks (1998) detected several compact blue regions within the inner ~2 kpc of Cygnus A using HST filters between 336- 622nm. At least 4 of 8 of these regions coincide with the large-scale extended emission seen at N and IHW18 in the SE cone (see Figure 5). Lynds et al. (1994), Stockton, Ridgway, and Lilly (1994), and Jackson all suggest that these regions trace young star formation similar to young star clusters seen in NGC 1275 (Holtzman et al. 1992). Another possible explanation for the

large-scale extended emission is mid-IR line emission. The coincidence between the [OIII] and this emission reveal that ionizing photons of at least 54.9 eV exist in these regions. This provides sufficient ionization to produce the 12.814 µm [NeII] fine structure line (21.6 eV) which would fall within our N-band filter (~ 8-13 µm). Other mid-IR lines such as [ArIII] and [SIV] could also contaminate our N-band filter and contribute to this emission. Future mid-IR spectroscopy with the slit placed along the ionization cone is needed to explore this possibility.

Conclusions

The mid-IR morphology of the inner kpc of Cygnus A shows structure consistent with the bi-cone observed at near-IR wavelengths. Calculations suggest that these structures are consistent with heating from a central engine rather than from local heating from star formation. Low level extended emission is also detected at 10 and 18 µm on scales up to 1.5-2 kpc from the nucleus. This emission may be a result of heating from the central engine on small grains, in-situ heating from weak star formation, line emission such as from [Ne II], PAH emission or any combination of these. An optical depth map of the region shows the highest optical depth is located along the edges of the ionization cone and supports the conclusion that dust in the central regions of Cygnus A is swept up by outflows, possibly causing density enhancements along the walls of the bicone.

CHAPTER 6
CASE STUDY: MRK 231

The galaxy Mrk 231 is one of the most luminous objects in the local universe ($z \leq$ 0.1), with an infrared luminosity of L_{IR} (8-1000µm) = 3.0 x 10^{12} $L_{\odot}$ (Genzel et al. 1998). The extreme IR luminosity is primarily due to either heating of dust by an AGN, intense star formation, or a mixture of both processes. AGN activity is confirmed by the detection of strong broad emission lines characteristic of a Seyfert 1 (Boksenberg et al. 1977). Radio observations of Neff and Ulvestad (1988), and Ulvestad, Wrobel, and Carilli (1999) also provide evidence for an AGN. These observations show a compact core less than 0.002" (1.6 pc) with a brightness temperature (10^9 -10^{10} K) most likely due to a central engine rather than supernovae remnants. In addition, Matthews et al. (1987), Keto et al. (1992), and Miles et al. (1996) reveal a compact 10 µm core suggestive of an AGN at the center of Mrk 231 ≤ 0.6" (492 pc) across.

Although Mrk 231 certainly contains an active nucleus, there is evidence that at least some, if not most, of the IR luminosity may be due to a circumnuclear starburst. Observations by Krabbe et al. (1997) of near-IR H_2 emission lines show a region of warm molecular gas on a scale of 3" (2.5 kpc). This overlaps with CO emission detected by Bryant and Scoville (1996), and Downes and Solomon (1998) which show a disk of emission aligned east-west with an inner diameter of 1" (820 pc) surrounded by a lower density region extending up to 3". Carilli, Wrobel and Ulvestad (1998) also detect continuum radio continuum emission with a major axis of 0.44" (360 pc) oriented east-west at an inclination to our line-of-sight of ~ 45°. In addition, they find HI 21cm

absorption in a disk elongated east-west with a velocity of $\pm$ 110 km s^{-1} out to a radius of 0.1" (82 pc). They identify this HI and radio continuum disk as the inner part of the molecular disk seen a larger scale and argue that the physical conditions for the thermal and nonthermal gas in this disk are similar to those proposed for compact nuclear starburst galaxies. Smith et al. (1998) also detects OH maser emission coincident with this emission over an angular dimension of 0.10" x 0.05" (82 x 41 pc) which they attribute to massive star formation in the inner disk.

This chapter discusses 10 and 20 μm observations obtained from the Keck II 10 m telescope of the core of Mrk 231. Mid-IR wavelengths act to trace the warm dust associated with star formation as well as AGN activity. Spatially extended infrared emission implies starburst activity while compact emission ($\ll$ kpc) is indicative of either a very dense starburst or an AGN (Miles et al. 1996). Observations in this chapter at high resolution will attempt to discern between a compact starburst or AGN.

Observations and Data Reduction

Observations of Mrk 231 were made in May 1999 using the University of Florida mid-IR camera/spectrometer OSCIR on the Keck II 10 m telescope. On the Keck II 10 m telescope OSCIR has a plate scale of 0.0616" pixel^{-1} corresponding to a field of view of 7.9" x 7.9". Images were obtained at N (λ_o = 10.8 μm, $\Delta\lambda$ = 5.2 μm) and IHW18 (λ_o = 18.2 μm, $\Delta\lambda$ = 1.7 μm) using the standard chop/nod technique to remove sky background and thermal emission from the telescope. The chopper throw was 10" in declination at a frequency of 4 Hz and the telescope was nodded every 30 seconds.

Mrk 231 was observed on May 6, 1999 for a total on-source integration time of 4 minutes per filter. Observations of Mrk 231 were preceded and followed by observations

of PSF stars PPM 50530 and α Crb. In addition, α Crb was used as a flux calibrator. Absolute photometric calibration of α Crb was performed using observations at N and Q by Tokunaga (1984). Flux calibration at IHW18 was achieved by applying a filter correction based on stellar models of similar stars by Cohen (1995) adjusted for the OSCIR filter transmission and atmospheric transmission. Based on this information the flux for α Crb was calculated to be 5.03 Jy at IHW18 and 2.02 Jy at N.

Full width at half max (FWHM) measurements were made on both PSF stars and Mrk 231. The FWHM of the PSF star PPM 50530 at N (0.248") taken before the observation of Mrk 231 was much smaller than that of α Crb (0.292"). These two observations were separated by approximately 1.5 hours. Either due to telescope aberrations and/or sky conditions, the FWHM increased through the night. Thus to determine the FWHM at the time of the Mrk 231 observations, a simple line fit to the measurements before and after Mrk 231 was to estimate the FWHM at the time of the galaxy exposure (~ 0.266"). A similar procedure was not attempted at IHW18 as the second PSF did not have adequate S/N to measure the FWHM. Instead only the FWHM of the first PSF was used for comparison.

The FWHM size of Mrk 231 and the PSF was further modified to account for a color effect in the wide N-band filter (8-13 μm). This effect causes the diffraction limit of a star whose photosphere is at a high temperature (~ 4000 K) to be smaller than that of a region of dust at a lower temperature (~ 200 K). This is due to the peak flux of the dust being biased towards the longer wavelengths at N while the peak flux of the star is biased towards the shorter wavelengths of the N-band. The monochromatic resolution limit of a PSF taken at the central wavelength of the N-band (10.8 μm) at the 10 m Keck II is

~0.223" assuming the Sparrow criteria of ~ λ/D. The diffraction limit of a star at ~ 4000 K is 0.204", while the diffraction limit of an object at ~ 200 K is 0.227". At IHW18 the effect is minimal however, due to the shorter bandwidth and peak fluxes being distributed more equally throughout the IHW18 wavelength range.

Results

The results from analysis of Mrk 231 are discussed below. The first section begins with an analysis of the size of the mid-IR nucleus followed by a discussion on the source of the mid-IR emission. Figure 6-1 shows our mid-IR images of Mrk 231 and the PSF star α Crb.

Nuclear Size

The mid-IR size of the central core of Mrk 231 was determined by using three methodologies. First the FWHM of the galaxy and that of the PSF were subtracted in quadrature to determine an upper limit to the size of any extended region. At IHW18, the only PSF measurement of the FWHM was 0.399". This closely matched the size of Mrk 231 (0.395"± 0.010[5]) implying an unresolved core at these wavelengths. The PSF FWHM at N interpolated to the time of the galaxy exposure was 0.266". As discussed above the FWHM at N of a point source at ~ 4000 K is 0.204". Subtracting these in quadrature results in an extension possibly due to seeing of 0.170". A PSF model was created by applying this extension to the diffraction limiting size of a ~ 200 K point source (0.227"). Thus taking into account this extension and color effects, a point source

---

[5] Uncertainties were calculated based on the variation of the FWHM measured in 30 second intervals (one nod) over the total on-source integration of 4 minutes. This resulted in 8 measurements per filter of the PSF over a period ~16 minutes in real time due to the efficiency of the chop-nod process. No uncertainties were calculated for PSF stars due to their integrations consisting of only one 30 second nod per star.
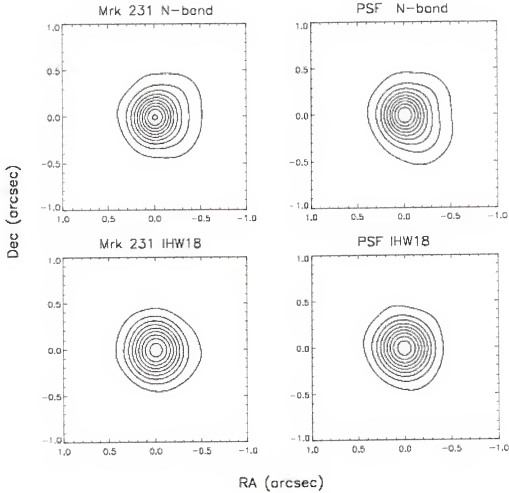
Figure 6-1. N-band (10.8 μm) and IHW18 (18.2 μm) images of Mrk 231. All images are smoothed with a 0.12" Gaussian to enhance low level emission. The lowest contours represent the 3σ level of the smoothed data (1.35 mJy at N, 2.00 mJy at IHW18). Contours are scaled linearly with a difference of 24.3 mJy per contour at N and 8.2 mJy per contour at IHW18.

at ~200 K should have a size of 0.284" at N. The observed size of Mrk 231 was

0.296"±0.003. Subtracted in quadrature this yields a size of 0.083"±0.011" (70 pc) for the

emitting region in the N-band. If the individual PSF FWHM for PPM 50530 (0.248") and

α Crb (0.292") are used rather than an interpolated value set to the time of the galaxy

exposure, the size of the emitting region ranges from as large as 0.130"±0.007" to unresolved.

The second method the size of the nucleus was measured involved fitting a blackbody to the observed fluxes at N and IHW18. This can be calculated from the standard solution of the radiative transfer equation at two frequencies (see Chapter 3).

$$F_{v1} = \Omega \cdot \left(1 - e^{-\tau_{v1}}\right) \cdot B_{v1}(T) \cdot e^{-\tau_{v1.ism}}$$

$$F_{v2} = \Omega \cdot \left(1 - e^{-\tau_{v2}}\right) \cdot B_{v2}(T) \cdot e^{-\tau_{v2.ism}}$$

The color-corrected monochromatic flux in a 2" diameter aperture around the center of Mrk 231 was measured to be 1.33±0.08 Jy at 10.8 μm (N) and 5.01±0.38 Jy at 18.2 μm (IHW18). This leaves us with four unknown parameters; the solid angle or size of the emitting region, Ω, the temperature of the region, T, the emission optical depth of the region τ_v, and the intervening intergalactic optical depth $\tau_{v.ism}$. Assuming the intervening intergalactic obscuration is small, and using the optically thick limit of $\tau_v \gg 1$, the above equations reduce to

$$F_{v1} = \Omega \cdot B_{v1}(T)$$

$$F_{v2} = \Omega \cdot B_{v2}(T)$$

Thus with two equations and two unknowns one can iterate and solve for Ω and T. Assuming the emission is isotropic this yields a lower limit to the size of an emitting blackbody and an upper limit to its color temperature. Based on the observed mid-IR flux densities associated with Mrk 231 a minimum size of the emitting region of ~ 0.05"

(41pc) and a maximum mid-IR color temperature of 194 K is calculated. In the other extreme, the optically thin limit where $\tau \ll 1$, the equations of radiative transfer reduce to

$$F_{\nu 1} = \Omega \cdot \tau_{\nu 1} \cdot B_{\nu 1}(T)$$

$$F_{\nu 2} = \Omega \cdot \left(\tau_{\nu 1} \frac{\nu 1}{\nu 2} \right) \cdot B_{\nu 2}(T)$$

However in this regime one cannot iteratively solve for Ω and T individually. Due to the dependence of the size of the emitting region on its emission optical depth the values of Ω and τ cannot be separated, rather one can only solve for the value of $\Omega x \tau$ and T. This yields a lower limit to the color temperature of 166 K.

The third way the size of the mid-IR nucleus was calculated also involved solving the equations of radiative transfer. In this case, assuming little intergalactic extinction, one is left with three unknowns; Ω, τ, and T. Optical depth values of Roche, Aitken, and Whitmore (1983) based on measurements of the $\sim$10 μm silicate feature showed $1.2 < \tau_{9.7} < 1.6$. Assuming a temperature between our optically thin limit of 166° K and our optically thick limit of 194 K, source sizes of 0.100" and 0.087" are calculated with a variation of $\pm$0.002" depending on the temperature used. The lower limit of the source size 0.087" $\pm$0.002" found by assuming $\tau_{9.7} = 1.6$, is very close to our source size of 0.083"$\pm$0.011" calculated at N by subtracting the interpolated PSF in quadrature.

Thus using three different methods we calculate source sizes of the mid-IR emitting regions over a very narrow range. This range of 0.05" – 0.100" is a factor of ~5 to 10 times smaller than previous mid-IR size limits of Matthews et al. (1987), Keto et al. (1992), and Miles et al. (1996) which showed an unresolved 10 μm source of $\leq$ 0.6". Our
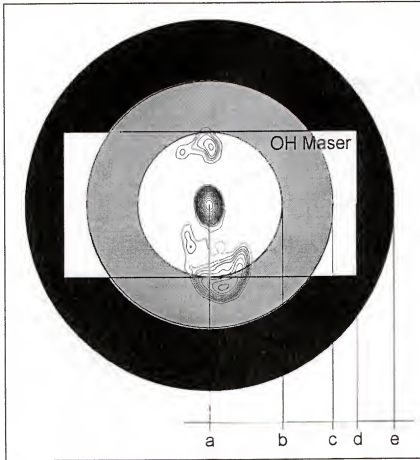
Figure 6-2. This figure shows the inner region of Mrk 231 to the same scale. (a) Center of the source based on 2.3 GHz radio contours of Ulvestad, Wrobel, & Carilli (1999). (b) The minimum size of the mid-IR region assuming the optically thick limit $\tau \gg 1$ (diameter = 0.05"). (c) The size measured from PSF subtraction (diameter = 0.085") as well as the approximate size of the mid-IR region assuming $\tau_{9.7\mu m} \sim 1.6$ (diameter = 0.087" ± 0.002"). (d) The size of the OH maser region (0.100" x 0.050") as well as the size of the mid-IR region assuming $\tau_{9.7\mu m} \sim 1.2$ (0.100"). (e) The 3σ upper limit to the mid-IR region from Soifer et al. (2000).

measurements also agree closely with the results of Soifer et al. (2000) which observed

Mrk 231 at 12.5 μm using the Long Wavelength Spectrograph (LWS) at Keck I. Using

nine measurements of their PSF interweaved with eleven measurements of Mrk 231, they

determined the source to be unresolved with a maximum size of 0.13" based on the 3σ

standard deviation of their FWHM measurements. Figure 6-2 shows the central region of Mrk 231 and the various size estimates of the mid-IR emitting region.

AGN vs. Starburst

The origin of the far-IR luminosity of Mrk 231 has been debated for some time. Cutri et al. (1984) modeled the near-IR spectrum as a linear combination of the spectra of M82 (starburst) and NGC 4151 (Seyfert 1.5) and concluded that the luminosity of Mrk 231 is divided equally between starburst and AGN activity. Downes and Solomon (1998) attributed as much as 2/3 of the luminosity to starburst activity in the central kpc. Star formation models of Smith et al. (1998) however disagree. Their data showed that the far-infrared (FIR) luminosity of Mrk 231 could not be realistically fitted by a starburst even accounting for a high star formation rate (SFR) and including radio super novae (RSN) at extremely high radio powers, as much as an order of magnitude larger than any previously reported RSN. Finally, mid-IR ISO spectroscopy by Genzel et al. (1998) also showed that as much as 90% of the luminosity of Mrk 231 is dominated by an AGN based on a strong high excitation mid-IR emission lines on the one hand, and a weak 7.7 μm PAH feature on the other hand.

A possible method to disentangle the emission processes is by measuring the luminosity density of the emitting region in the mid-IR as compared to typical starburst regions in other galaxies. Star forming regions of Luminous Infrared Galaxies (LIG's) typically have sizes up to several kpc and bolometric surface brightness's up to (1-5) x 10^5 L$_\odot$ pc^{-2} (Telesco 1988, Meurer et al. 1997). Super star clusters (SSC) such as those in NGC 1569 and NGC 1705 are thought to be a major component in producing the high L$_{IR}$ in these galaxies. For example, O'Connell, Gallagher, and Hunter (1994; hence OGH) measure the surface brightness of SSC NGC 1569A, NGC 1569B, and NGC 1705 and

found the average bolometric surface to be on order of $\sim 3 \times 10^6$ $L_\odot$ pc^{-2} (about 2 times that of the R136 cluster in 30 Doradus (Malumuth & Heap (1994)). Comparing this to the values for LIG's by Telesco (1988), they conclude that if SSC's are typical of these regions they must cover $\sim 10\%$ of the area of the star forming regions in these systems, a value they regard to be remarkably dense. In comparison Meurer et al. (1997) found that the peak surface brightness of clusters in some starburst galaxies can reach 5.0×10^7 $L_\odot$ pc^{-2} over regions < 10 pc in diameter.

Our measurements of Mrk 231 show a mid-IR luminosity (L_{MIR}) of 6.69×10^{11} $L_\odot$ within a radius of $\sim 0.085''$ (70 pc). This mid-IR luminosity represents a lower limit to the bolometric luminosity while the radius represents our upper limit to the size of the emitting region. Thus the minimum surface brightness we calculate is $\sim 1.8 \times 10^8$ $L_\odot$ pc^{-2}. These measurements however only represent a lower limit to the energy density. In the optically thick blackbody regime we calculate a minimum source size of $\sim 0.05''$ (41pc) resulting in a $L_{MIR} = 1.0 \times 10^{12}$ $L_\odot$. This would imply a maximum surface brightness of $\sim 7.6 \times 10^8$ $L_\odot$ pc^{-2}. These results agree closely with that of Soifer et al. (2000) who performed a similar analysis. As discussed earlier they found Mrk 231 to be unresolved with a maximum size of $< 0.13''$ (106 pc) based on their 3σ standard deviation of their FWHM measurements. They then calculated the maximum and minimum surface brightness of Mrk 231. Their maximum surface brightness assumed that the total infrared luminosity ($\sim L_{IR}$ (8-1000μm) $= 3.0 \times 10^{12}$ $L_\odot$) emerges from the compact core. Their minimum assumes that only their "observed" mid-IR luminosity emerges from the compact core. Their values as well as our calculations in addition to measurements of other star formation regions are listed in Table 6-1. These results show that the minimum

surface brightness of Mrk 231 is between $(1 - 1.8) \times 10^8$ $L_\odot$ pc^{-2}. This is ~ 30- 60 times

higher than the average surface brightness of SSC's as measured by OGH and at least 2-4

times brighter than the brightest starburst cluster as measured by Meurer et al. (1997)

over an area 100-300 times greater than the typical sizes of these clusters. These results

imply that the nuclear region of Mrk 231 is

dominated by a powerful AGN rather than a starburst. Starburst activity does occur in a

region ~ 3" (2.5 kpc) of the nucleus, however these star forming knots only contribute a

far-IR luminosity of ~ 2×10^{10} $L_\odot$ (Surace & Sanders 1999) which is < 1% of the IR

luminosity.

Table 6-1. Energy Density

Object	Size (pc)	$L_\odot$ pc^{-2}	Reference
Starburst Cluster	< 10	5.0×10^7	Meurer et al. (1997)
SSC NGC 1569 A	4.4	5.6×10^6	OGH
SSC NGC 1705	6.8	2.0×10^6	OGH
R136 (30 Doradus)	8.4	1.4×10^6	Malumuth and Heap (1994)
SSC NGC 1569 B	6.0	1.3×10^6	OGH
NGC 253	150	4.0×10^5	Telesco (1988)
M82	250	1.4×10^5	Telesco (1988)
Mrk 231			
Mrk 231 Max	41	7.6×10^8	This chapter
Mrk 231 Max	< 106	$> 3.9 \times 10^8$	Soifer et al. (2000)
Mrk 231 Min	70	1.8×10^8	This chapter
Mrk 231 Min	< 106	$> 1.0 \times 10^8$	Soifer et al. (2000)

Conclusions

This chapter presents high resolution mid-IR imaging and analysis of the nuclear region of Mrk 231. The size of the core of Mrk 231 is measured to be between 5-10 times smaller than the sizes of ~ 0.5" as measured by Miles et al. (1996) and Keto et al. (1992). The large infrared luminosity from this galaxy is most likely dominated by emission from a dust enshrouded AGN rather than from a circumnuclear starburst in agreement with the results of Soifer et al. (2000).

CHAPTER 7
CONCLUSIONS

In this chapter the general conclusions of this disseratation as well as the prospects of future research are discussed.

General Conclusions

Mid –IR observations from this dissertation have contributed to the understanding of the dynamics in the central regions of three AGN. All three AGN (NGC 4151, Cygnus A, and Mrk 231) were observed at high resolution (sub-arcsecond) using 8-10 m class telescopes. This resulted in observations of the central kpc of these AGN at resolutions of 35, 250, and 300 pc respectively ($H_o = 75$ km s^{-1} Mpc^{-1}). This high resolution was essential in order to observe the narrow emission line region (NLR) of AGN which typically extend on scales of 0.1-1 kpc (Dahari & DeRobertis 1988) as well as circumnuclear starbursts which typically occur on scales of a few hundred parsecs (Ohsuga et al. 1999; Heckman et al. 1997; Colina et al. 1997; and Gonzalez-Delgado et al. 1998).

Observations of all three AGN were conducted at N ($\lambda_0 = 10.8$ µm, $\Delta\lambda = 5.2$ µm) and IHW18 ($\lambda_0 = 18.2$ µm, $\Delta\lambda = 1.7$ µm) using the University of Florida mid-IR camera/spectrometer OSCIR. The mid-infrared was chosen as an ideal wavelength regime for investigating the central regions of AGN. The mid-IR (10-25 µm) suffers 25–75 times less extinction than optical wavelengths and 3-10 times less extinction than the near-IR. This is especially important when studying the embedded regions in galaxies where the extinction must be at least 10 magnitudes at optical wavelengths in order to

hide the broad emission line region (Malkan et al. 1998). Additionally, AGN and starburst emission peak at mid-IR wavelengths and hence provides the ideal wavelength at which to study these different emission mechanisms (Telesco 1993).

Extended mid-IR emission was detected at both N and IHW18 in two AGN (NGC 4151 and Cygnus A) and marginally at N in the case of Mrk 231. In the cases of NGC 4151 and Cygnus A, extended mid-IR emission was consistent with heating of dust grains from the central engine. In Mrk 231, the high mid-IR surface brightness of the central source in comparison with strong starburst regions in other galaxies also shows that the core is most likely powered by the central AGN. No relationship between star formation and AGN type was found as mid-IR emission associated with the central super massive black hole dominated over star formation in all cases. However because only three AGN type were observed, a Seyfert 1, Seyfert 1.5, and a Type 2 FR II, no statistical evidence for or against evolutionary scenarios was discovered.

Suggestions for Future Work

Observations and results from this dissertation represent a beginning in the study of AGN characteristics. A much larger survey of galaxies taken at high resolution is needed to confirm evolutionary predictions.. In the future a high resolution mid-IR imaging survey of the entire Seyfert sample from Maiolino and Rieke (1995) (hereafter MR95) extended RSA sample is preferable. Observations of all 91 galaxies in the sample will greatly increase Seyfert statistics and provide a more complete sample of nearby Seyfert AGN. As discussed in Chapter 2 the average distance of Sy's in this sample is ~ 30 Mpc as opposed to ~ 100 Mpc for the CfA and ~ 140 Mpc for the 12 Micron Sy samples. The relative proximity of this sample allows nuclear spectra to be less diluted by stellar light from the host galaxy. Thus biases against detecting low luminosity and edge on Sy's are

greatly reduced in this sample in comparison to the more distant CfA and 12 Micron samples. This also allows the MR95 sample to be observed at 3-5 times greater resolution than the CfA and 12 Micron samples.

In order to survey galaxies at high resolution, mid-IR observations of this sample would best be carried out using large 8 -10 m class telescopes. These telescopes provide the high angular resolution necessary to study the sub-kpc regions of the MR95 Seyfert galaxies at mid-IR wavelengths. Assuming a resolution of ~ 0.4" at N-band (10 um) on Gemini, all but 7 of the Seyferts from the MR95 sample can be resolved at < 160 pc with 80% < 100 pc of which half are resolvable at < 50 pc. Proposals to observe the Northern portion of the MR95 sample using the Gemini North facility mid-IR imager Michelle will be submitted in the future. Approximately 2/3 of the sample is observable from the Southern Hemisphere using Gemini South and the initial focus of any future project is to complete the observations of these Southern sources using the facility mid-IR imager T-ReCS.

This survey will provide valuable information on the energetics and classification of Seyferts nuclei. Detection of an increasing amount of sub-kpc nuclear starburst activity and/or NLR dust emission through the progression from Sy 1 to Sy 2 would provide strong evidence for an evolutionary connection of Seyfert galaxies. In addition, detection of starburst activity in the near nuclear regions of Sy 2 hosts would provide further support for a stellar origin of the BFC (Cid Fernadez & Terlevich 1995, Colina et al. 1997, and Gonzalez-Delgado et al. 1998). Increasing starburst luminosity versus Seyfert type on scales of a few hundred parsecs would also provide support the models of an obscuring wall proposed by Oshuga et al. (1999). This survey will also help separate

excess mid-IR emission not associated with the torus and place greater constraints on torus models. Non-detection of enhanced starburst activity or more extended emission in later type Seyfert hosts would force major revisions in several of the above theories.

LIST OF REFERENCES

Antonucci, R. 1993, ARA&A, 31, 473

Antonucci, R. R. J., Hurt, T., & Kinney, A. 1994, Nature, 371, 313

Antonucci, R. R. J. & Miller, J. S. 1985, ApJ, 297, 621

Armus, L., Heckman, T. M. & Miley, G. K. 1989, ApJ, 347, 727

Audouze & Israel, 1985, Cambridge Atlas of Astronomy, Cambridge University Press

Ayani, K. & Maehara, H. 1991, PASJ, 43, L1

Baade, W. & Minkowski, R. 1954, ApJ, 119, 206

Bothun, G. D. & Cornell, M. E. 1990, AJ, 99, 1004

Braatz, J. A., Wilson, A. S., Gezari, D. Y., Varosi, F., & Beichman, C. A. 1993, ApJ, 409, L5

Bryant, P. M. & Scoville, N. Z. 1996, ApJ, 457, 678

Cameron, M., Storey, J. W. V., Rotaciuc, V., Genzel, R., Verstraete, L., Drapatz, S., Sieben-morgen, R., & Lee, T. J. 1993, ApJ, 419, 136

Carilli, C. L., Wrobel, J. M., & Ulvestad, J. S. 1998, AJ, 115, 928

Carleton, N. P., Elvis, M., Fabbiano, G., Willner, S. P., Lawrence, A., & Ward, M. 1987, ApJ, 318, 595

Cassidy, I. & Raine, D. J. 1996, A&A, 310, 49

Cid Fernandez, R., & Terlevich, R. 1995, MNRAS, 272, 423

Clavel, J. et al. 1990, MNRAS, 246, 668

Cohen, M., Witteborn, F. C., Walker, R. G., Bregman, J. D. & Wooden, D. H. 1995, AJ, 110, 275

Colina, L., Vargas, M. L. G., Delgado, R. M. G., Mas-Hesse, J. M., Perez, E., Alberdi, A., & Krabbe, A. 1997, ApJL, 488, L71

Contini, M., Viegas, S. M., & Prieto, M. A. 2002, A&A, 386, 399

Curran, S. J. 2000, A&AS, 144, 271

Cutri, R. M., Rieke, G. H., & Lebofsky, M. J. 1984, ApJ, 287, 566

Dahari, O. & DeRobertis M. 1988, ApJS, 67, 249

Davis, M., Huchra, J. & Latham, D. 1983, IAU Symp. 104: Early Evolution of the Universe and its Present Structure, 104, 167

de Kool, M. & Begelman, M. C. 1989, Nature, 338, 484

de Vaucouleurs, G., de Vaucouleurs, A., Corwin, H.: Second Reference Catalogue of Bright Galaxies, Univ. Texas Press, Austin (1976) (RC2)

de Vaucouleurs, G., de Vaucouleurs, A, Corwin, H.G., Jr., Buta, R.J., Paturel, G., Fouqué, P.: Third Reference Catalogue of Bright Galaxies, Springer-Verlag, New York (1991) (RC3)

Delgado, A. J., Alfaro, E. J., & Cabrera-Cano, J. 1997, AJ, 113, 713

Dopita, M. A., Heisler, C., Lumsden, S., & Bailey, J. 1998, ApJ, 498, 570

Dopita, M. A., & Sutherland, R. S. 1995, ApJ, 455, 468

Dopita, M. A. & Sutherland, R. S. 1996, ApJS, 102, 161

Downes, D. & Solomon, P. M. 1998, ApJ, 507, 615

Draine, B. T. 1981, ApJ, 245, 880

Draine, B. T. & Lee, H. M. 1984, ApJ, 285, 89

Dultzin-Hacyan, D., Krongold, Y., Fuentes-Guridi, & Marziani P. 1999, ApJ, 513, L111

Edelson, R. A. 1987, ApJ, 313, 651

Edelson, R. A. & Malkan, M. A. 1986, ApJ, 308, 59

Edelson, R. A., Malkan, M. A., & Rieke, G. H. 1987, ApJ, 321, 233

Efstathiou, A. & Rowan-Robinson, M. 1995, MNRAS, 273, 649

Engargiola, G., Harper, D. A., Elvis, M., & Willner, S. P. 1988, ApJ, 332, L19

Evans, I. N., Tsvetanov, Z., Kriss, G. A., Ford, H. C., Caganoff, S., & Koratkar, A. P. 1993, ApJ, 417, 82

Fadda, D., Giuricin, G., Granato, G. L., & Vecchies, D. 1998, ApJ, 496, 117

Falcke, H. Wilson A. S. Simpson, C. 1998, ApJ, 502, 199

Fanaroff, B. L. & Riley, J. M. 1974, MNRAS, 167, 31P

Ferland, G.J., & Netzer, H. 1983, ApJ, 264, 105

Fernandez, B. R., Holloway, A. J., Meaburn, J., Pedlar, A., & Mundell, C. G. 1999, MNRAS, 305, 319

Filippenko, A. V. & Halpern, J. P. 1984, ApJ, 285, 458

Filippenko, A. V. & Sargent, W. L. W. 1985, ApJS, 57, 503

Fisher, R. S. 2001, Ph.D. thesis Univ. Florida

Fitch, W. S., Pacholczyk, A. G., & Weymann, R. J. 1967, ApJ, 150, L67

Genzel, R. et al. 1998, ApJ, 498, 579

Giuricin, G., Mardirossian, F., & Mezzetti, M. 1995, ApJ, 446, 550

Gonzalez-Delgado, R., Heckman, T.M., Leitherer, C., Meurer, G., Krolik, J., Wilson, A., Kinney, A., & Koratkar, A. 1998, ApJ, 505, 174

Gonzalez-Delgado, R. M., Perez, E., Diaz, A. I., Garcia-Vargas, M. L., Terlevich, E. & Vilchez, J. M. 1995, ApJ, 439, 604

Goodrich, R. W. 1989, ApJ, 340, 190

Goodrich, R.W. 1995, ApJ, 440, 141

Goodrich, R. W. & Miller, J. S. 1994, ApJ, 434, 82

Granato, G. L., Danese, L. & Franceschini, A. 1997, ApJ, 486, 147

Haas, M., Chini, R., Meisenheimer, K., Stickel, M., Lemke, D., Klaas, U. & Kreysa, E. 1998, ApJ, 503, L109

Hamilton, D. & Keel, W. C. 1987, ApJ, 321, 211

Heckman, T. M. 1980, A&A, 87, 152

Heckman, T. M., Armus, L. & Miley, G. K. 1987, AJ, 93, 276

Heckman, T.M., Blitz, L., Wilson, A. S., Armus, L., & Miley, G.K. 1989, ApJ, 342, 735

Heckman, T.M., Gonzalez-Delgado, R., Leitherer, C., Meurer, G., Krolik, J., Wilson, A., & Koratkar, A., Kinney, A. 1997, ApJ, 482, 114

Heckman, T. M., Lebofsky, M. J., Rieke, G. H., & van Breugel, W. 1983, ApJ, 272, 400

Holtzman, J. A. et al. 1992, AJ, 103, 691

Huchra, J. & Burg, R. 1992, ApJ, 393, 90

Huchra, J., Davis, M., Latham, D. & Tonry, J. 1983, ApJS, 52, 89

Huchra, J., & Sargent, W. L. W. 1973, ApJ, 186, 433

Imanishi, M., Terada, H., Goto, M., & Maihara, T. 1998, PASJ, 50, 399

Imanishi, M. & Ueno, S. 2000, ApJ, 535, 626

Jackson, N., Tadhunter, C. & Sparks, W. B. 1998, MNRAS, 301, 131

Jaffe, W., Ford, H. C., Ferrarese, L., van den Bosch, F. & O'Connell, R. W. 1993, Nature, 364, 213

Johnston, K. J., Elvis, M., Kjer, D., & Shen, B. S. P. 1982, ApJ, 262, 61

Kaiser, M. E. et al. 2000, ApJ, 528, 260

Kawara, K., Nishida, M. & Gregory, B. 1990, ApJ, 352, 433

Kay, L. E. 1994, ApJ, 430, 196

Kellermann, K. I., Sramek, R., Schmidt, M., Shaffer, D. B., & Green, R. 1989, AJ, 98, 1195

Keto, E., Ball, R., Arens, J., Jernigan, G., & Meixner, M. 1992, ApJL, 387, L17

Khachikian, E. Y. & Weedman, D. W. 1974, ApJ, 192, 581

Knapp, G. R., Bies, W. E., & van Gorkom, J. H. 1990, AJ, 99, 476

Koski, A. T. 1978, ApJ, 223, 56

Krabbe, A., Colina, L., Thatte, N., & Kroker, H. 1997, ApJ, 476, 98

Krolik, J. H. & Begelman, M. C. 1988, ApJ, 329, 702

Kukula, M. J., Pedlar, A., Baum, S. A. & O'Dea, C. P. 1995, MNRAS, 276, 1262

Laor, A. & Draine, B. T. 1993, ApJ, 402, 441

Larson, R. B. 1988, IAU Symp. 126: The Harlow-Shapley Symposium on Globular
    Cluster Systems in Galaxies, 126, 311

Lawrence, A. 1987, PASP, 99, 309

Lord, S.D. 1992, NASA Technical Memor. 103957

Lynds, R., O'Neil, E. J., Scowen, P. A., & Idt, M. O. W. C. 1994, American Astronomical
    Society Meeting, 184, 4905

Lyutyi, V. M. 1972, AZh, 49, 930

Maiolino, R., & Rieke, G.H., 1995, ApJ, 454, 95 (MR95)

Maiolino, R., Ruiz, M., Rieke, G. H., & Keller, L. D. 1995, ApJ, 446, 561

Maiolino, R., Ruiz, M., Rieke, G. H., & Padadopoulos, P. 1997, ApJ, 485, 552

Malkan, M.A., Gorijan, V., & Tam, R. 1998, ApJS, 117, 25

Malumuth, E. M. & Heap, S. R. 1994, AJ, 107, 1054

Martin, P. G., Thompson, I. B., Maza, J. and Angel, J. R. P. 1983, ApJ, 266, 470

Mas-Hesse, J. M., Rodriguez-Pascual, P. M., Sanz Fernandez de Cordoba, L., Mirabel, I.
    F., Wamsteker, W., Makino, F. & Otani, C. 1995, A&A, 298, 22

Matthews, K., Neugebauer, G., McGill, J., & Soifer, B. T. 1987, AJ, 94, 297

Meurer, G. R., Heckman, T. M., Lehnert, M. D., Leitherer, C., & Lowenthal, J. 1997, AJ,
    114, 54

Miles, J. W., Houck, J. R., Hayward, T. L., & Ashby, M. L. N. 1996, ApJ, 465, 191

Miller, J. S. & Goodrich, R. W. 1990, ApJ, 355, 456

Miller, J. S., Goodrich, R. W. & Mathews, W. G. 1991, ApJ, 378, 47

Mouri, H., Taniguchi, Y., Kawara, K. & Nishida, M. 1989, ApJ, 346, L73

Mundell, C. G., Pedlar, A., Baum, S. A., O'Dea, C. P., Gallimore, J. F., & Brinks, E. 1995, MNRAS, 272, 355

Murayama, T., Mouri, H. & Taniguchi, Y. 2000, ApJ, 528, 179

Neff, S. G. & Ulvestad, J.S. 1988, AJ, 96, 841

Netzer, H. & Peterson, B. M. 1997, ASSL Vol. 218: Astronomical Time Series, 85

Neugebauer, G. & 27 colleagues 1984, ApJL, 278, L1

Neugebauer, G., Graham, J. R., Soifer, B. T., & Matthews, K. 1990, AJ, 99, 1456 (N90)

Noguchi, M. 1988, Astr. Ap., 203, 259

Norman, C. A. 1987, Star Formation in Galaxies, 395

Norman, C. & Scoville, N. 1988, ApJ, 332, 124

O'Connell, R. W., Gallagher, J. S., & Hunter, D. A. 1994, ApJ, 433, 65

Ogle, P. M., Cohen, M. H., Miller, J. S., Tran, H. D., Fosbury, R. A. E. & Goodrich, R. W. 1997, ApJ, 482, L37

Ohsuga, K., & Umemura, M. 1999, ApJ, 521, L13

Osterbrock, D. E., 1989, Astrophysics of Gaseous Nebulae and Active Galaxies, University Science Books, USA

Osterbrock, D. E. 1991, PASP, 103, 874

Osterbrock, D. E. 1993, Revista Mexicana de Astronomia y Astrofisica, vol. 26, 26, 65

Osterbrock, D. E. & Fulbright, J. P. 1996, PASP, 108, 183

Osterbrock, D. E. & Koski, A. T. 1976, MNRAS, 176, 61P

Papadakis, I. E. & McHardy, I. M. 1995, MNRAS, 273, 923

Pedlar, A., Fernandez, B., Hamilton, N. G., Redman, M. P., & Dewdney, P. E. 1998, MNRAS, 300, 1071

Pedlar, A., Kukula, M. J., Longley, D. P. T., Muxlow, T. W. B., Axon, D. J., Baum, S., O'Dea, C., & Unger, S. W. 1993, MNRAS, 263, 471

Penston, M. V. & Perez, E. 1984, MNRAS, 211, 33P

Penston, M. V. et al. 1990, A&A, 236, 53

Perez-Fournon, I. & Wilson, A. S. 1990, ApJ, 356, 456

Peterson, B. M., 1997, An Introduction to Active Galactic Nuclei, Cambrifge University Press, U.K.

Pier, E. A. & Krolik, J. H. 1992, ApJ, 401, 99

Pogge, R.W. 1989, ApJ, 345, 730

Radomski, J. T., Piña, R. K., Packham, C., Telesco, C. M., & Tadhunter, C. N. 2001, ASP Conf. Ser. 249: The Central Kiloparsec of Starbursts and AGN: The La Palma Connection, 325

Radomski, J. T., Piña, R. K., Packham, C., Telesco, C. M., & Tadhunter, C. N. 2002, ApJ, 566, 675.

Radomski, J. T., Piña, R. K., Packham, C., Telesco, C. M., De Buizer, J. M., Fisher, R. S., & Robinson, A. 2003, ApJ, 587, 117

Rees, M. J. 1966, Nature, 211, 468

Rees, M. J., 1984, ARA&A, 22, 471

Rieke, G. H. 1992, ASP Conf. Ser. 31: Relationships Between Active Galactic Nuclei and Starburst Galaxies, 61

Rieke, G. H. & Lebofsky, M. J. 1981, ApJ, 250, 87

Rieke, G. H., Lebofsky, M. J. & Walker, C. E. 1988, ApJ, 325, 679

Rieke, G. H. & Low, F. J. 1972, ApJ, 176, L95

Rieke, G. H. & Low, F. J. 1972, ApJ, 177, L115

Robinson, A. et al. 1994, A&A, 291, 351

Robson, I. 1996, Active Galactic Nuclei, Praxis Publishing Ltd, Chichester

Roche, P. F. & Aitken, D. K. 1985, MNRAS, 215, 425

Roche, P. F., Aitken, D. K., Smith, C. H., & Ward, M. J. 1991, MNRAS, 248, 606

Roche, P. F., Aitken, D. K., & Whitmore, B. 1983, MNRAS, 205, 21P

Rodriguez Espinosa, J.M., Perez Garcia, A. M., Lemke, D., & Meisenheimer, K. 1996, A&A, 315, L129 (RE96)

Ruiz, M., Young, S., Packham, C., Alexander, D. M., & Hough, J. H. 2003, MNRAS, (in press)

Sandage, A., & Tammann, G. A., 1987, A Revised Shapley-Ames Catalog of Bright Galaxies (Carnegie Inst. of Washington Publ. 635, Washington D.C.) (ST87)

Sanders, D. B., Soifer, B. T., Elias, J. H., Madore, B. F., Matthews, K., Neugebauer, G. & Scoville, N. Z. 1988, ApJ, 325, 74

Schmitt, H. R. & Kinney, A. L. 1996, ApJ, 463, 498

Schulz, H. & Komossa, S. 1993, A&A, 278, 29

Sellgren, K., Werner, M.W., & Dinerstein, H.L. 1983, ApJ, 271, L13

Seyfert, C. 1943, ApJ, 97, 28

Shuder, J. M. 1981, ApJ, 244, 12

Smith, C. H., Aitken, D. K. & Roche, P. F. 1989, MNRAS, 241, 425

Smith, H. E., Lonsdale, C. J., & Lonsdale, C. J. 1998, ApJ, 492, 137

Soifer, B. T. et al. 2000, AJ, 119, 509

Stasinska, G. 1984, A&A, 135, 341

Stockton, A., Ridgway, S. E. & Lilly, S. J. 1994, AJ, 108, 414

Storchi-Bergmann, T., Gonzalez Delgado, R. M., Schmitt, H. R., Cid Fernandes, R., & Heckman, T. 2001, ApJ, 559, 147

Sturm, E., Alexander, T., Lutz, D., Sternberg, A., Netzer, H., & Genzel, R. 1999, ApJ, 512, 197.

Surace, J. A. & Sanders, D. B. 1999, ApJ, 512, 162

Sutherland, R. S., Bicknell, G.V., & Dopita, M. A. 1993, ApJ, 414, 510

Tadhunter, C. N. et al. 2000, MNRAS, 313, L52

Tadhunter, C. N., Packham, C., Axon, D. J., Jackson, N. J., Hough, J. H., Robinson, A.,
    Young, S. & Sparks, W. 1999, ApJ, 512, L91

Telesco, C. M. 1988, ARA&A, 26, 343

Telesco, C. M. 1993, Infrared Astronomy : IV Canary Islands Winter School of
    Astrophysics, 175

Telesco, C. M., Becklin, E. E., & Wynn-Williams, C. G. 1980, ApJ, 241, L69

Terlevich, E., Diaz, A. I. & Terlevich, R. 1990, Revista Mexicana de Astronomia y
    Astrofisica, vol. 21, 21, 218

Terlevich, E., Diaz, A. I., & Terlevich, R. 1990, MNRAS, 242, 271

Terlevich, R. & Melnick, J. 1985, MNRAS, 213, 841

Thornton, R. J., Stockton, A. & Ridgway, S. E. 1999, AJ, 118, 1461

Toomre, A., & Toomre, J. 1972, ApJ, 178, 623

Tran, H. D., Miller, J. S. & Kay, L. E. 1992, ApJ, 397, 452

Tresch-Fienberg, R., Fazio, G. G., Gezari, D. Y., Lamb, G. M., Shu, P. K., Hoffmann, W.
    F., & McCreight, C. R. 1987, ApJ, 312, 542

Turner, J.,E. H., Allington-Smith, J., Chapman, S., Content, R., Done, C., Haynes, R.,
    Lee, D., & Morris, S. 2002, MNRAS, 331, 284

Ueno, S., Koyama, K., Nishida, M., Yamauchi, S. & Ward, M. J. 1994, ApJ, 431, L1

Ulvestad, J. S. & Wilson, A. S. 1989, ApJ, 343, 659

Ulvestad, J. S., Wrobel, J. M., & Carilli, C. L. 1999, ApJ, 516, 127

van der Bliek, N. S., Manfroid, J., & Bouchet, P. 1996, A&AS, 119, 547

Velusamy, T. & Langer, W. D. 1998, Nature, 392, 685

Ward, M. J., Blanco, P. R., Wilson, A. S. & Nishida, M. 1991, ApJ, 382, 115

Ward, M., Elvis, M., Fabbiano, G., Carleton, N. P., Willner, S. P., & Lawrence, A. 1987, ApJ, 315, 74.

Weedman, D. W. 1983, ApJ, 266, 479

Weingartner, J. C. & Draine, B. T. 2001, ApJ, 548, 296

Whysong, D. & Antonucci, R. 2001, ApJL, (submitted) (astro-ph/0106381)

Wilkes, B. J. & Elvis, M. 1987, ApJ, 323, 243

Woltjer L., 1990, Active Galactic Nuclei, eds T. L. Courvoisier & M. Mayor, Springer-Verlag, Berlin

Yee, H. K. C. 1980, ApJ, 241, 894

Yoshida, M. & Ohtani, H. 1993, PASJ, 45, 407

Young, S., Corbett, E. A., Giannuzzo, M. E., Hough, J. H., Robinson, A., Bailey, J. A. & Axon, D. J. 1999, MNRAS, 303, 227

Young S., Packham C., Hough J. H., Efstathiou A., MNRAS, 283, 1

Zwicky, F., Herzog, E., & Wild, P. 1968, Pasadena: California Institute of Technology (CIT), 1961-1968

BIOGRAPHICAL SKETCH

I was born in Jersey City, N.J. but was primarily raised in Jacksonville, FL since the age of 6. As long as I can remember I have been interested in exploring the Universe. When I was a wee lad the three things I wanted to be most was a football player, an astronomer, or a dinosaur. Football hurt too much to be considered as a full time profession. As for dinosaur, I do somewhat regret not fully exploring my options there. However I am very glad to be an astronomer exploring the Universe. I drew a great deal of inspiration watching television that dealt with the Universe such as NOVA and Carl Sagan's Cosmos. One of the first magazines I can remember reading was National Geographic and it's issues dealing with the Viking exploration of Mars and the Voyager exploration of the outer planets. I can still remember the excitement of my first astronomy class in college. It was the first time I ever used a telescope. I was lucky enough to see a massive storm on Saturn before it had even been officially discovered. Thirteen years later I've finally completed a part of the journey I began as a child. The journey however continues as there is still a Universe to explore and questions to answer.
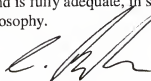
I certify that I have read this study and that in my opinion it conforms to acceptable standards of scholarly presentation and is fully adequate, in scope and quality, as a dissertation for the degree of Doctor of Philosophy.

Fred W. Hamann, Chair
Associate Professor of Astronomy

I certify that I have read this study and that in my opinion it conforms to acceptable standards of scholarly presentation and is fully adequate, in scope and quality, as a dissertation for the degree of Doctor of Philosophy.
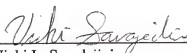
Christopher C. Packham
Assistant Scientist of Astronomy

I certify that I have read this study and that in my opinion it conforms to acceptable standards of scholarly presentation and is fully adequate, in scope and quality, as a dissertation for the degree of Doctor of Philosophy.
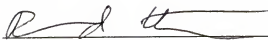
Charles M. Telesco
Professor of Astronomy

I certify that I have read this study and that in my opinion it conforms to acceptable standards of scholarly presentation and is fully adequate, in scope and quality, as a dissertation for the degree of Doctor of Philosophy.

Vicki L. Saradejini
Assistant Professor of Astronomy

I certify that I have read this study and that in my opinion it conforms to acceptable standards of scholarly presentation and is fully adequate, in scope and quality, as a dissertation for the degree of Doctor of Philosophy.

Richard J. Elston
Professor of Astronomy

I certify that I have read this study and that in my opinion it conforms to acceptable standards of scholarly presentation and is fully adequate, in scope and quality, as a dissertation for the degree of Doctor of Philosophy.

Steven Detweiler
Professor of Physics

This dissertation was submitted to the Graduate Faculty of the Department of Astronomy in the College of Liberal Arts and Sciences and to the Graduate School and was accepted as partial fulfillment of the requirements for the degree of Doctor of Philosophy.

May 2003

Dean, Graduate School